Thord Niri Gjesdahl Heggren

Improving Impurity Photovoltaic Solar Cells via Inhomogeneous Doping Concentrations in Proximity to the Depletion Region

Master's thesis in Nanotechnology
Supervisor: Turid Reenaas
June 2023

NTNU
Norwegian University of
Science and Technology

Thord Niri Gjesdahl Heggren

Improving Impurity Photovoltaic Solar Cells via Inhomogeneous Doping Concentrations in Proximity to the Depletion Region

Master's thesis in Nanotechnology
Supervisor: Turid Reenaas
June 2023

Norwegian University of Science and Technology
Faculty of Natural Sciences
Department of Physics

NTNU
Norwegian University of
Science and Technology

Abstract

Conventional single junction solar cell have an efficiency limit of 33.7%. One possible method to go beyond this limit is to introduce an intermediate band in the bandgap to make so-called intermediate band solar cells (IBSC). The theoretical efficiency limit of such cells is 49.4%. A proposed method to make IBSC is by high concentration deep-level doping, where the introduced states delocalize and form the intermediate band. However, the delocalization can be difficult to achieve in practice, and the cells could rather end up as impurity photovoltaic (IPV) cells. IPV cells have the same theoretical efficiency limit as IBSC, and the main difference between them is that IPV cells have localized states in the bandgap that allows for non-radiative Shockley–Read–Hall (SRH) recombination, that might reduce the efficiency significantly.

An IPV cell only benefits from the states in the bandgap if the net generation (generation minus recombination) via the impurities is positive. As early-stage IPV devices are normally prone to high SRH recombination rates, reducing this mechanism is necessary to approach their theoretical efficiency limit. The aim of this thesis is to combine a doping design principle found in literature for heterojunctions that utilize inhomogeneous doping concentrations in proximity to the depletion region, to suppress SRH recombination with IPV cells. Oxides have been suggested as suitable materials to make IPV solar cells, and since oxides mostly form heterojunctions due to the difficulty to fabricate both a p- and n-doped oxide of the same material, they can be especially suitable this combination. However, as reliable material parameters for these materials are not easily available, the work in this thesis have been focused on the more common III-V semiconductors GaAs and AlGaAs.

The work in this thesis is purely theoretical, and have been conducted using the solar cell simulation program SCAPS. A initial set of simulations were first conducted to verify SCAPS's capability to simulate the design principle. These simulations were successful and SCAPS was deemed suitable for the subsequent simulations. However, later results showed some inconsistencies in the simulations when layers were split into two. The cause is found to be SCAPS's mesh generation settings' dependency of the layers in the cell, which determines the points of calculations. The result of this in this thesis is that the absolute efficiency increase due to the design principle is slightly lower than what the numerical values indicates.

Next, the doping design principle was investigated for conventional GaAs and AlGaAs cells, without the IPV effect. The results showed that the conduction band offset in p-GaAs/n-AlGaAs cells reduced the electron flow when the design principle was applied. Thus, it is concluded that the heterojunction must be free of band offsets in order to benefit from the design principle. After mathematically removing the band offset by adjusting the electron affinities, a positive result was obtained for the design principle. Then, the relative layer thicknesses in the cells were varied, which for the optimal thicknesses increased the cell efficiency by over 20% compared to the initial thicknesses. However, the numeric values of the layer thicknesses is only applicable to the cells simulated here, and a similar optimization must be conducted if the design principle is to be applied to other cells, with other material parameters.

Finally, the doping design principle was attempted combined for three IPV GaAs and AlGaAs cells. The result showed efficiency increased about 5% for all three cells. This is a substantial improvement which suggests that the combination of inhomogeneous doping and IPV cells is beneficial. However, the physical explanation behind the improvement in the IPV cells due to the design principle is not the same as for the conventional cells, where the SRH recombination is reduced. This is confirmed by the fact that the best performing cells does not have the highest net generation rate via the impurities. It is suggested here that the increase in efficiency is partly due to a more effective transport of the generated carriers, but the results also indicate that other unknown factors that is not studied in this thesis also contribute. Thus, more research is needed to fully understand the effect of inhomogeneous doping in IPV cells.

Sammendrag

Konvensjonelle enkelovergangs solceller har en effektivitetsgrense på 33.7%. En mulig måte å overgå denne grensen er å introdusere et mellombånd i båndgapet for å lage såkalte mellombånd solceller (IBSC). Den teoretiske effektivitetsgrensen for slike celler er 49.4%. En foreslått måte for å lage IBSC er ved høy konsentrasjon, dyp-level doping, hvor de introduserte tilstandene delokaliserer og former mellombåndet. Men, i praksis kan delokaliseringen være vanskelig å få til, og cellene kan i stedet heller ende opp som defekt fotovoltaisk (IPV) solceller. IPV celler har den samme teoretiske effektivitetsgrensen som IBSC, og hovedforskjellen mellom dem er at IPV celler har lokaliserte tilstander i båndgapet som tillater ikke-radiativ Shockley–Read–Hall (SRH) rekombinering, som kan redusere effektiviteten betydelig.

En IPV-celle nyter bare godt av tilstandene i båndgapet hvis netto generering (generering minus rekombinering) via defektene er positiv. Ettersom tidlig fase IPV enheter normalt er utsatt for høye SRH rekombinerings rater, er det nødvendig å redusere denne mekanismen for å nærme seg deres teoretiske effektivitetsgrense. Målet med denne avhandlingen er å kombinere et doping-designprinsipp fra litteraturen for heterooverganger som utnytter inhomogen dopingkonsentrasjon i nærheten av deplesjonsområdet for å hindre SRH rekombinering med IPV celler. Oksider har blitt foreslått som egnede materialer for å lage IPV celler, og ettersom oksider i hovedsak danner heterooverganger på grunn av vansligheten ved å fremstille både en p- og n-dopet oksid av det samme materiale, kan de være spesielt egnede for denne kombinasjonen. Men, ettersom pålitelige materialparametere for disse materialene ikke er lett tilgjengelige, har arbeidet i denne avhandlingen vært gjort på de vanligere III-V halvlederne GaAs og AlGaAs.

Arbeidet i denne avhandlingen har vært utelukkende teoretisk, og har blitt utført med solcellesimuleringsprogrammet SCAPS. En innledende serie med simuleringer ble først utført for å bekrefte SCAPSs evne til å simulere designprinsippet. Disse simuleringene var vellykkede, og SCAPS ble ansett som egnet for de påfølgende simuleringene. Men, senere resultater viste noe inkonsistens i sumuleringene når lag ble delt i to. Årsaken ble funnet til å være SCAPS sine "beregningspunktinnstillinger" sin avhengighet av lagene i cellen, som bestemmer kalkulasjonspunktene. Resultatet av dette i denne avhandlingen er at den absolutte effektivitetsøkningen forårsaket av designprinsippet er noe lavere enn hva de numeriske verdiene tilsier.

Deretter ble doping-designprinsippet undersøkt for konvensjonelle GaAs og AlGaAs celler uten IPV effekten. Resultatene viste at ledningsbåndavviket i p-GaAs/n-AlGaAs celler elektronstrømmen når designprinsippet ble anvendt. Dermed er det konkludert at heterooverganger må være uten båndavvik for å dra nytte av designprinsippet. Etter å ha matematisk fjernet båndavviket ved å justere elektronaffinitetene, ble et positivt resultat oppnådd ved designprinsippet. Deretter ble de relative lagtykkelsene i cellene variert, noe som ved de optimale tykkelsene økte effektiviteten i cellen med over 20% sammenlignet med de originale tykkelsene. Men, de numeriske verdiene av lagtykkelsene gjelder bare for cellene som ble simulert her, og en lik optimalisering må bli gjennomført hvis designprinsippet skal brukes på andre celler med andre materialparametere.

Til slutt ble det samme doping-designprinsippet forsøkt kombinert med tre IPV GaAs og AlGaAs celler. Resultatet viste en økning i effektivitet på omtrent 5% på alle tre cellene. Dette er en betydelig forbedring som antyder at kombinasjonen av inhomogen doping og IPV celler gunstig. Men, den fysiske forklaringen på forbedringen i IPV cellene grunnet designprinsippet er ikke det samme som i de konvensjonelle cellene, hvor SRH rekombineringen blir redusert. Dette bekreftes av det faktum at de høyest ytende cellene ikke har den høyest netto genereringsraten via urenhetene. Det blir forestått her at effektivitetsøkningen delvis er på grunn av mer effektiv transport av de genererte ladningsbærerne, men resultatene indikerer også andre ukjente faktorer som ikke er undersøkt i denne avhandlingen også bidrar. Derfor er mer forsking nødvendig for å fullt forstå effekten av inhomogen doping i IPV celler.

Preface

This master's thesis concludes my five-year M.Sc. degree in Nanotechnology at the Norwegian University of Science and Technology (NTNU) in Trondheim, Norway. The work was carried out at the Department of Physics under the supervision of Turid Reenaas.

I would like to extend my deepest appreciation to my supervisor, Turid Reenaas. Your invaluable support, encouragement, and consistent feedback have been indispensable in bringing this thesis to fruition. Working on this project with you has been an incredible learning experience, and I am forever grateful for this.

I would also like to sincerely express my gratitude to my classmates for five incredible years together. Thank you for your support, assistance, and all the cherished memories we have created. I wish you all the best in the future.

Finally, to my friends and family. I could not have done this without you. Thank you for being who you are, and thank you for your endless love and support.

Thord Niri Gjesdahl Heggren
Trondheim, 19th of June 2023

Contents

Chapter 1

Introduction

Climate change is one of the biggest challenges of our times. In 2021, the world's total primary energy consumption was approximately 595.15 exajoules [1]. Of this, over 82 % came from fossil fuels. In addition to not being a sustainable energy source, fossil fuel burning pollutes the air and emits greenhouse gasses. This is the primary cause of the current climate change, altering the Earth's ecosystem and potentially harming all life all around the world.

The 2030 Agenda for Sustainable Development presented by the United Nations (UN) in 2015 set 17 goals to improve life on Earth [2]. The seventh goal states *"Ensure access to affordable, reliable, sustainable and modern energy for all"*. This shows that there is a world-wide agreement that the development and implementation of sustainable and renewable energy sources is an unavoidable part of the solution to climate change.

One possible energy source that could fulfill the criteria set by the UN is solar energy. Every second, the sun emits 1.7×10^{17} J of energy to the Earth [3]. This means, in theory, that in under one hour the sun could power the whole Earth for one year. While it of course is unrealistic to utilize all the solar energy, it shows the enormous potential of the sun as an energy source.

The current state of solar energy is promising. Ever since 2011, there have been an nearly exponential growth in the global solar energy production. As of 2021, the total photovoltaic (PV) capacity was 942 GW, and the yearly increase rate was at an all time high. This was achieved despite the estimated 57 % jump in PV module cost due to silicon shortage, again showing the potential of solar power [4].

However, a potential problem with the current solar cells is their relatively low efficiency. The theoretical limit for a conventional single junction solar cell is about 33.7% [5], not much higher than the current record for silicon solar cells of 26.7% [6]. Thus, when there is a limitation on available area, new technologies have to be explored in order for solar cells to be a substantial producer of energy.

In general, third generation solar cells aim to achieve a high efficiency while keeping price low. There are several proposed methods to achieve this, and one of them is by introducing an intermediate band (IB) in the bandgap E_g in so-called intermediate band solar cells (IBSC) [7]. The purpose of this IB is to increase the fraction of solar radiation that can be harnessed while maintaining a high voltage in the cell. In theory, such cell could reach efficiencies up to 49.4 % [8]. As of 2022, the highest recorded efficiency of an IBSC is around 19% [9]. However, the technology is still in its early stages, and IBSCs are yet to be commercially available. Figure 1.1 illustrates the theoretical efficiency limits of single junction solar cells and IBSCs, in addition to the current records and the efficiency of commercially available cells.

One possible method for making IBSC is using the *impurity-based approach*. It is known that doping of semiconductors introduces discrete states in the bandgap, even deep-level (DL) states located far away from the valence band (VB) and conduction band (CB). The idea is then by sufficient high density doping of the semiconductor material, the electronic wave functions of the dopants overlap so that the states transition from being localized to becoming delocalized, creating an energy band, i.e. the IB. However, the delocalization can be difficult to achieve in practice, and the cells could rather end up as impurity photovoltaic (IPV) cells [10]. The main difference between IPV cells and IBSC is that IPV cells does not have bands in the bandgap, but localized states that favors thermal, non-radiative recombination. The maximum theoretical efficiency is the same for IPV cells and IBSCs, and since no IPV cells have been successfully fabricated, there is no record efficiency yet.
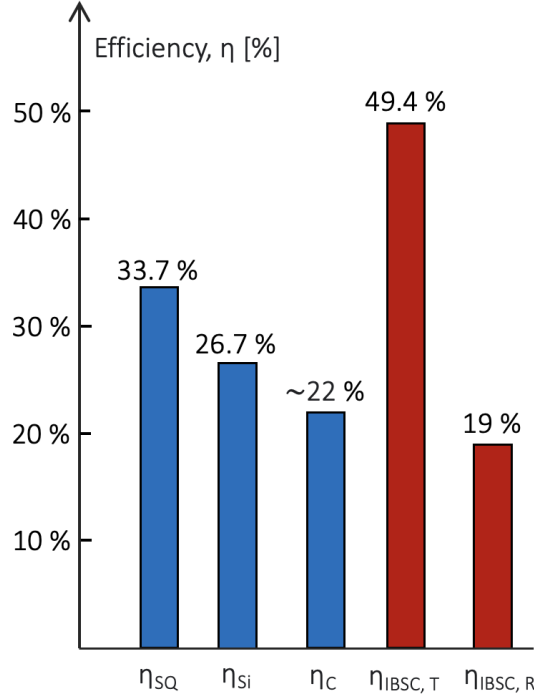
Figure 1.1: Comparison of solar cell efficiencies. The blue columns represents single junction solar cells, while the red columns represent intermediate band solar cells. η_{SQ}, η_{Si}, and η_{C} are the Shockley-Queisser efficiency limit, the record efficiency achieved with silicon, and an approximate value of the efficiency of commercially available cells, respectively. $\eta_{\text{IBSC, T}}$ and $\eta_{\text{IBSC, R}}$ are the theoretical efficiency limit of IBSC and the record efficiency of IBSC, respectively.

The resulting efficiency of an IPV solar cell is strongly dependent on the amount of non-radiative Shockley–Read–Hall (SRH) recombination in the cell. This is because while the DL states allows for a two-step generation path, they also act as recombination centers. Thus, only if the rate of generation is greater than the rate of recombination via the DL states, does the IPV cell benefit from the introduction of said states. It is therefore desirable to design IPV solar cells where the non-radiative SRH recombination mechanism is suppressed.

This work in this thesis focuses on a design principle presented by Santhanam and Fan [11] that utilizes inhomogeneous doping concentration around the depletion region to suppress SRH recombination in heterojunctions. The aim was to attempt to combine this design principle with IPV cells with the goal of creating higher efficiency cells by improving the generation-to-recombination rate via the DL states. Oxide-based IB materials could suitable for this purpose, as it is difficult to fabricate both a p- and n-doped oxide of the same material, and they are

thus often heterostructures. However, as reliable material parameters for these materials are not easily available, the work in this thesis have been focused on the more common III-V semiconductors GaAs and AlGaAs.

The work in this thesis is purely theoretical, i.e. it has all been conducted using the solar cell simulation program SCAPS (a Solar Cell Capacitance Simulator) [12]. SCAPS was developed at Department of Electronics and Information Systems (ELIS) of the University of Gent, Belgium by M. Burgelman et al. It is freely available to the PV research community and can be obtained on request by contacting Marc Burgelman. A initial set of simulations were first conducted to verify SCAPS capability to simulate the design principle. Next, the design principle was investigated on conventional GaAs and AlGaAs cells, without the IPV effect. Finally, the same design principle was attempted combined with IPV GaAs and AlGaAs cells.

This thesis is divided into five chapters. In chapter 2 is the relevant background theory required to understand the work conducted in this thesis presented. Then, in chapter 3 all parameters used in SCAPS necessary to replicate the simulations are given. In chapter 4, the results and the subsequent discussion of the simulations are presented. Finally, in chapter 5, a final conclusion and suggestions for further work is given.

Chapter 2

Theory

Parts of this chapter is reworked from the preceding *specialization project* [13]. It provides the necessary theory to understand the work conducted in this thesis, and is divided into five main parts. First, section 2.1 presents some fundamental solar cell physics relevant for the upcoming simulations. Next, while not directly relevant for this thesis and only included for completeness, section 2.2 introduces the concept of intermediate band solar cells. Then, section 2.3 introduces the impurity photovoltaic effect. In section 2.4, an introduction of the doping design principle used in this thesis of inhomogeneous doping concentration in proximity to the depletion region to suppress non-radiative recombination is given. This section is based on the paper by Santhanam and Fan in Ref. [11]. Finally, section 2.5 introduces the simulation program SCAPS used to conduct the simulations in this thesis.

2.1 Solar Cell Physics

When nothing else is stated, the theory presented here is based on Würfel and Würfel's book *Physics of Solar Cells: From Basic Principals to Advanced Concepts* [3], J. Nelson's book *The Physics of Solar Cells* [14], and S. M. Sze's book *Semiconductor Devices: Physics and Technology* [15]. It is assumed that the reader has a basic understanding of semiconductor physics and the fundamental properties of light and the solar spectra.

2.1.1 Energy Bands

In general, solar cells are made of semiconductors. The electronic states in these materials are characterized by having a nearly completely full valence band (VB) and a nearly empty conduction band (CB), separated by an energy gap; the bandgap E_g. The probability that an electron occupies a certain electronic state with energy E is given by the Fermi–Dirac distribution function $F(E)$

$$F(E) = \frac{1}{1 + \exp\left\{(E - E_\mathrm{F})/k_\mathrm{b}T\right\}} \tag{2.1}$$

where k_b is Boltzmann's constant, T the temperature in Kelvin, and the Fermi level E_F is the energy at which the probability of occupation by an electron is 50%. For intrinsic semiconductors, E_F is in the middle of the bandgap. For extrinsic semiconductors, i.e. doped semiconductors, the position of E_F is shifted due to the uneven distribution of electrons and holes between the bands. P-type semiconductors are doped with acceptors, and the Fermi level in these materials is shifted down towards the VB edge E_V. N-type semiconductors are doped with donors, and

the Fermi level in these materials is shifted up towards the CB edge E_C. Figure 2.1 shows the band diagram and the position of the Fermi level for (1) intrinsic semiconductors, (2) p-type semiconductors, and (3) n-type semiconductors.
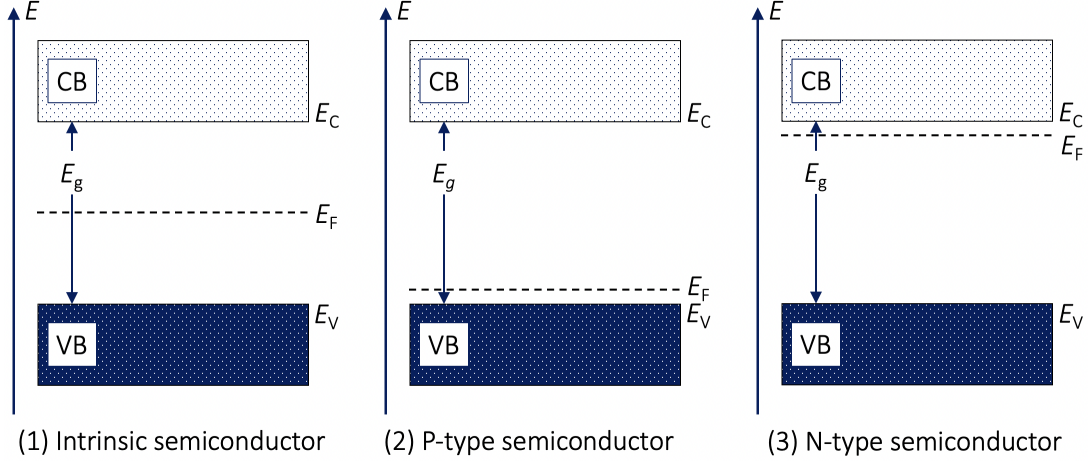
Figure 2.1: Band diagram with the position of the Fermi level E_F for (1) intrinsic semiconductors, (2) p-type semiconductors, and (3) n-type semiconductors. E_g is the band gap, and E_V and E_C are the valence band (VB) edge and conduction band (CB) edge, respectively.

To calculate the number of electrons per unit volume in the CB in a semiconductor, i.e. the electron density n, one can start from the electron density in an incremental energy range $\mathrm{d}E$. This density $n(E)$ is given by the product of the density of states $N(E)$ and the Fermi–Dirac distribution function (Eq.(2.1)). The density of states is the density of allowed energy states (including electron spin) per energy range per unit volume, and is given by

$$N(E) = 4\pi \left(\frac{2m_\mathrm{n}}{h^2} \right)^{3/2} E^{1/2} \tag{2.2}$$

where m_n is the effective mass of the electrons and h is Planck's constant. Thus, the electron density in the CB is given by integrating $N(E)F(E)\,\mathrm{d}E$ from the bottom of the CB (E_C initially taken to be $E = 0$ for simplicity) to the top of the CB E_Top:

$$n = \int_0^{E_\mathrm{Top}} N(E)\,F(E)\,\mathrm{d}E \tag{2.3}$$

However, as will be useful in this thesis, the integral limits can be changed to any values within the CB. Therefore, one can use Eq.(2.3) not to calculate the *total* electron density in the CB, but the electron density in a specific region in the CB. To exemplify, if one wishes to know the electron density in the upper half of the CB, this can be calculated by using Eq.(2.3) with $\frac{1}{2}E_\mathrm{Top}$ as the lower integral limit and E_Top as the upper integral limit.

2.1.2 Generation

In semiconductor physic, generation is the process where an electron-hole pair is generated. This happens when an electron is supplied with a certain amount of energy and gets excited from a state in the VB to a state in the CB. Several processes can provide this energy, such as impact ionization, lattice vibrations, and, most important for solar cells, photon absorption. The excitations can only promote electrons to energy states, so when there are no states in the bandgap, the electrons must minimum receive the energy of the bandgap width. If the energy is supplied from a photon with more energy than the bandgap width, the excess energy is lost in thermalization processes. If the provided energy is less than the bandgap width, no generation occurs. Figure 2.2 illustrates the processes when the energy provided from a photon E_γ is (1) less than E_g, (2) equal to E_g, and (3) larger than E_g.
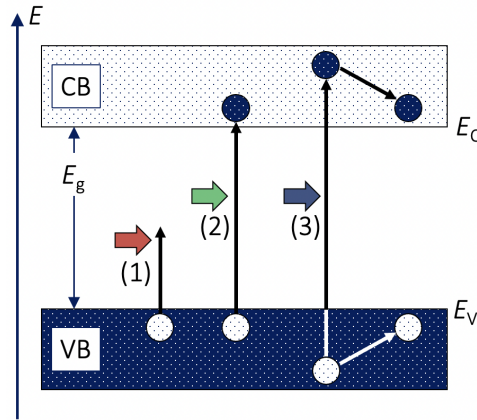
Figure 2.2: Three possible outcomes when energy is provided to a semiconductor. (1) The energy is less than the bandgap width and no generation occurs. (2) The energy is equal to the bandgap and an electron-hole pair is generated. (3) The energy is larger than the bandgap, and excess energy is lost in thermalization processes. Figure based on Ref. [16].

The fraction of photons that gets absorbed at a certain depth is defined by the absorption coefficient $\alpha(E_\gamma)$. It is a material property dependent on the energy of the incoming photon and independent of the geometry of the body. If absorption occurs, an electron-hole pair is generated. α is proportional to the density of occupied states in the VB in which holes can be generated, and unoccupied states in the CB in which electrons can be generated.

A transition from the VB to the CB, i.e. the generation process, can either be direct or indirect. In direct transitions, the momentum of the electron–hole system does not change, and the balance of momentum is then consistent with a reaction exclusively with photons. Such transitions can only occur in semiconductors where the momentum of the VB maximum and CB minimum aligns. In indirect transitions, the generation cannot occur by photons alone, as their momentum is too low. Instead, the momentum balance is satisfied through the participation of phonons. As only one particle participates in direct transitions, the absorption coefficient for direct material is larger, thus reducing the required thickness needed to absorb the absorbable part of the solar spectrum with photon energies $E_\gamma > E_g$. In fact, the absorption coefficient of direct semiconductors tend to be more alike to each other than to indirect semiconductors. In this thesis, this will be useful when the fraction of aluminium x in aluminium gallium arsenide $Al_xGa_{1-x}As$ will be chosen, as this material changes from being direct to indirect at around $x = 0.45$ [17].

2.1.3 Recombination

Recombination is the process where an electron-hole pair is annihilated, i.e. the opposite process of generation. In a recombination process, either photons, phonons, or both, are emitted. If only photons are released, the process is called radiative recombination, and it is the reverse of photon induced generation. Otherwise, the process is called non-radiative recombination. The principle of detailed balance tell us that in equilibrium with the radiation in the environment, the rates of generation and recombination are exactly balanced, i.e. for a solar cell in the dark.

In Figure 2.3, (1) illustrates the radiative recombination mechanism present in semiconductors. As can be seen in the figure, the excess energy from this process is released as a photon. This mechanism is important for solar cells, as it is non-avoidable and the only recombination mechanism included when calculating the maximum theoretical efficiency.
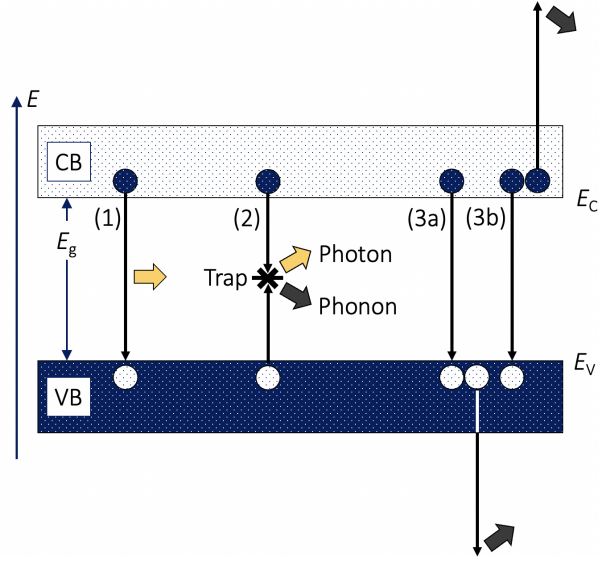
Figure 2.3: Recombination mechanisms in semiconductors. (1) is radiative recombination, (2) is radiative and non-radiative SRH recombination for the yellow and black arrow, respectively, and (3a) is Auger recombination when the excess energy is captured by a hole, (3b) is Auger recombination when the excess energy is captured by an electron. Figure based on Ref. [16].

In Figure 2.3, (2) illustrates the Shockley–Read–Hall (SRH) recombination mechanism, also called impurity recombination, present in semiconductors. As can be seen in the figure, by recombining via a state in the bandgap, the excess energy from the process can either be released as a photon or a phonon. The former is is often neglected when discussion this recombination mechanism because the emission of photons from SRH recombination very low in conventional silicon solar cells. However, as will be important later, this process is relevant for IPV cells. This is because the introduced DL states in IPV cells does not only allows for optical generation, but also optical recombination. This is more elaborated on in section 2.3.

The non-radiative SRH recombination rate for electrons $R_{e,\,SRH}$ is given by

$$R_{e,\,SRH} = \sigma_e \nu_e n_e N_t (1 - f_t) \tag{2.4}$$

where σ_e is the capture cross section (CCS) of electrons, ν_e is the thermal velocity of electrons, n_e is the density of electrons, N_t is the impurity density, and f_t is probability of the impurity level being occupied by an electron. The CCS of a defect in a semiconductor describes the

effectiveness of the defect to capture a carrier and is a measure (typically in cm^2) of how close the carrier needs to come to the defect to be captured. The most predominant recombination process in solar cells is non-radiative recombination.

While not being relevant for this thesis and only included for completeness, (3) in Figure 2.3 illustrates the non-radiative Auger recombination mechanism present in semiconductors. More specifically, (3a) shows non-radiative Auger recombination when the excess energy is captured by a hole, and (3b) shows non-radiative Auger recombination when the excess energy is captured by an electron. For both processes, the excess energy captured by the particles are released as phonons. Auger recombination increases with increasing carrier concentrations and contributes to reducing the efficiency in solar cells.

2.1.4 p-n Junctions

Combining a p-type semiconductor and n-type semiconductor creates a p-n junction. Such junctions can be illustrated using energy band diagrams, i.e. the position of the band edges and Fermi level with respect to the position in the p-n junction. The following paragraphs describes the energy band diagram for a p-n junction at four different conditions; with and without illumination, and with and without an applied voltage.

At equilibrium, i.e. in the dark and without a bias, the Fermi level in the junction is invariant with position. Because of this, the p-side of the junction is shifted up relative to the n-side in energy space. The energy distance of this shift is given by qV_{bi}, q being the elemental charge and V_{bi} the built in potential difference across the space charge region at equilibrium caused by the doping. The band diagram for such a p-n junction is shown in Figure 2.4a. The region where the energy bands are non-constant with respect to position is called depletion region W. This region is created due to the electron flow from the n-type semiconductor to the p-type semiconductor when the junction is formed. It is called the depletion region as the built in electric fields depletes it of free carriers.

During illumination, the p-n junction is no longer in equilibrium. The illumination causes the carrier concentrations in the bands to increase. This would both shift the Fermi level down to the VB and up to the CB, and one can no longer use Fermi-Dirac statistics to describe the carrier populations in each band. In order to fix this problem, two quasi-Fermi levels E_{Fp} and E_{Fn} are introduced. E_{Fp} describes the occupation of holes in the VB and E_{Fn} describes the occupation of electrons in the CB. This makes it possible to use Fermi-Dirac statistics on the two energy bands separately. The band diagram for an illuminated p-n junction without a bias is shown in Figure 2.4b.

There are no applied voltage on power producing solar cells. However, they are connected to a load, and since the cells behaves like an ideal current source, this results in a voltage $V_a = IR_L$ over the cell, where I is the current the cell delivers and R_L is resistance over the load. This brings the cell out of equilibrium, and the difference between the band edges on the p- and n-side is then given by $q(V_{bi} - V_a)$. The band diagram of such a positive "biased" p-n junction without and with illumination are shown in Figure 2.4c and Figure 2.4d, respectively.

(a) No illumination, zero voltage   (b) Illuminated, zero voltage

(c) No illumination, positive voltage   (d) Illuminated, positive voltage
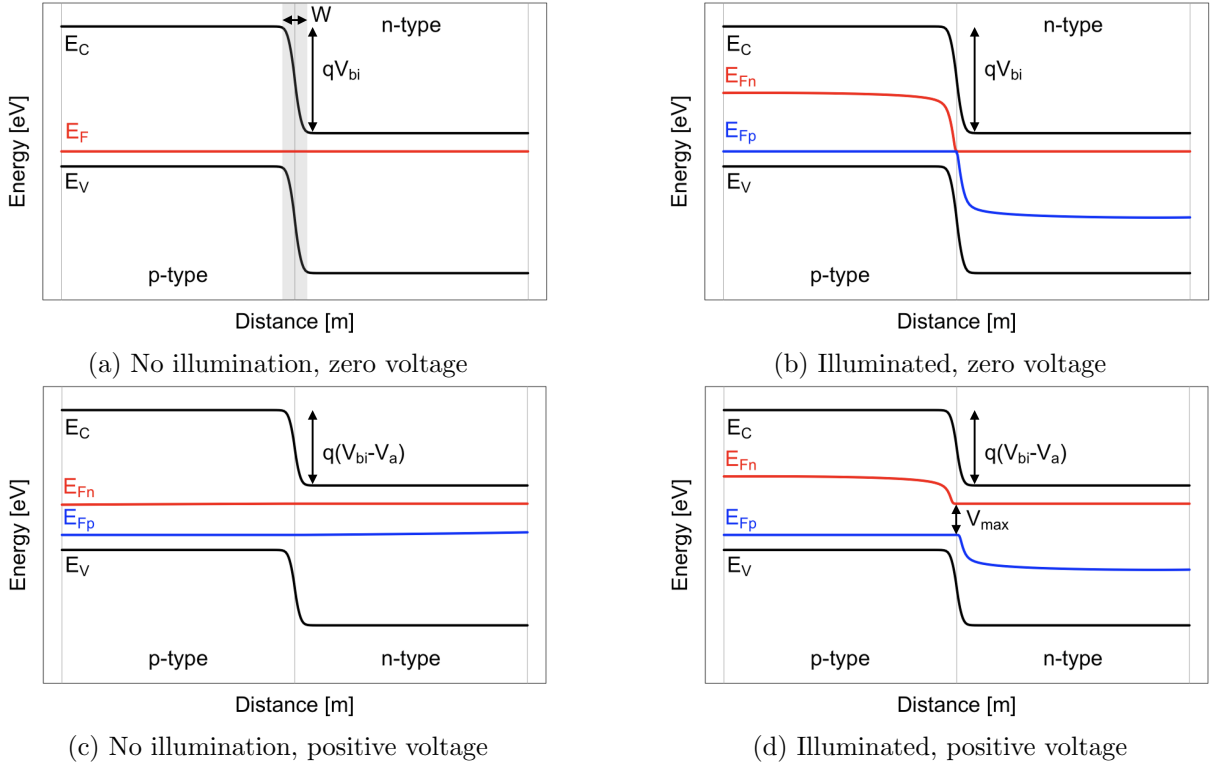
Figure 2.4: Energy band diagrams of a p-n junction under four conditions: (a) No illumination, zero voltage, (b) Illuminated, zero voltage, (c) No illumination, positive voltage, and (d) Illuminated, positive voltage. Figure based on Ref. [18]. E_V and E_C are the VB and CB edges, respectively. E_F is the Fermi level, while E_Fn and E_Fp are the quasi-Fermi levels for electrons and holes, respectively. q is the elemental charge, V_bi the built in potential difference, V_a is the equivalent applied voltage, and V_max is the maximum voltage an illuminated cell can provide. W is the depletion region, and is only indicated in (a).

The maximum voltage an illuminated p-n junction can provide, V_max, is determined by the smallest energy difference between the quasi-Fermi levels as a function of position. Visually, this can be seen in Figure 2.4d, and mathematically, this is given by

$$V_\mathrm{max} = \frac{1}{q}\left(E_\mathrm{Fn} - E_\mathrm{Fp}\right) \tag{2.5}$$

where E_Fn is the quasi-Fermi level of electrons in the n-type semiconductor and E_Fp is the quasi-Fermi level of holes in the p-type semiconductor. All p-n junctions in Figure 2.4 are homojunctions, i.e. the p- and n-doped layers are made of the same semiconductor. In such junctions, there are no band offsets, i.e. no sudden change in either the CB or VB edges. However, this can occur in heterojunctions, i.e. a p-n junction made up of two different semiconductor materials. The vertical position the energy bands of the p- and n-type semiconductors can then be described by Anderson's rule, which states that the vacuum levels of the two materials should be aligned [19]. As a consequence, the electron affinity χ, i.e. the energy required completely remove an electron from the crystal, can be used to derive the band offsets. This is beneficial as the electron affinity is nearly independent of the position of the Fermi level and thus nearly independent of the doping. Using Anderson's rule, a CB offset ΔE_C between two materials A and B can be described as

$$\Delta E_\mathrm{C} \equiv E_\mathrm{C}^B - E_\mathrm{C}^A = \chi^A - \chi^B \tag{2.6}$$

10

where E_C is the energy of the CB edge and χ is the electron affinity. Figure 2.5 illustrates these parameters in for two materials with $E_g^A < E_g^B$ and $\chi^A < \chi^B$. In this thesis, Anderson's rule will be used to mathematically remove band offsets in certain simulated heterojunction cells.
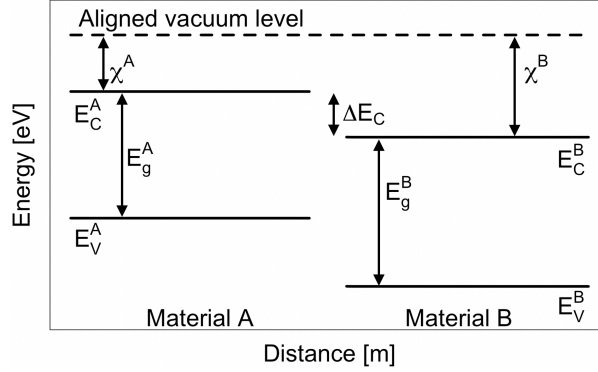
Figure 2.5: Two materials A and B where the vacuum levels of are aligned as described by Anderson's rule. Figure based on Ref. [19]. E_V and E_C are the VB and CB edges, E_g the bandgap, ΔE_C the CB offset, and χ is the electron affinity.

2.1.5 Solar Cell Performance Parameters

In general, IV-curves describes the effect on the current when a voltage is applied to a p-n junction. For an ideal diode, using the sign convention for solar cells, the current I as a function of voltage V is given by

$$I(V) = I_L - I_D = I_L - I_0 \left(\exp\left\{ \frac{qV}{k_B T} \right\} - 1 \right) \tag{2.7}$$

where I_D is the dark current, I_L is the illumination current, I_0 is the dark saturation current, q is the elemental charge, k_B is the Boltzmann's constant, and T is the temperature in Kelvin. Figure 2.6 schematically illustrates an IV-curve for a cell in the dark ($I(V) = I_D$) and an IV-curve for an illuminated cell ($I(V) = I_L - I_D$).
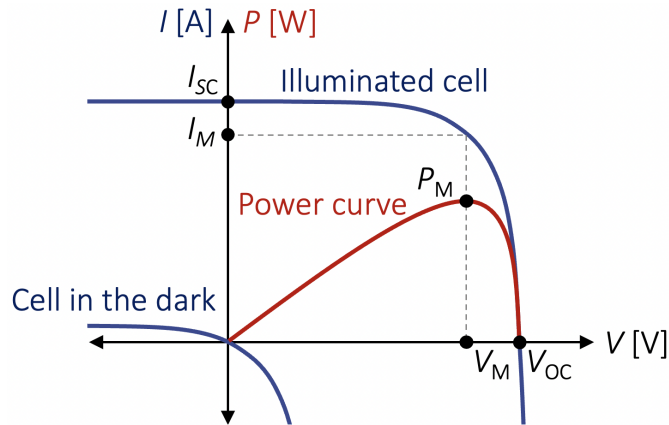
Figure 2.6: IV-curves for a p-n junction in the dark and under illumination, and the corresponding power curve for the illuminated junction. I_{SC} is the short-circuit current, V_{OC} is the open-circuit voltage, P_M is the maximum power point, and I_M and V_M are the current and voltage at P_M, respectively.

Also in Figure 2.6, two solar cell performance parameters are indicated, namely the the short-circuit current I_{SC} and the open-circuit voltage V_{OC}. I_{SC} is the current under illumination at zero voltage. Often, this is instead expressed as the short circuit current density J_{SC}, which is the total short-circuit current per unit area. For silicon solar cells under the AM1.5 spectrum, the maximum value of the J_{SC} is about 46 mA/cm^2. The short-circuit current density can be approximated as

$$J_{SC} = qG(L_n + L_p) \qquad (2.8)$$

where G is the generation rate, and L_n and L_p are the electron and hole diffusion lengths, respectively. The diffusion length is the average length a carrier moves between generation and recombination. This again depends on the lifetime of the electrons and holes, τ_n and τ_p, respectively, by the following equation

$$L_i = \sqrt{D\tau_i} \qquad (2.9)$$

where D is diffusivity. The lifetime is the average time which a carrier can spend in an excited state after electron-hole generation before it recombines, and in general does longer lifetime result in better performing cells. In this thesis, the relationships in both Eq.(2.8) and Eq.(2.9) will be used to describe some effects observed when the design principle by Santhanam and Fan [11] (see section 2.4) is applied to the simulated cells.

The open-circuit voltage is the voltage under illuminating at zero current. It can be expresses as

$$V_{OC} = \frac{nk_bT}{q} \ln \left\{ \frac{I_L}{I_0} + 1 \right\} \qquad (2.10)$$

where n is the ideality factor. Silicon solar cells on high quality single crystalline material under the AM1.5 spectrum can have a V_{OC} of up to 764 mV. In this thesis, some low light intensity simulations were conducted. The V_{OC} varies with the incoming light intensity X by

$$V'_{OC} = V_{OC} + \frac{nk_bT}{q} \ln X \qquad (2.11)$$

By multiplying the current and voltage of a p-n junction under illumination and plotting this against the voltage one obtains the power curve. This curve gives the power produced by the junction at any given voltage. The maximum power produced is denoted the maximum power point P_{max}. The current and voltage at P_{max} are called I_M and V_M, respectively. A power curve, together with P_{max}, I_M, and V_M, are given in Figure 2.6.

Using the performance parameters described above, one can calculate fill factor FF and the efficiency η. The fill factor describes the "squareness" of the IV-curve under illumination, and a high FF can be an indication of a high performing solar cell. Mathematically, it is given by the ratio between P_M and the product of I_{SC} and V_{OC}.

The efficiency describes ratio of the extracted power P_{out} and the incoming power P_{in}. The higher the efficiency, the better, and the theoretical limit for a conventional single junction solar cell is about 33.7%. One can calculate the efficiency by one of the following relations

$$\eta = \frac{P_{\text{out}}}{P_{\text{in}}} = \frac{P_{\text{M}}}{P_{\text{in}}} = \frac{I_{\text{M}}V_{\text{M}}}{P_{\text{in}}} = \frac{V_{\text{OC}}I_{\text{SC}}}{P_{\text{in}}}FF \tag{2.12}$$

Which relation is most useful in Eq.(2.12) depends on which reliable parameters that are available. SCAPS [12] (see section 2.5) in general calculates this automatically. However, during the low light simulations conducted in this thesis, this is done manually using the first relation in Eq.(2.12).

2.2 Intermediate Band Solar Cells

Intermediate band solar cells are not directly relevant to this thesis. However, they are strongly connected to IPV cells, a concept that will be relevant here. Therefore, this section on IBSC are included here for completeness. When nothing else is stated, this and the subsequent section are on chapter 1.29 of the book *Comprehensive Renewable Energy* by E. Antolín *et al.* [20].

2.2.1 The Shockley–Queisser Limit

Continuous research and development over the past decades have pushed the obtainable efficiencies of solar cells. Currently, the record efficiency of a single junction silicon solar cell under one sun conditions is about 26.7%. This it not much lower than the absolute efficiency limit of single junction cells with an optimum bandgap, the Shockley–Queisser (SQ) limit, at about 33.7%. If a substantial increase in solar cell efficiencies is desirable to achieve, which is especially relevant when the available area is limited, novel devices not subject to the SQ limit are required. In general, such devices are known as "third-generation solar cells".

To better understand the potential of third-generation solar cells, it is useful to first discuss two of the limitations of single junction solar cells. Firstly, the efficiency of single-gap solar cells is fundamentally limited by the fact that they only harness a portion of the solar spectrum. All photons with energies lower than the bandgap width cannot generate an electron-hole pair. All photons with energies equal or higher than the bandgap width can generate an electron-hole pair. However, all excess energy with respect to E_{g} will be lost in thermalization processes. We thus face a trade-off: a large bandgap width material will result in fewer absorbed photons, whereas a small bandgap width material will result in more absorbed photons, but a greater amount of energy will be lost due to thermalization. Figure 2.7 shows a semiconductor bandgap E_{g} and a solar spectrum where all photons with wavelength shorter than the highest possible wavelength available for absorption $\lambda(E_{\text{g}})$ is marked. Secondly, as described by Eq.(2.5), the voltage a solar cell can provide is limited by the energy difference between the quasi-Fermi levels. Therefore, the maximum voltage a narrow bandgap material can provide is lower than that of a wide bandgap material.

2.2.2 Principle of the Intermediate Band Solar Cell

One approach to third-generation solar cells is the so-called intermediate band solar cells (IBSC). These cells are characterized by the existence of an isolated electronic energy band, the intermediate band (IB), between the VB and the CB. As depicted in Figure 2.8, the IB divides the main bandgap E_{g} into two sub-bandgaps, E_{L} and E_{H} (L and H denotes *low* and *high*, respectively.) This allows for two generation paths: the conventional one photon absorption directly from the VB to the CB (labeled (1) in Figure 2.8), and the two photon absorption process from the VB to CB via the IB (labeled (2) and (3) in Figure 2.8). The position in of the IB in the figure is arbitrary chosen, but to achieve the highest possible efficiency, the IB should be positioned so that $2E_{\text{L}} \approx E_{\text{H}}$.
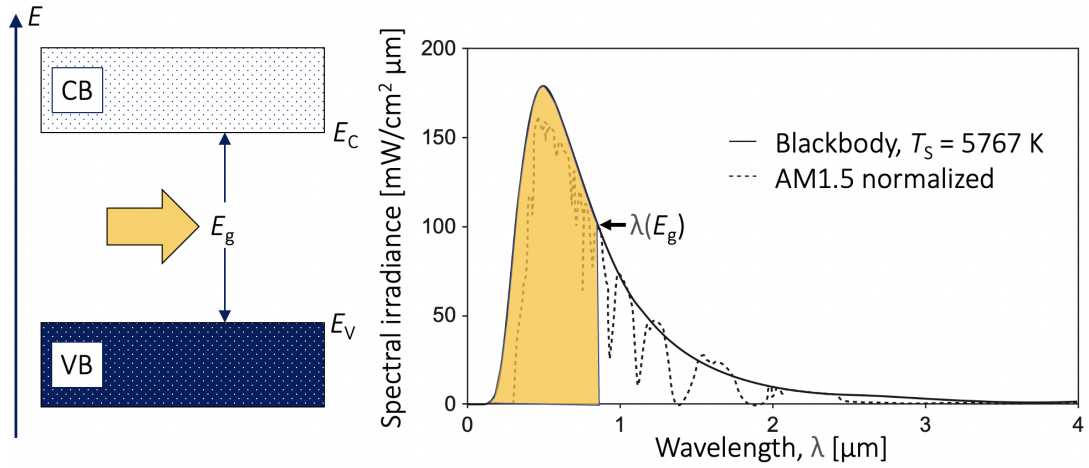
Figure 2.7: Semiconductor bandgap E_g with a solar spectrum where all photons with wavelength shorter than the minimum possible wavelength available for absorption $\lambda(E_g)$ is marked. Spectrum taken from Ref. [21].

The aim of IBSC is to reduce the two efficiency-reducing effects of single junction cells described above. That is, in theory, IBSC manages to capture a larger portion of the solar spectrum while reducing thermalization losses and maintaining a high voltage. The maximum voltage an IBSC can provide V_{max} is illustrated in Figure 2.8. This is independent of the Fermi level of the IB $F_{F,IB}$, and Eq.(2.5) still holds true. Thus, if a large E_g is used, a high voltage can be achieved. The increased fraction of the solar spectrum harnessed is due to the additional generation path via the IB. Photons with lower energy than the main bandgap width E_g can now be absorbed by the two sub-bandgaps. Figure 2.9 schematically illustrates an IB semiconductor with a solar spectrum where the the highest possible photon wavelengths $\lambda(E_g)$, $\lambda(E_H)$, and $\lambda(E_L)$ available for absorption for the main-bandgap, the high-bandgap, and the low-bandgap, respectively, are indicated. Comparing the solar spectra where the available photons for absorption are marked for single junction solar cells and IBSC (Figure 2.7 and Figure 2.9, respectively), one can qualitatively see that this is IBSC can absorb a higher number of photons.

Figure 2.8: Schematic illustration of the energy band diagram to an IBSC under working conditions (illuminated and connected to a load). See text for details. Figure based on Ref. [20].

14

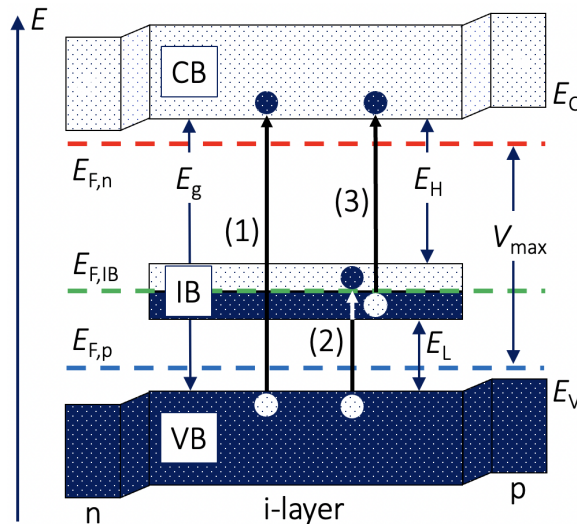In ideal conditions, IBSC can reach efficiencies of about 49.4%. However, as of 2022, the highest recorded efficiency of an IBSC is around 19% [9]. In contrary to real IBSC, ideal IBSC among others only regard radiative recombination, have optimum placement and widths of the bandgaps, and have optimal absorption coefficients.
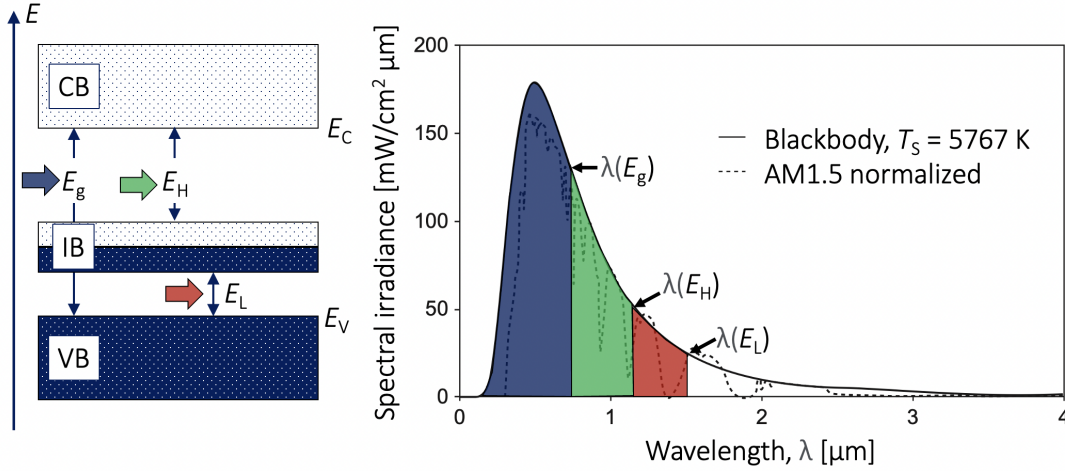

Figure 2.9: The left figure shows a semiconductor with an IB where the main-bandgap E_{g}, the high-bandgap E_{H}, and the low-bandgap E_{L} are indicated. The right figure shows the solar spectrum where all photons available for absorption are marked until the maximum wavelengths $\lambda(E_{\text{g}})$, $\lambda(E_{\text{H}})$, and $\lambda(E_{\text{L}})$ for E_{g}, E_{H}, and E_{L}, respectively. Spectrum taken from Ref. [21].

2.2.3 The Impurity Based Approach

It is known that dopants or impurities can create discrete states in the bandgap, sometimes distant from the band edges in so-called deep-level (DL) states. These DL states can allow for a two-step generation path, i.e. exactly what we want in IBSC. Logically, a suggestion to make IBSC is thus to strategically dope semiconductors with with appropriate DL impurities. This method is called the the impurity based approach.

When using the impurity based approach to make IBSC, one needs the introduced states to form a *band*. In this context, the significance of the term band is related to the assumption that the intermediate states should not act as SRH recombination centers. This is because isolated DL states, i.e. not in a band, promotes non-radiative SRH recombination which is a loss mechanism. However, if the states rater exists in a band, the non-radiative SRH recombination is suppressed and only band-to-band radiative recombination remains [22]. The following paragraphs explains why this behavior is observed and the suggested method to ensure band formation.

When a non-radiative recombination process occurs, the energy must be absorbed by other electrons (Auger recombination) or by phonons. For DL states, phonons are the only particle that realistically can absorb this energy. However, the energy a single phonon can absorb is low compared to the bandgap width, and thus many phonons are required. The probability that many phonons are emitted simultaneously in one process is to low to justify the observed non-radiative SRH recombination. Therefore, the energy absorption must be explained by a more complex model, the so-called Lattice Relaxation Multiple-Phonon Emission (MPE) mechanism [20].

The origin of the MPE mechanism lies in the different behavior a DL state and a band disperses energy from a charge carrier. In the bands, the electrons are characterized by Bloch functions extending across the whole crystal. In the DL states, the electrons are instead characterized by localized wavefunctions. In a transition from a band to a DL state, a charge formerly dis-

tributed across the whole structure suddenly becomes localized in the DL state. This change makes the state heavily vibrate to recover equilibrium. During this vibration, successive emission processes of phonons occurs through ordinary phonon–electron interaction, i.e. the MPE mechanism.

The MPE mechanism is based on the premise that the wavefunction of the DL state is localized. The process can thus be prevented if we are able to transition these wavefuncitons from being localization to being delocalization. To achieve this, we can increase the density of traps, i.e. increase the DL doping concentration. This is because above a certain doping concentration, the screening between the DL states is strong enough to counteract the Coulomb potential produced by a localized charge. In other words, above a critical doping density, the impurities are close enough as to experience interaction and their levels split into bands. When the DL states have delocalized and formed an IB in the bandgap, a transition from e.g. the CB to the IB does not change how the charge was distributed. Therefore, the recombination process will no longer be the MPE mechanism, but rather radiative recombination. Figure 2.10 schematically illustrates (1) localized states, (2) deloalized states, and (3) an IB.
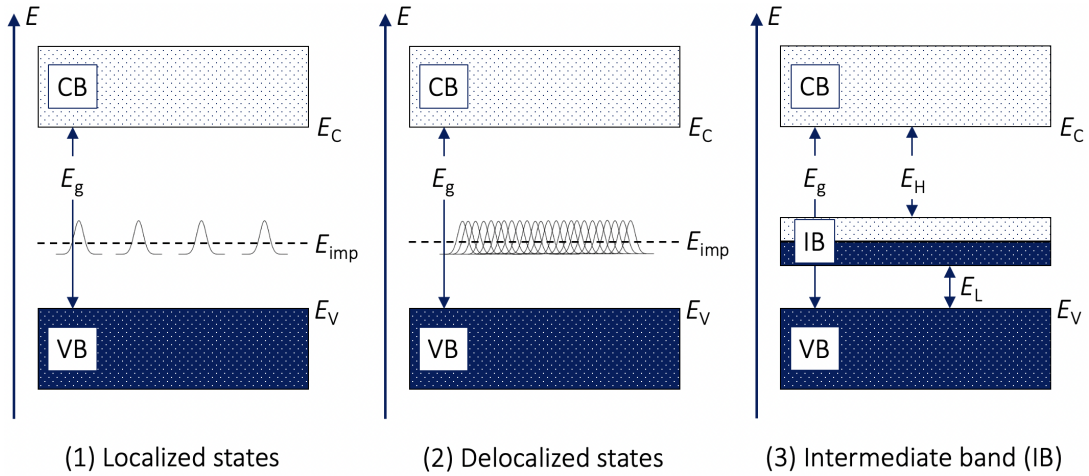
Figure 2.10: Schematic illustration of (1) deep-level states at low concentration where the states are localized, (2) deep-level states at high concentration where the states are delocalized, and (3) deep-level states that have formed an partially based intermediate band. Figure based on Ref. [20].

2.3 The Impurity Photovoltaic Effect

Currently, one of the main challenges to realize high-efficiency IBSC is that the delocalization of the DL states might be difficult to achieve. This is especially true if one aims to keep a high crystalline quality of the semiconductor material to be doped. If delocalization does not occur, the result when aiming to fabricate an IBSC could rather be an impurity photovoltaic (IPV) cell. Therefore, it is important to understand the IPV effect.

2.3.1 IPV Effect v. IBSC

The main difference between IPV cells and IBSC is that the introduced DL states are localized in IPV cells. Using the reasoning as presented in subsection 2.2.3 about the impurity based approach, it is then clear that non-radiative SRH recombination will be present in IPV cells. Also, IPV cells does not actually have the two additional sub-bandgaps E_L and E_H, as there

they do not have the IB. However, for convenience is this notation often (incorrectly) used in IPV cells as well, and this thesis will be no exception to this. Apart from this do they share several similarities. Both allows for an additional two-step generation path via the introduced states, and both have the same fundamental efficiency limit.

If one excludes Auger processes are there in theory twelve transitions that can take place in an IPV cell. The generation (electron excitation from the VB to the CB) and emission (electron excitation from or to an impurity) can either be induced by phonons (thermal) or by photons (optical). Similarly, the reverse processes recombination and capture either releases phonons or photons. In Figure 2.11, all these twelve transitions are illustrated. However, it should be noted that not all models of the IPV effect differentiate between all twelve transitions. For example, Keevers and Green [23] only include ten transitions as they do not differentiate between optical and thermal capture of charge carriers and view all energy released in the capture processes as lost. Also, experimental studies on the IPV effect often does not differentiate between thermal and optical recombination/capture as this would require a set-up that detects whether the processes releases phonons or photons.

The introduced impurities in IPV cells can either increase or reduce the efficiency of an identical impurity-free cell, depending on whether the generation or recombination rates via the impurities is greatest, respectively. This again depends on several factors, where only the two most important for this thesis are presented here. Firstly, the capture cross section (CCS) for electrons and holes σ^n and σ^p, respectively, in a semiconductor describes the effectiveness of the defect to capture a carrier. Using Figure 2.11, it can be seen as a measure of the area of the stippled line for E_{imp}. A higher CCS will in general result in a higher SRH recombination rate and lower efficiency. Secondly, impurity density N_t is the concentration of impurities. Using Figure 2.11, it can be seen as a measure of the number of impurities on the stippled line for E_{imp}. N_t should neither be too high nor too low if the optimum efficiency is to be achieved.
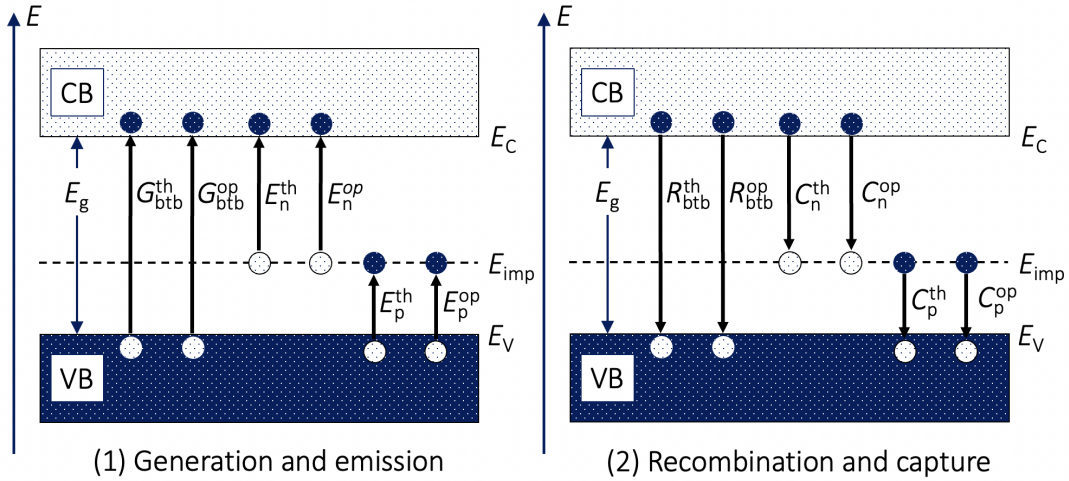
Figure 2.11: The twelve possible transition (not including Auger processes) in IPV cells with one impurity energy level E_{imp}. G, E, R, and C denotes generation, emission, recombination, and capture, respectively. th and op denotes thermal and optical, respectively, and corresponds to the capture or emission of a phonon or photon, respectively. Finally, btb, n, and p denotes a band-to-band transition, a transition between the CB and the impurity, and a transition between the VB and the impurity, respectively. Figure based on Ref. [18].

2.4 Suppressing Non-radiative Recombination via Inhomogeneous Doping

In the paper *Suppressing non-radiative generation and recombination in LEDs, PVs, and photodiode detectors via inhomogeneous doping around the depletion region co-located with a heterojunction* by Santhanam and Fan, an improved design principle for photonically-active heterojunction diodes is presented [11]. In short this principle utilizes spatial control over the doping concentrations to suppress non-radiative SRH recombination processes. This is beneficial since non-radiative processes can constitute major losses. The design principle is general to all diodes with carrier-confining heterojunctions. For power producing diodes, i.e. solar cells, the redesigned devices exhibit higher open-circuit voltages and efficiencies, with significant improvement in cells with high defect densities. As this design principle will be utilized in the simulations conducted in this thesis, the following subsections explains the theory behind the principle and the effect the redesign had on the PV diodes in the paper in Ref. [11].

2.4.1 SRH Recombination Rates Outside and Inside the Depletion Region

In Eq.(2.7), the current in an *ideal* diode solar cell is given. However, in real solar cells, an additional factor, the ideality factor n must be included to correctly describe the current. The ideality factor is a measure of how closely the current in the diode follows the ideal diode equation. It is a number between 1 and 2 which typically increases as the current decreases. Including this factor the diode equation then becomes

$$I(V) = I_{\mathrm{L}} - I_0 \left(\exp \left\{ \frac{qV}{nk_{\mathrm{B}}T} \right\} - 1 \right) \tag{2.13}$$

Several assumptions are made in the derivation of the ideal diode equation, i.e. Eq.(2.13) with $n = 1$. Relevant here is that it assumes that all SRH recombination occurs outside the depletion region. However, SRH recombinatoin *does* occur within the depletion region, and to correctly include this in the diode equation an ideality factor of $n = 2$ must be used.

In the context of this thesis, the important consequence of the change in ideality factor inside and outside the depletion region here is that the SRH recombination rate scales differently with respect to the voltage outside and inside the depletion region. Figure 2.12 schematically illustrates this by showing the radiative and SRH recombination rates at voltage V_0 and $V_0 + V > V_0$ around the depletion region in a p-n junction. As can be seen in the figure, when the voltage decreases, the decrease in SRH recombination is much greater outside the depletion region than within. Therefore, as the bias is decreased, the relative impact of depletion region SRH recombination increases and becomes the primary non-radiative pathway. This is often the case for cells where the open-circuit voltage is low relative to the bandgap.

The essence of the design principle is to limit the peak of the SRH recombination. This is done by manipulating the doping profiles in the vicinity of the depletion region in p-n heterojunctions. The SRH recombination rate peak coincides with the mid-gap energy crossing the defect level. In the paper Santhanam and Fan show that the local SRH recombination rate density R_{SRH} at this peak is in fact proportional to the intrinsic concentration n_{i}, a quantity which is smaller in the wider bandgap layer than in the narrow bandgap layer. By changing the doping concentrations around the depletion region, the peak of the SRH recombination rate can be displaced into the wider bandgap side of the heterojunction. The rate is thus reduced in proportion to n_{i}, meaning it is reduced exponentially in the ratio of the bandgap difference to $2k_{\mathrm{B}}T$. The impact on device efficiencies at low voltages is thus expected to be substantial. It should be noted that

the type of doping in the layer is not essential to this design principle, i.e. it can be applied to either the case of an n-type or a p-type narrow bandgap layer.

One could question the necessity of *inhomogeneous* doping to utilize this design principle. In other words, why would not a new, homogeneous doping concentrating not be sufficient? The rationale is simply that the doping of these layers are, prior to the design change, chosen for particular reasons that continue to impact device performance. Lateral current spreading is necessary, which in turn necessitates reasonably high doping in these current spreading layers to limit the newly introduced series resistance. Since the current spreads in the outer carrier-confinement layers, reducing the doping here would increase series resistance. Thus, the inhomogeneous aspect of the design provides a benefit over simply changing the doping of the entire layer.
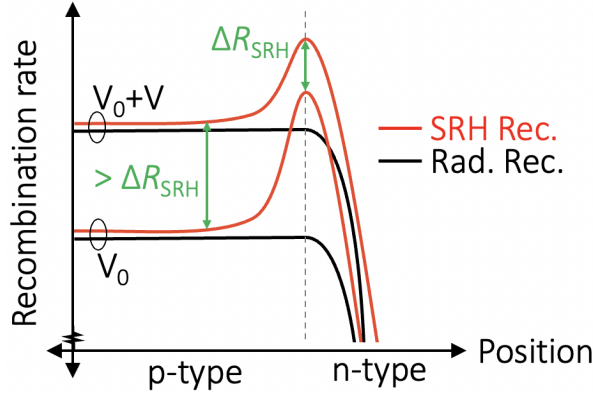
Figure 2.12: Schematic illustration of the SRH recombination (SRH Rec.) and the radiative recombination (Rad. Rec.) around the depletion region in a p-n junction. The two pairs of lines are given for a voltage V_0 and $V_0 + V > V_0$. The difference in SRH recombination ΔR_{SRH} is lower in the middle of the depletion region (stippled vertical line) than ouside. Figure based on Ref. [11].

2.4.2   Design Example and Results

In the paper by Santhanam and Fan in Ref. [11] they simulated a p-InP/p-GaInAsP/p-GaInAsP/n-InP/n-InP cell. They initially did the simulations with a uniform doping concentration, and then again where they applied the design principle by changing the doping concentrations around the depletion region. The materials they used and their thickness and doping concentrations are summarized in Table 2.1.

Table 2.1: Thicknesses, materials and doping concentration of the solar cells simulated by Santhanam and Fan in Ref. [11]. The values that changes from the forth to the fifth column are colored in orange.

Layer #	Thickness [nm]	Material	Basline Doping $|N_{\text{D}} - N_{\text{A}}|$ [cm^{-3}]	Redesigned Doping $|N_{\text{D}} - N_{\text{A}}|$ [cm^{-3}]
5	500	p-InP	$2.0 \cdot 10^{18}$	$2.0 \cdot 10^{18}$
4	980	p-GaInAsP	$2.0 \cdot 10^{18}$	$2.0 \cdot 10^{18}$
2	20	p-GaInAsP	$2.0 \cdot 10^{18}$	$4.0 \cdot 10^{18}$
2	40	n-InP	$2.0 \cdot 10^{18}$	$1.0 \cdot 10^{18}$
1	460	n-InP	$2.0 \cdot 10^{18}$	$2.0 \cdot 10^{18}$

Their results showed that the positive impact of the design change is minimal for higher quality devices with longer SRH lifetimes. This is because in these devices other recombination processes

not affected by the changes dominates. However, for lower quality devices with shorter SRH lifetimes the impact of the design change was found to have a significant, positive effect. This means that the design principle is among others relevant for devices with high defect densities and low open-circuit voltages.

2.4.3 Applicability to IPV Cells

As described in section 2.3, IPV cells only benefits from the introduced defects if the generation-to-recombination rate via the impurities is greater than one. However, this can be difficult to achieve, and early-stage IPV cells most likely will have high SRH recombination rates. It could therefore be hugely beneficial if one were able to apply the design principle described above with its positive effect to IPV cells, and this is the basis for this thesis.

The design principle is only applicable to heterostuctures. It have been suggested that both IPV cells and IBSC can be made of oxides. Oxides can often only be either p- or n-doped, i.e. it is difficult to make a p-n junction using the same oxide. Thus, oxide junctions is most often heterostuctures, and can theoretically benefit from the design principle.

2.5 Simulation Program: SCAPS

This section presents relevant theory on the simulation program used this thesis. It is based on the SCAPS manual [12], the specialization project of Tore Bysting [24], and Stine Hansen's master thesis [16]. The version of the software used is SCAPS 3.3.10. No guide of the SCAPS user interface or a standard simulation procedure will be given. Instead, the interested reader can be find this in Hansen's master thesis [16].

2.5.1 About SCAPS

SCAPS (a Solar Cell Capacitance Simulator) is a one dimensional solar cell simulation program developed at the Department of Electronics and Information Systems (ELIS) of the University of Gent, Belgium. The researchers behind the program are A. Niemegeers, M. Burgelman, K. Decock, S. Degrave, and J. Verschraegen. Originally, it was developed for cell structures of the CuInSe$_2$ and the CdTe family. However, recent developments make the program now also applicable to crystalline solar cells (Si and GaAs family) and amorphous cells (a-Si and micromorphous Si).

In SCAPS one can define a solar cell with a maximum of seven layers, in addition to a front and back contact. The interfaces between each layer can also be defined. In each layer, several material properties such as thickness, doping concentrations, carrier mobilities, recombination rates and defects can be set. The light absorption of each material must be set, either through a model or a file containing the absorption coefficient as a function of wavelength. Care should be taken when choosing the simulations parameters, as extreme values might result in unrealistic results and possibly reduce the stability of the program.

2.5.2 SCAPS Equations

SCAPS simulates solar cells by numerically solve three one-dimensional semiconductor equations: the Poisson equation and the continuity equations for electrons and holes, respectively. In this order, in the bulk of the layers, these are given by

$$\frac{\partial}{\partial x}\left(\varepsilon\frac{\partial \Psi}{\partial x}\right) = -\frac{q}{\varepsilon_0}\left[-n + p - N_{\mathrm{A}}^- + N_{\mathrm{D}}^+ + \frac{1}{q}\rho_{\mathrm{defect}}(n,p)\right] \tag{2.14}$$

$$-\frac{\partial j_\text{n}}{\partial x} + G - U_\text{n}(n, p) = \frac{\partial n}{\partial t} \tag{2.15}$$

$$-\frac{\partial j_\text{p}}{\partial x} + G - U_\text{p}(n, p) = \frac{\partial p}{\partial t} \tag{2.16}$$

where ε and ε_0 is the permittivity of vacuum and the semiconductor, respectively, x is the distance, Ψ is the electrostatic potential, q is the electronic charge, n and p are the free carrier concentrations of electrons and holes, respectively, N_A^- and N_D^+ are the density of ionized acceptors and donors, respectively, $\rho_\text{defect}(n, p)$ is the charge density of defects, j_n and j_p are the electron and hole current densities, respectively, G is the volume rate of generation, t is the time, and $U_\text{n}(n, p)$ and $U_\text{p}(n, p)$ are the volume rates of recombination for electrons and holes, respectively.

To calculate the electron and hole current densities from Eq.(2.15) and Eq.(2.16), respectively, SCAPS uses the following two equations,

$$j_\text{n} = -\frac{\mu_\text{n}}{q} n \frac{\partial E_\text{Fn}}{\partial x} \tag{2.17}$$

$$j_\text{p} = -\frac{\mu_\text{p}}{q} p \frac{\partial E_\text{Fp}}{\partial x} \tag{2.18}$$

where μ_n and μ_p are the carrier mobilities for electrons and holes, respectively, and E_Fn and E_Fp are the quasi-Fermi levels for electrons and holes, respectively.

Combining the equations above with appropriate boundary conditions gives a system of coupled differential equations. When SCAPS runs a simulation, these equations are solved iteratively. Each simulation gives three types of results. Firstly, one can choose one parameter to be varied, and measure its effect on another parameter. This result is represented graphically. Secondly, some key values are calculated, such as the open-circuit voltage V_OC, the short-circuit current density J_SC, the fill factor FF and the efficiency η. Finally, graphs of the energy band diagrams, occupation probabilities for defects and generation-recombination profiles are displayed.

2.5.3 IPV Effect in SCAPS

In SCAPS, the SRH recombination and generation via the impurities are not considered separate mechanisms. Instead, a net SRH recombination rate which is equal to the capture minus the emission via the impurity is calculated. If this net value is negative, the cell experiences a higher generation rate than recombination rate via the impurities. Therefore, a negative net SRH recombination rate indicates that the IPV effect has a net positive impact on the cell.

The IPV effect implemented by SCAPS is a slightly modified version of the model of Keevers and Green [23]. Of the twelve theoretical possible transitions in IPV cells (described in subsection 2.3.1), only nine are considered by SCAPS. It combines optical and thermal capture/recombination, both directly from the CB to the VB and via the impurity, to a single capture term. This means that SCAPS used a single term for the band-to-band recombination called *Radiative recombination* which in reality is the sum of both optical and thermal recombination. This merger of two terms is also used for the optical and thermal capture of both electrons and holes by the impurities. In SCAPS, these two therms are referred to as "hole capture" and "electron capture".

Chapter 3

Methods

This chapter provides the necessary simulation input parameters to replicate the simulations conducted in this thesis. All simulations were done using SCAPS version 3.3.10 [12].

The chapter consists of two main parts. First, section 3.1 summarizes the fixed parameters for all simulations. Then, the remaining sections presents the varied and fixed parameters for each set of cells. Most input parameters are identical between the sets of cells. However, due to ease of replication, the parameters are repeated in all sections. To clearly indicate which parameters that differs between similar cells, are these values colored in orange. The subsequent list presents the sets of cells and their respective section.

- Initially, section 3.2 is a replication of the GaInAsP/InP cells by Santhanam and Fan in Ref. [11]. These cells consist of five layers and there are impurities in all of them, leading to SRH recombination.

- Next, section 3.3 applies the design principle to p-GaAs/n-AlGaAs cells. These cells consist of four layers and there are impurities in all of them.

- In section 3.4, the CB offset present in the cells in section 3.3 is removed to make modified p-GaAs/n-AlGaAs cells, and the design principle is then applied to these cells. These cells also consist of four layers and there are impurities in all of them.

- In section 3.5, the design principle is applied to GaAs homojunction cells. Again does these cells also consist of four layers and there are impurities in all of them.

- Then, in section 3.6, are the IPV cells introduced. Here, the design principle is applied to GaAs homojunction IPV cells. The cells in this section consists of five layers where only the middle layer has impurities, now contribution to both generation and recombination.

- Next, section 3.7 repeats the simulations in section 3.6 but using modified CB offset free p-GaAs/i-GaAs/n-AlGaAs IPV cells. These cells also consists of five layers where only the middle layer has impurities.

- Finally, in section 3.8 are the the simulations in section 3.7 repeated, but using modified band offset free p-AlGaAs/i-GaAs/n-AlGaAs IPV cells. Again, these cells also consists of five layers where only the middle layer has impurities.

3.1 Fixed Parameters for all Simulations

Table 3.1 and Table 3.2 summarizes the fixed parameters for the main menu and the contacts, respectively. All other fixed parameters not presented in these tables are given in the list below.

- The cells are illuminated from the right, voltage is applied to the left contact, and the current reference is set to "generator".
- No interface properties are defined.
- Tunneling is not allowed.
- There is no grading applied to neither defects nor the semiconductor layers.
- Where nothing else is stated is the transmission set to 100%.

Table 3.1: Main interface fixed settings for all SCAPS simulations. All settings are based on Stine Hansen's master thesis [16].

Setting/Parameter	Value
Working point settings	
Temperature	300 K
Voltage	0.0 V
Frequency	10^6 Hz
Number of points	5
Resistance and Illumination Settings	
Series resistance	No
Shunt resistance	No
Illumination	Light
Specify illumination spectrum, then calculate G(x) / Directly specify G(x)	Specify illumination spectrum, then calculate G(x)
Analytic model for spectrum / Spectrum from file	Spectrum from file
Illuminated from	Right
Spectrum file name	AM1_5G 1 sun.spe
Spektrum cut off	No
Neutral Density	0.0

Table 3.2: Fixed settings for the contacts for all SCAPS simulations.

Contact settings		
Parameter	**Value**	**Ref.**
Electron surface recombination velocity, left contact	10 cm/s	[25]
Hole surface recombination velocity, left contact	10^7 cm/s	[25]
Electron surface recombination velocity, right contact	10^7 cm/s	[25]
Hole surface recombination velocity, right contact	10 cm/s	[25]
Flat bands	Yes	NA
Optical filter	On	NA
Optical filter from value/file	From value	NA
Filter Mode	Reflection	NA
Filter value, left (back) contact	100 %	NA
Filter value, right (front) contact	0.0 %	NA

3.2 GaInAsP/InP Cells

The GaInAsP/InP cells are, to best possible extent, a replication of the work conducted by Santhanam and Fan in Ref. [11]. The cells consist of five layers, from left to right: p-InP, p-GaInAsP, p-GaInAsP, n-InP, and n-InP, and all of them have impurities. Their thicknesses are 500 nm, 980 nm, 20 nm, 40 nm, and 460 nm, respectively. This is schematically illustrated in Figure 3.1, where the red color indicates p-type and the blue color n-type.
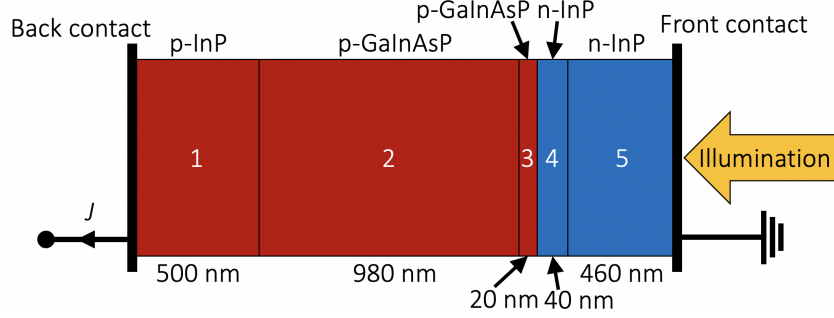

Figure 3.1: Schematic illustration of the structure of the GaInAsP/InP cells.

3.2.1 Varied Parameters

In total, three GaInAsP/InP cells were simulated. These are labelled *GaInAsP/InP - Ref.*, *GaInAsP/InP - Hom.*, and *GaInAsP/InP - Inhom.* The *GaInAsP/InP - Ref.* cell is free of impurities and has a uniform doping concentration through all layers. The *GaInAsP/InP - Hom.* cell has impurities and a uniform doping concentration through all layers. The *GaInAsP/InP - Inhom.* cell has impurities and has a inhomogeneous doping concentration in layers 3 and 4 with respect to layers 2 and 5 (see Figure 3.1). The doping concentration in layer 3 is increased while the doping concentration in layer 4 is decreased. Table 3.3 summarizes this paragraph and provides the numeric values of the doping concentrations.

Table 3.3: All varied parameters between the GaInAsP/InP cells. The names below the second line in the first column represents the X in *GaInAsP/InP - X*. Next, *Imp.* in the second column is an abbreviation for impurities. The orange color indicates the values that changes from the previous row. All values are taken from Ref. [11].

X	With $Imp.$	1: p-InP N_A [cm^{-3}]	2: p-GaInAsP N_A [cm^{-3}]	3: p-GaInAsP N_A [cm^{-3}]	4: n-InP N_D [cm^{-3}]	5: p-InP N_D [cm^{-3}]
Ref.	No	$2.0 \cdot 10^{18}$	$2.0 \cdot 10^{18}$	$2.0 \cdot 10^{18}$	$2.0 \cdot 10^{18}$	$2.0 \cdot 10^{18}$
Hom.	Yes	$2.0 \cdot 10^{18}$	$2.0 \cdot 10^{18}$	$2.0 \cdot 10^{18}$	$2.0 \cdot 10^{18}$	$2.0 \cdot 10^{18}$
Inhom.	Yes	$2.0 \cdot 10^{18}$	$2.0 \cdot 10^{18}$	$4.0 \cdot 10^{18}$	$1.0 \cdot 10^{18}$	$2.0 \cdot 10^{18}$

3.2.2 Fixed Parameters

Table 3.4 provides the fixed material, recombination, and absorption parameters for the three GaInAsP/InP cells. Then, Table 3.5 provides the defect parameters used in the *GaInAsP/InP - Hom.* and *GaInAsP/InP - Inhom.* cells.

Table 3.4: Fixed material parameters for all InP/GaInAsP cells. All numerical values are based on the values provided by *Ioffe Institute* [26]. The absorption interpolation model is provided by SCAPS [12].

Variable	n-InP/p-InP	p-GaInAsP
Material Parameters		
Bandgap [eV]	1.344	1.100
Electron affinity [eV]	4.380	4.390
Dielectric permitivity [relative]	12.500	13.000
CB effective density of states [cm^{-3}]	$5.7 \cdot 10^{17}$	$2.1 \cdot 10^{17}$
VB effective density of states [cm^{-3}]	$1.1 \cdot 10^{19}$	$9.6 \cdot 10^{17}$
Electron thermal velocity [cm/s]	$3.9 \cdot 10^{7}$	$4.5 \cdot 10^{7}$
Electron thermal velocity [cm/s]	$1.7 \cdot 10^{7}$	$1.8 \cdot 10^{7}$
Hole thermal velocity [cm/s]	$1.0 \cdot 10^{3}$	$1.0 \cdot 10^{3}$
Electron mobility [cm^{2}/Vs]	$1.8 \cdot 10^{2}$	$1.0 \cdot 10^{2}$
Recombination Model		
Radiative recombination coefficient [cm^{3}/s]	$1.2 \cdot 10^{-10}$	$1.2 \cdot 10^{-10}$
Auger electron capture coefficent [cm^{6}/s]	$9.0 \cdot 10^{-31}$	$1.1 \cdot 10^{-31}$
Auger hole capture coefficent [cm^{6}/s]	$9.0 \cdot 10^{-32}$	$1.1 \cdot 10^{-31}$
Absorption interpolation model		
Model	$\alpha(\lambda) = (h\nu(\lambda) - E_\mathrm{g})^{0.5}$	

Table 3.5: Fixed defect parameters used in the three InP/GaInAsP cells with defects.

Defect properties	
Variable	**Input**
Defect type	Neutral
Capture cross section electrons [cm^{2}]	$1.0 \cdot 10^{-15}$
Capture cross section holes [cm^{2}]	$1.0 \cdot 10^{-15}$
Energetic distribution	Single
Reference for defect energy level E_t	Above E_i
Energy level with respect to reference [eV]	0.000
N_t total [cm^{-3}]	$1.0 \cdot 10^{15}$

3.3 GaAs/AlGaAs Cells

The simulated GaAs/AlGaAs cells consists of four layers: p-GaAs, p-GaAs, n-AlGaAs, and n-AlGaAs, and all of them have impurities. Their thicknesses are 480 nm, 20 nm, 40 nm, and 460 nm, respectively. This is schematically illustrated in Figure 3.2.

The fraction of aluminium in Al$_x$Ga$_{1-x}$As is given by a number x between 0 and 1, while the fraction of Ga is given by $1-x$. For $x = 0.3$, i.e. Al$_{0.3}$Ga$_{0.7}$As, does the material have a direct bandgap, and it is the value for x chosen for all simulations including AlGaAs in this thesis. Thus, the Al fraction is mostly omitted hereafter.

3.3.1 Varied Parameters

Except from an initial cell labelled *AlGaAs - Imp. free*, all cells this section have impurities. The only other parameter varied was then the doping concentration. Numerous configurations of different doping concentrations in the four layers of the GaAs/AlGaAs cells were simulated. Of these, the seven most interesting are labelled *AlGaAs - X*, where X describes the specific features of the cell. The H and L in the names denotes whether the doing concentration in

the third and fourth layer is *higher* or *lower* than the doping concentration in the first and fourth layer, respectively. The names of the cells and the corresponding doping profiles are summarized in Table 3.6.
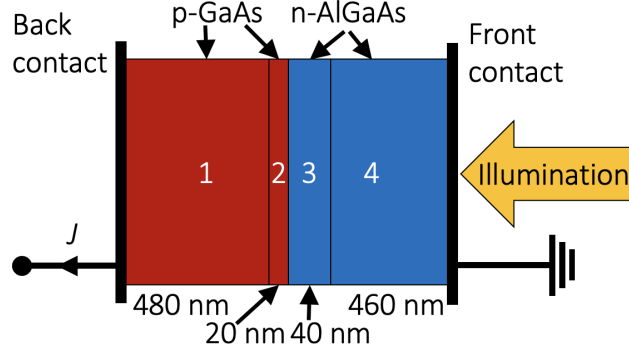

Figure 3.2: Schematic illustration of the structure of the GaAs/AlGaAs cells.

Table 3.6: The seven most interesting GaAs/AlGaAs cells. They are denoted *AlGaAs - X*, where X describes the specific features of the cell. The orange color in table represents values that changes from the previous row. The initial values is are based on a qualified guess and the subsequent values are based on the subsequent results, and thus no source is given.

Cell	Imp.	Doping Cons. $|N_{\mathrm{D}} - N_{\mathrm{A}}|$ $[\mathrm{cm}^{-3}]$			
		Layer 1	Layer 2	Layer 3	Layer 4
AlGaAs - Imp. free	No	$2.0 \cdot 10^{17}$	$2.0 \cdot 10^{17}$	$2.0 \cdot 10^{17}$	$2.0 \cdot 10^{17}$
AlGaAs - Imp.	Yes	$2.0 \cdot 10^{17}$	$2.0 \cdot 10^{17}$	$2.0 \cdot 10^{17}$	$2.0 \cdot 10^{17}$
AlGaAs - HL	Yes	$2.0 \cdot 10^{17}$	$4.0 \cdot 10^{17}$	$1.0 \cdot 10^{17}$	$2.0 \cdot 10^{17}$
AlGaAs - LH	Yes	$2.0 \cdot 10^{17}$	$1.0 \cdot 10^{17}$	$4.0 \cdot 10^{17}$	$2.0 \cdot 10^{17}$
AlGaAs - HH	Yes	$2.0 \cdot 10^{17}$	$4.0 \cdot 10^{17}$	$4.0 \cdot 10^{17}$	$2.0 \cdot 10^{17}$
AlGaAs - Uni.	Yes	$9.0 \cdot 10^{17}$	$9.0 \cdot 10^{17}$	$9.0 \cdot 10^{17}$	$9.0 \cdot 10^{17}$
AlGaAs - Uni., HH	Yes	$9.0 \cdot 10^{17}$	$2.0 \cdot 10^{18}$	$2.0 \cdot 10^{18}$	$9.0 \cdot 10^{17}$

3.3.2 Fixed Parameters

Table 3.7 provides the fixed material, recombination, and absorption parameters for the GaAs/AlGaAs cells. Then, Table 3.8 provides the defect parameters used in all GaAs/AlGaAs cells with impurities.

Table 3.7: Fixed material parameters for all GaAs/Al$_{0.3}$Ga$_{0.7}$As cells. All values are based on the values provided by *Ioffe Institute* [26].

Variable	p-GaAs	n-Al$_{0.3}$Ga$_{0.7}$As
Material Parameters		
Bandgap [eV]	1.424	1.798
Electron affinity [eV]	4.070	3.740
Dielectric permitivity [relative]	12.900	12.050
CB effective density of states [cm^{-3}]	$4.7 \cdot 10^{17}$	$6.5 \cdot 10^{17}$
VB effective density of states [cm^{-3}]	$9.0 \cdot 10^{18}$	$1.1 \cdot 10^{19}$
Electron thermal velocity [cm/s]	$4.4 \cdot 10^{7}$	$3.8 \cdot 10^{7}$
Electron thermal velocity [cm/s]	$1.8 \cdot 10^{7}$	$1.7 \cdot 10^{7}$
Hole thermal velocity [cm/s]	$4.0 \cdot 10^{3}$	$2.3 \cdot 10^{3}$
Electron mobility [cm^2/Vs]	$2.0 \cdot 10^{2}$	$1.5 \cdot 10^{2}$
Recombination Model		
Radiative recombination coefficient [cm^3/s]	$7.2 \cdot 10^{-10}$	$1.8 \cdot 10^{-10}$
Auger electron capture coefficent [cm^6/s]	$1.0 \cdot 10^{-31}$	$1.0 \cdot 10^{-31}$
Auger hole capture coefficent [cm^6/s]	$1.0 \cdot 10^{-32}$	$1.0 \cdot 10^{-31}$
Absorption interpolation model		
Model	See subsection 3.3.3	

Table 3.8: Fixed defect parameters used for the GaAs/AlGaAs cells with defects.

Defect properties	
Variable	**Input**
Defect type	Neutral
Capture cross section electrons [cm^2]	$1.0 \cdot 10^{-13}$
Capture cross section holes [cm^2]	$1.0 \cdot 10^{-13}$
Energetic distribution	Single
Reference for defect energy level E_t	Above E_i
Energy level with respect to reference [eV]	0.000
N_t total [cm^{-3}]	$1.0 \cdot 10^{14}$

3.3.3 Absorption Coefficient

The absorption coefficient in SCAPS can either be defined by from a file or from a model. All absorption coefficient of cells with GaAs and/or AlGaAs in this thesis is defined from a file. For GaAs, this file is provided by SCAPS, and is shown as the black curve in Figure 3.3. In the figure does the rightmost vertical line indicate the bandgap energy of GaAs used in this thesis.

No absorption coefficient for AlGaAs is provided by SCAPS, and it was not found in literature either. Therefore was the absorption coefficient file for AlGaAs approximated by using the file for GaAs provided by SCAPS. In general, as both are relatively similar materials and both are direct semiconductors at the Al fraction of $x = 0.3$ used in this thesis, should this be an acceptable approximation if done correctly. This should be done by using a non-linear shift of the energy axis decreasing with increasing energy. However, due to a misunderstanding of the literature was the AlGaAs absorption coefficient was instead obtained by setting all values in the GaAs file below the AlGaAs bandgap to zero. The result of this is illustrated as the dashed red curve in Figure 3.3, where the leftmost line corresponds to the bandgap energy of AlGaAs.

Unfortunately, this error was identified at the end of the master thesis work. The result of this is that the calculated efficiencies of cells with AlGaAs increases slightly due to higher photon absorption. As this this effect is constant for all AlGaAs cells will it not affect the observed changes when other parameters are varied, and is thus mostly omitted from the discussions in chapter 4.
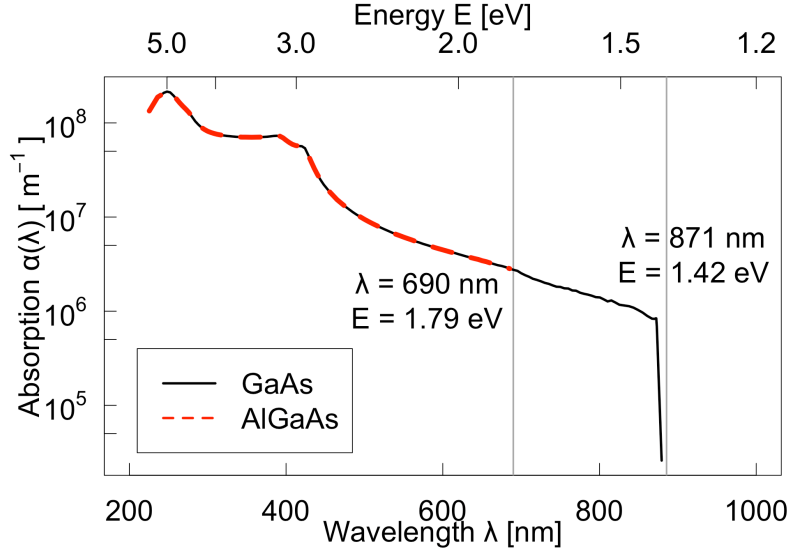

Figure 3.3: Absorption coefficient as a function of wavelength (or equivalently energy) for GaAs (black curve) and AlGaAs (dashed red curve). The rightmost line indicates the bandgap of AlGaAs, while the rightmost line indicates the bandgap of GaAs. The curve for GaAs is taken from Ref. [11].

3.4 Modified GaAs/AlGaAs Cells

The simulated GaAs*/AlGaAs cells consists of four layers: p-GaAs*/p-GaAs*/n-AlGaAs/n-AlGaAs, and they all have impurities. The asterisk on the GaAs* indicates that the electron affinity have been modified. This was done by calculating the CB offset in the *AlGaAs - Uni.* cell from the preceding section and adjusting the electron affinity using Anderon's rule and Eq.(2.6) so that the the CB offset disappeared. The modified value of the electron affinity of the GaAs is $\chi_{\text{GaAs, new}} = 3.74$ eV. The thicknesses of the layers have been varied while the entire cell thickness have been kept constant at 1000 nm. This is schematically illustrated in Figure 3.4.

3.4.1 Varied Parameters

Initially, four GaAs*/AlGaAs cells where the doping concentrations in layers 2 and 3 were varied with respect to the value kept constant for layers 1 and 4 (see Figure 3.4). These four cells are labelled *GaAs* - Uni.*, *GaAs* - HL*, *GaAs* - LH*, and *GaAs* - HH*, where *H* and *L* denotes a *higher* and *lower* doping concentration in layers 2 and 3. The constant doping concentrations were taken from the *AlGaAs - Uni.* cell from the preceding section, and the *higher* and *lower* values were set to be approximately twice as much and half as much, respectively, as this is done in Ref. [11]. The doping concentrations are summarized in Table 3.9.

For the *GaAs* - Uni.* and *GaAs* - HL* cells, the *transmission* parameter in SCAPS (which effectively scales the incident light power) was varied between 100% and 0% at 10 percentage points increments, however the last value was set to 1% instead of 0%. At each incident light power density value, the efficiency of the two cells were calculated.
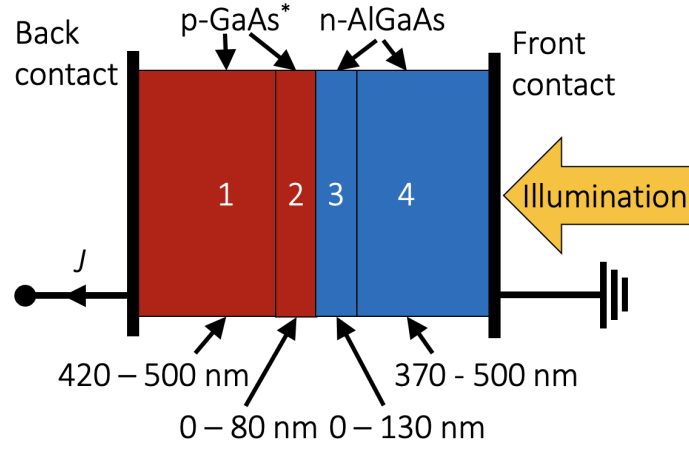
Figure 3.4: Schematic illustration of the structure of the modified GaAs*/AlGaAs cells. The total thickness is kept at 1000 nm, while the relative thicknesses of the layers are varied as indicated.

Table 3.9: Doping concentrations in the first four GaAs*/AlGaAs cells *GaAs* - Uni.*, *GaAs* - HL*, *GaAs* - LH*, and *GaAs* - HH*. The orange color in table represents values that changes from the previous row.

	1: p-GaAs* N_A [cm^{-3}]	2: p-GaAs* N_A [cm^{-3}]	3: n-AlGaAs N_D [cm^{-3}]	4: p-AlGaAs N_D [cm^{-3}]
GaAs - Uni.*	$9.0 \cdot 10^{17}$	$9.0 \cdot 10^{17}$	$9.0 \cdot 10^{17}$	$9.0 \cdot 10^{17}$
GaAs - HL*	$9.0 \cdot 10^{17}$	$2.0 \cdot 10^{18}$	$4.0 \cdot 10^{17}$	$9.0 \cdot 10^{17}$
GaAs - LH*	$9.0 \cdot 10^{17}$	$4.0 \cdot 10^{17}$	$2.0 \cdot 10^{18}$	$9.0 \cdot 10^{17}$
GaAs - HH*	$9.0 \cdot 10^{17}$	$2.0 \cdot 10^{18}$	$2.0 \cdot 10^{18}$	$9.0 \cdot 10^{17}$

Next, using the *GaAs* - Uni.* cell, the capture cross section (CCS) of electrons and holes where kept equal, i.e. $\sigma = \sigma^n = \sigma^p$, and varied between 10^{-8} cm^2 and 10^{-20} cm^2 with a factor 10 increment. For each value of the CCS was the defect density N_t varied between 10^8 cm^{-3} and 10^{20} cm^{-3}, also with a factor 10 increment. From these simulations, one new cell with $\sigma = 10^{-12}$ cm^2 and $N_t = 10^{16}$ cm^{-3} was constructed. This cell is labelled *GaAs* - LE* (LE = low efficiency).

Now using the *GaAs* - LE* cell, the variation of doping concentrations in layers 2 and 3 was then repeated. This resulted in three new cells, where the doping concentrations in layers 2 and 3 were higher and lower, lower and higher, and higher and higher. These are labelled *GaAs* - LE, HL*, *GaAs* - LE, LH*, and *GaAs* - LE, HH*, respectively, and their doping concentrations are summarized in Table 3.10.

Table 3.10: Doping concentrations in the LE cells with a modified value of the GaAs electron affinity *GaAs* - LE*, *GaAs* - LE, HL*, *GaAs* - LE, LH*, and *GaAs* - LE, HH*. The orange color in table represents values that changes from the previous row.

	1: p-GaAs* N_A [cm^{-3}]	2: p-GaAs* N_A [cm^{-3}]	3: n-AlGaAs N_D [cm^{-3}]	4: p-AlGaAs N_D [cm^{-3}]
GaAs - LE*	$9.0 \cdot 10^{17}$	$9.0 \cdot 10^{17}$	$9.0 \cdot 10^{17}$	$9.0 \cdot 10^{17}$
GaAs - LE, HL*	$9.0 \cdot 10^{17}$	$2.0 \cdot 10^{18}$	$4.0 \cdot 10^{17}$	$9.0 \cdot 10^{17}$
GaAs - LE, LH*	$9.0 \cdot 10^{17}$	$4.0 \cdot 10^{17}$	$2.0 \cdot 10^{18}$	$9.0 \cdot 10^{17}$
GaAs - LE, HH*	$9.0 \cdot 10^{17}$	$2.0 \cdot 10^{18}$	$2.0 \cdot 10^{18}$	$9.0 \cdot 10^{17}$

Finally, the relative thicknesses of the two layers of each material in the *GaAs* - LE, HL* cell was varied. The second GaAs* layer was varied between 0 nm and 80 nm, and the first GaAs* layer was thus varied between 500 nm and 420 nm to keep the total thickness of the GaAs* layers constant at 500 nm. The first AlGaAs layer was varied between 0 nm an 130 nm, and the second was varied between 500 nm and 380 nm, again to keep the total thickness constant at 500 nm.

3.4.2 Fixed Parameters

Table 3.11 provides the fixed material, recombination, and absorption parameters for the GaAs*/AlGaAs cells. Then, Table 3.12 provides the defect parameters used in the GaAs*/AlGaAs cells with impurities. All simulations except the ones where the transmission were varied were conducted at an incident light power of 1000 Wm^{-2} with 100% transmission.

Table 3.11: Fixed material parameters for the GaAs*/AlGaAs cells. All values except from the value of the electron affinity of GaAs are based on the values provided by *Ioffe Institute* [26]. Instead, this value is calculated as described in subsection 4.2.3, and it thus marked in orange.

Variable	p-GaAs*	n-Al$_{0.3}$Ga$_{0.7}$As
Material Parameters		
Bandgap [eV]	1.424	1.798
Electron affinity [eV]	3.740	3.740
Dielectric permitivity [relative]	12.900	12.050
CB effective density of states [cm^{-3}]	$4.7 \cdot 10^{17}$	$6.5 \cdot 10^{17}$
VB effective density of states [cm^{-3}]	$9.0 \cdot 10^{18}$	$1.1 \cdot 10^{19}$
Electron thermal velocity [cm/s]	$4.4 \cdot 10^{7}$	$3.8 \cdot 10^{7}$
Electron thermal velocity [cm/s]	$1.8 \cdot 10^{7}$	$1.7 \cdot 10^{7}$
Hole thermal velocity [cm/s]	$4.0 \cdot 10^{3}$	$2.3 \cdot 10^{3}$
Electron mobility [cm^2/Vs]	$2.0 \cdot 10^{2}$	$1.5 \cdot 10^{2}$
Recombination Model		
Radiative recombination coefficient [cm^3/s]	$7.2 \cdot 10^{-10}$	$1.8 \cdot 10^{-10}$
Auger electron capture coefficent [cm^6/s]	$1.0 \cdot 10^{-31}$	$1.0 \cdot 10^{-31}$
Auger hole capture coefficent [cm^6/s]	$1.0 \cdot 10^{-32}$	$1.0 \cdot 10^{-31}$
Absorption interpolation model		
Model	See subsection 3.3.3	

Table 3.12: Fixed defect parameters used for the GaAs*/AlGaAs cells.

Defect properties	
Variable	**Input**
Defect type	Neutral
Energetic distribution	Single
Reference for defect energy level E_t	Above E_i
Energy level with respect to reference [eV]	0.000

3.5 GaAs Homojunction Cells

The cells in this section only consist of GaAs. The four initial cells are buildt up of four layers: p-GaAs/p-GaAs/n-GaAs/n-GaAs, and they all have impurities. Their thicknesses are 480 nm, 20 nm, 40 nm, and 460 nm, respectively. This is schematically illustrated in Figure 3.5. The GaAs here does <u>not</u> use the modified value of the electron affinity from section 3.4.

Five additional GaAs homojunction cells were simulated, and the number of layers and the layer thicknesses in these cells are not shown in a figure but summarized in Table 3.13.
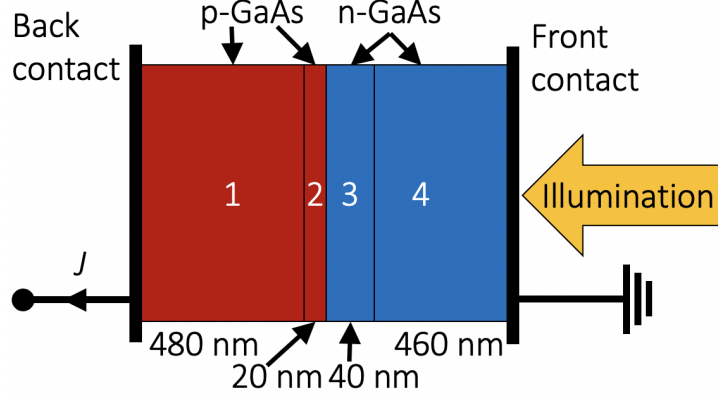

Figure 3.5: Schematic illustration of the structure of the GaAs homojunction cells.

3.5.1 Varied Parameters

Initially, four GaAs homojunction cells with different doping concentrations were simulated. These four cells are labelled *GaAs, HJ - Uni.*, *GaAs, HJ - HL*, *GaAs, HJ - LH*, and *GaAs, HJ - HH* (*HJ* denotes HomoJunction), and their doping concentrations are summarized in Table 3.13.

Table 3.13: Doping concentrations in the GaAs homojunction cells *GaAs, HJ - Uni.*, *GaAs, HJ - HL*, *GaAs, HJ - LH*, and *GaAs, HJ - HH*. The orange color in table represents values that changes from the previous row.

	1: p-GaAs N_A [cm^{-3}]	2: p-GaAs N_A [cm^{-3}]	3: n-GaAs N_D [cm^{-3}]	4: n-GaAs N_D [cm^{-3}]
GaAs, HJ - Uni.	$9.0 \cdot 10^{17}$	$9.0 \cdot 10^{17}$	$9.0 \cdot 10^{17}$	$9.0 \cdot 10^{17}$
GaAs, HJ - HL	$9.0 \cdot 10^{17}$	$2.0 \cdot 10^{18}$	$4.0 \cdot 10^{17}$	$9.0 \cdot 10^{17}$
GaAs, HJ - LH	$9.0 \cdot 10^{17}$	$4.0 \cdot 10^{17}$	$2.0 \cdot 10^{18}$	$9.0 \cdot 10^{17}$
GaAs, HJ - HH	$9.0 \cdot 10^{17}$	$2.0 \cdot 10^{18}$	$2.0 \cdot 10^{18}$	$9.0 \cdot 10^{17}$

Then, five new GaAs homojunctions where simulated where the doping concentration was kept constant at $9 \cdot 10^{17}$ cm^{-3} while the number of layers and the layer thicknesses were varied. The five cells are labelled *GaAs, HJ - 1*, *GaAs, HJ - 2*, *GaAs, HJ - 3*, *GaAs, HJ - 4*, and *GaAs, HJ - 5*. The *GaAs, HJ - 2* cells happens to be identical to the *GaAs, HJ - Uni.* cell, but they are kept separate to make the upcoming comparisons easier. All the cell layers and thicknesses of these cells are summarized in Table 3.14.

Table 3.14: Number of layers and the layer thicknesses in the *GaAs, HJ - 1*, *GaAs, HJ - 2*, *GaAs, HJ - 3*, *GaAs, HJ - 4*, and *GaAs, HJ - 5* cells.

Cell	Layer 1	Layer 2		
GaAs, HJ - 1	500 nm	500 nm		

Cell	Layer 1	Layer 2	Layer 3	Layer 4
GaAs, HJ - 2	250 nm	250 nm	250 nm	250 nm
GaAs, HJ - 3	480 nm	20 nm	40 nm	460 nm
GaAs, HJ - 4	20 nm	480 nm	460 nm	40 nm
GaAs, HJ - 5	495 nm	5 nm	5 nm	495 nm

3.5.2 Fixed Parameters

Table 3.15 provides the fixed material, recombination, and absorption parameters for the GaAs homojunction cells. Table 3.16 provides the defect parameters used in the GaAs homojunction cells with impurities.

Table 3.15: Fixed material parameters for all GaAs homojunction cells. The values are the same in the p- and n-layers, and are based on the values provided by *Ioffe Institute* [26]. The value of the electron affinity have been changed back to the value provided by *Ioffe Institute* from the value given in Table 3.11, and is thus marked in orange.

Variable	p/n-GaAs
Material Parameters	
Bandgap [eV]	1.424
Electron affinity [eV]	4.070
Dielectric permitivity [relative]	12.900
CB effective density of states [cm^{-3}]	$4.7 \cdot 10^{17}$
VB effective density of states [cm^{-3}]	$9.0 \cdot 10^{18}$
Electron thermal velocity [cm/s]	$4.4 \cdot 10^{7}$
Electron thermal velocity [cm/s]	$1.8 \cdot 10^{7}$
Hole thermal velocity [cm/s]	$4.0 \cdot 10^{3}$
Electron mobility [cm^2/Vs]	$2.0 \cdot 10^{2}$
Recombination Model	
Radiative recombination coefficient [cm^3/s]	$7.2 \cdot 10^{-10}$
Auger electron capture coeffcient [cm^6/s]	$1.0 \cdot 10^{-31}$
Auger hole capture coeffcient [cm^6/s]	$1.0 \cdot 10^{-32}$
Absorption interpolation model	
Model	See subsection 3.3.3

Table 3.16: Fixed defect parameters used for the GaAs homojunction cells.

Defect properties	
Variable	**Input**
Defect type	Neutral
Capture cross section electrons [cm^2]	$1.0 \cdot 10^{-12}$
Capture cross section holes [cm^2]	$1.0 \cdot 10^{-12}$
Energetic distribution	Single
Reference for defect energy level E_t	Above E_i
Energy level with respect to reference [eV]	0.000
N_t total [cm^{-3}]	$1.0 \cdot 10^{16}$

3.6 GaAs Homojunction IPV Cells

The cells in this section is build up of 1 to 2 p-GaAs layer(s), one i-GaAs layer, and 1 to 2 either i-GaAs or n-GaAs layer(s), and only the middle i-layer (layer 3) has impurities. Their thicknesses have all been varied, but the total thicknesses of layers 1 and 2 combined and 4 and 5 combined have been kept constant at 495 nm each. This is schematically illustrated in Figure 3.6, where the red color indicates p-type, the green color indicates i-type, the blue color indicates n-type, and a combination of green and blue indicates that the layer has been simulated both as an i-layer and a n-layer. As only the middle i-layer, i.e. layer 3, has impurities, is it also the only layer where the IPV effect can take place.
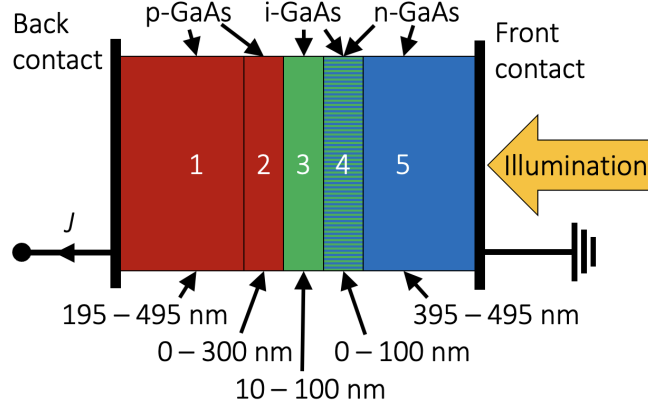

Figure 3.6: Schematic illustration of the layers in the GaAs IPV homojunction cells. The thicknesses of the two first and two last layers were kept constant at 495 nm each. The middle i-layer was varied between 10 and 100 nm. Thus, the total cell thickness varied between 1000 and 1090 nm.

3.6.1 Varied Parameters

Initially, two reference p-i-n cells were simulated, one without and with the IPV effect. These are labelled *GaAs, No IPV* and *GaAs, IPV*, respectively. The layer thicknesses in these cells were 495 nm, 10 nm, and 495 nm, and the doping concentrations were $N_A = N_D = 9 \cdot 10^{17}$ cm^{-3}.

Then, in the *GaAs, IPV* cell, the doping concentrations of the p- and n-layer were independently optimized (values between $6 \cdot 10^{16}$ cm^{-3} and $1 \cdot 10^{18}$ cm^{-3}). This was followed by an optimization of the i-layer thickness (values between 10 nm and 100 nm) were the total thickness of the cell was varied. The best performing cell after these optimizations is labelled *GaAs, IPV - pin*.

The n-layer in the *GaAs, IPV - pin* was then split into two layers. Initially, the layer in contact with the i-layer was 50 nm, while the other n-layer was 445 nm. The doping concentration of the narrow n-layer was then varied between 0 cm^{-3} and $1 \cdot 10^{18}$ cm^{-3} to find the optimum value. Then, the thickness of the same was varied between 0 nm and 200 nm, again to find the optimum value. This resulted in a cell labelled *GaAs, IPV - pinn*.

Next, the p-layer was split into two and a similar procedure as described above was conducted. At a layer thickness of 50 nm, the doping concentration was optimized (values between 0 cm^{-3} and $1 \cdot 10^{18}$ cm^{-3}), followed by an optimization of the thickness of the same layer (values between 50 nm and 300 nm). This resulted in a cell denoted *GaAs, IPV - ppinn*. All the main cell characteristics of the GaAs IPV homojunction cells are summarized in Table 3.17.

Table 3.17: Main characteristics of the IPV GaAs homojunction cells. See Figure 3.6 for schematic illustration of the layers.

Cell	Characteristics
GaAs, No IPV	No IPV effect.
GaAs, IPV	IPV effect enabled
GaAs, IPV - pin	Optimized doping concentration and i-layer thickness
GaAs, IPV - pinn	Optimized doping concentration and thickness of layer 4
GaAs, IPV - ppinn	Optimized doping concentration and thickness of layer 2

3.6.2 Fixed Parameters

Table 3.18 provides the fixed material, recombination, and absorption parameters for the GaAs homojunction IPV cells. Then, Table 3.19 provides the defect parameters used in the same cells.

Table 3.18: Fixed material parameters for all GaAs homojunction IPV cells. The values are the same in the p-, i- and n-layers, and are based on the values provided by *Ioffe Institute* [26].

Variable	p/i/n-GaAs
Material Parameters	
Bandgap [eV]	1.424
Electron affinity [eV]	4.070
Dielectric permitivity [relative]	12.900
CB effective density of states [cm^{-3}]	$4.7 \cdot 10^{17}$
VB effective density of states [cm^{-3}]	$9.0 \cdot 10^{18}$
Electron thermal velocity [cm/s]	$4.4 \cdot 10^{7}$
Electron thermal velocity [cm/s]	$1.8 \cdot 10^{7}$
Hole thermal velocity [cm/s]	$4.0 \cdot 10^{3}$
Electron mobility [cm^2/Vs]	$2.0 \cdot 10^{2}$
Recombination Model	
Radiative recombination coefficient [cm^3/s]	$7.2 \cdot 10^{-10}$
Auger electron capture coefficent [cm^6/s]	$1.0 \cdot 10^{-31}$
Auger hole capture coefficent [cm^6/s]	$1.0 \cdot 10^{-32}$
Absorption interpolation model	
Model	See subsection 3.3.3

Table 3.19: Fixed defect parameters used in the i-layer (layer 3) in the GaAs homojunction IPV cells. As the cells in this section (and the next two) allows for the IPV effect, the necessary parameters for the optical capture are included in this table and marked in orange here.

Defect properties	
Variable	**Input**
Defect type	Neutral
Capture cross section electrons [cm^2]	$1.0 \cdot 10^{-12}$
Capture cross section holes [cm^2]	$1.0 \cdot 10^{-12}$
Energetic distribution	Single
Reference for defect energy level E_t	Above E_i
Energy level with respect to reference [eV]	0.000
N_t total [cm^{-3}]	$1.0 \cdot 10^{16}$
Refractive index [1]	3
Effective mass of electrons [1]	$6.7 \cdot 10^{-2}$
Effective mass of holes [1]	$4.7 \cdot 10^{-1}$
Effective field ratio [1]	$2.0 \cdot 10^{0}$
Cut off energy [eV]	1.4

3.7 Modified p-GaAs/i-GaAs/n-AlGaAs IPV Cells

The cells in this section are built-up as those in the preceding section, except that layers 4 and 5 now is AlGaAs and that the electron affinity of GaAs have been modified. In addition is the middle i-layer thickness not varied, so the total cell thickness is kept constant at 1090 nm. This is schematically illustrated in Figure 3.6, where the red color indicates p-type, the green color indicates i-type, the blue color indicates n-type, and a combination of green and blue indicates that the layer has been simulated both as an i-layer and a n-layer. The asterisk in GaAs* layers indicates that their electron affinity have been modified. As only the middle i-layer, i.e. layer 3, has impurities, is it also the only layer where the IPV effect can take place.
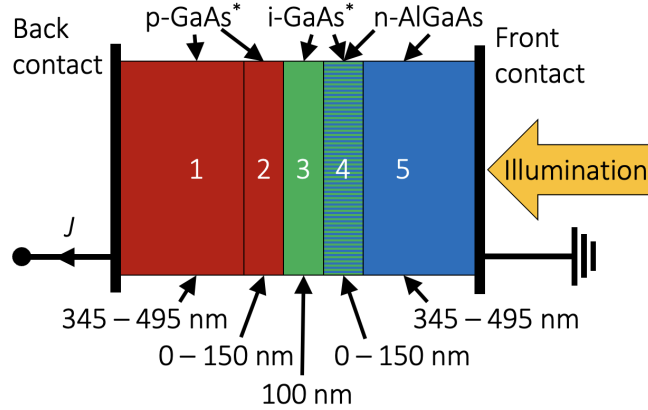

Figure 3.7: Schematic illustration of the layers in the p-GaAs*/i-GaAs*/n-AlGaAs IPV cells. The total thickness is kept at 1090 nm, while the relative thicknesses of the layers are varied as indicated.

3.7.1 Varied Parameters

Initially, a p-i-n cell with the IPV effect enabled and using $\chi = 4.07$ eV as the electron affinity in the GaAs layers was simulated. This cell is labelled *GaAs, IPV - CB*. Next, a identical cell except using $\chi = 3.75$ eV as electron affinity in the GaAs layers was simulated. This cell is labelled *GaAs*, IPV - pin*. Then, an identical cell to the *GaAs*, IPV - pin* except the IPV effect was disbled was simulated. This cell is labelled *GaAs*, No IPV*. The layer thicknesses in all these cells were 495 nm (p), 100 nm (i), and 495 nm (n), and the doping concentrations were $N_A = N_D = 9 \cdot 10^{17}$ cm^{-3} in all layers except the i-layer (which do not have doping).

The n-layer in the *AlGaAs*, IPV - pin* was then split into two layers. Initially, the layer in contact with the i-layer was 50 nm, while the other was 445 nm. The doping concentration of the narrow n-layer was then varied between 0 cm^{-3} and $1 \cdot 10^{18}$ cm^{-3} to find the optimum value. Then, the thickness of the same was varied between 0 nm and 200 nm, again to find the optimum value. This resulted in a cell labelled *GaAs*, IPV - pinn*.

Then, the p-layer was split into two a similar procedure was conducted. At a layer thickness of 50 nm, the doping concentration was optimized (values between $1 \cdot 10^{15}$ cm^{-3} and $1 \cdot 10^{18}$ cm^{-3}), followed by an optimization of the thickness of the same layer (values between 0 nm and 150 nm). This resulted in a cell labelled *GaAs*, IPV - ppinn*. All the main cell characteristics of the modified p-GaAs*/i-GaAs*/n-AlGaAs IPV cells are summarized in Table 3.17.

Table 3.20: Main characteristics of the modified p-GaAs*/i-GaAs*/n-AlGaAs IPV cells. See Figure 3.7 for schematic illustration of the layers.

Cell	Characteristics
GaAs, IPV - CB	With IPV effect and CB offset
GaAs*, IPV - pin	With IPV effect and without CB offset
GaAs*, No IPV	Without IPV effect and CB offset
GaAs*, IPV - pinn	Optimized doping concentration and thickness of layer 4
GaAs*, IPV - ppinn	Optimized doping concentration and thickness of layer 2

3.7.2 Fixed Parameters

Table 3.21 provides the fixed material, recombination, and absorption parameters for the modified p-GaAs*/i-GaAs*/n-AlGaAs IPV cells. Then, Table 3.22 provides the defect parameters used in the same cells.

Table 3.21: Fixed material parameters for all modified p-GaAs*/i-GaAs*/n-AlGaAs IPV cells. All values except from the value of the electron affinity of GaAs are based on the values provided by *Ioffe Institute* [26]. Instead, this value is calculated as described in subsection 4.6.1, and it thus marked in orange.

Variable	p-GaAs*	n-Al$_{0.3}$Ga$_{0.7}$As
Material Parameters		
Bandgap [eV]	1.424	1.798
Electron affinity [eV]	3.740	3.740
Dielectric permitivity [relative]	12.900	12.050
CB effective density of states [cm^{-3}]	$4.7 \cdot 10^{17}$	$6.5 \cdot 10^{17}$
VB effective density of states [cm^{-3}]	$9.0 \cdot 10^{18}$	$1.1 \cdot 10^{19}$
Electron thermal velocity [cm/s]	$4.4 \cdot 10^{7}$	$3.8 \cdot 10^{7}$
Electron thermal velocity [cm/s]	$1.8 \cdot 10^{7}$	$1.7 \cdot 10^{7}$
Hole thermal velocity [cm/s]	$4.0 \cdot 10^{3}$	$2.3 \cdot 10^{3}$
Electron mobility [cm^2/Vs]	$2.0 \cdot 10^{2}$	$1.5 \cdot 10^{2}$
Recombination Model		
Radiative recombination coefficient [cm^3/s]	$7.2 \cdot 10^{-10}$	$1.8 \cdot 10^{-10}$
Auger electron capture coefficent [cm^6/s]	$1.0 \cdot 10^{-31}$	$1.0 \cdot 10^{-31}$
Auger hole capture coefficent [cm^6/s]	$1.0 \cdot 10^{-32}$	$1.0 \cdot 10^{-31}$
Absorption interpolation model		
Model	See subsection 3.3.3	

Table 3.22: Fixed defect parameters used in the i-layer (layer 3) in the modified p-GaAs*/i-GaAs*/n-AlGaAs IPV cells.

Defect properties	
Variable	**Input**
Defect type	Neutral
Capture cross section electrons [cm^2]	$1.0 \cdot 10^{-12}$
Capture cross section holes [cm^2]	$1.0 \cdot 10^{-12}$
Energetic distribution	Single
Reference for defect energy level E_t	Above E_i
Energy level with respect to reference [eV]	0.000
N_t total [cm^{-3}]	$1.0 \cdot 10^{16}$
Refractive index [1]	3
Effective mass of electrons [1]	$6.7 \cdot 10^{-2}$
Effective mass of holes [1]	$4.7 \cdot 10^{-1}$
Effective field ratio [1]	$2.0 \cdot 10^{0}$
Cut off energy [eV]	1.4

3.8 Modified p-AlGaAs/i-GaAs/n-AlGaAs IPV Cells

The cells in this section are again built-up as those in the preceding section, except that layers 1 to 2 now also are AlGaAs. The electron affinity of GaAs is here set back to its correct value, while the electron affinity of the two AlGaAs layers are modified. The middle i-layer thickness not varied, so the total cell thickness is kept constant at 1090 nm. This is schematically illustrated in Figure 3.8, where the red color indicates p-type, the green color indicates i-type, the blue color indicates n-type, and a combination of green and blue indicates that the layer has been simulated both as an i-layer and a n-layer. The asterisk in AlGaAs* layers indicates that their electron affinity have been modified. As only the middle i-layer, i.e. layer 3, has impurities, is it also the only layer where the IPV effect can take place.
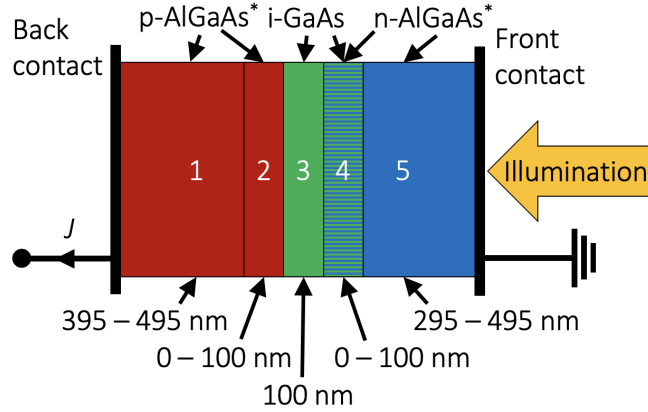

Figure 3.8: Schematic illustration of the layers in the p-AlGaAs*/i-GaAs/n-AlGaAs* IPV cells. The total thickness is kept at 1090 nm, while the relative thicknesses of the layers are varied as indicated.

3.8.1 Varied Parameters

Initially, a p-i-n cell without the IPV effect enabled and using $\chi = 3.74$ eV as the electron affinity in the AlGaAs layers was simulated. This cell is labelled *AlGaAs, No IPV - Barrier*. Then, a identical cell except using 3.69 eV as electron affinity in the p-AlGaAs layer and 4.07 eV in the n-AlGaAs was simulated. This cell is labelled *AlGaAs*, No IPV*. Then, an identical cell to the *GaAs*, No IPV* except the IPV effect was enabled was simulated. This cell is labelled *AlGaAs*, IPV - pin*. The layer thicknesses in all these cells were 495 nm (p), 100 nm (i), and 495 nm (n), and the doping concentrations were $N_A = N_D = 9 \cdot 10^{17}$ cm^{-3} in all layers except the i-layer (which do not have doping).

The n-layer in the *AlGaAs*, IPV - pin* was then split into two layers. Initially, the layer in contact with the i-layer was 50 nm, while the other was 445 nm. The doping concentration of the narrow n-layer was then varied between 0 cm^{-3} and $1 \cdot 10^{18}$ cm^{-3} to find the optimum value. Then, the thickness of the same was varied between 0 nm and 150 nm, again to find the optimum value. This resulted in a cell labelled *AlGaAs, IPV* - pinn*.

Then, the p-layer was split into two and a similar procedure as described above was conducted. At a layer thickness of 50 nm, the doping concentration was optimized (values between $1 \cdot 10^{15}$ cm^{-3} and $1 \cdot 10^{18}$ cm^{-3}), followed by an optimization of the thickness of the same layer (values between 0 nm and 100 nm). This resulted in a cell labelled *AlGaAs*, IPV - ppinn*. All the main cell characteristics of the modified p-AlGaAs*/i-GaAs/n-AlGaAs* IPV cells are summarized in Table 3.23.

Table 3.23: Main characteristics of the modified p-AlGaAs*/i-GaAs/n-AlGaAs* IPV cells. See Figure 3.8 for schematic illustration of the layers.

Cell	Characteristics
AlGaAs, IPV - Barrier	Without IPV effect and with band offsets
AlGaAs*, No IPV	Without IPV effect and band offsets
AlGaAs*, IPV - pin	With IPV effect and without CB offset
AlGaAs*, IPV - pinn	Optimized doping concentration and thickness of layer 4
AlGaAs*, IPV - ppinn	Optimized doping concentration and thickness of layer 2

3.8.2 Fixed Parameters

Table 3.24 on the subsequent page provides the fixed material, recombination, and absorption parameters for modified p-AlGaAs*/i-GaAs/n-AlGaAs* IPV cells. Then, Table 3.25 provides the defect parameters used in the same cells.

Table 3.24: Fixed material parameters for all modified p-AlGaAs*/i-GaAs/n-AlGaAs* IPV cells. All values except from the values of the electron affinities of p- and n-AlGaAs are based on the values provided by *Ioffe Institute* [26]. Instead, they are calculated as described in subsection 4.7.1, and are thus marked in orange. In addition, since the electron affinity of GaAs have been changed back to the value provided by *Ioffe Institute* from the value given in Table 3.21, it is also marked in orange.

Variable	i-GaAs	n/p-Al$_{0.3}$Ga$_{0.7}$As*
Material Parameters		
Bandgap [eV]	1.424	1.798
Electron affinity, p-type [eV]	*NA*	3.690
Electron affinity, i-type [eV]	3.740	*NA*
Electron affinity, n-type [eV]	*NA*	4.070
Dielectric permitivity [relative]	12.900	12.050
CB effective density of states [cm^{-3}]	$4.7 \cdot 10^{17}$	$6.5 \cdot 10^{17}$
VB effective density of states [cm^{-3}]	$9.0 \cdot 10^{18}$	$1.1 \cdot 10^{19}$
Electron thermal velocity [cm/s]	$4.4 \cdot 10^{7}$	$3.8 \cdot 10^{7}$
Electron thermal velocity [cm/s]	$1.8 \cdot 10^{7}$	$1.7 \cdot 10^{7}$
Hole thermal velocity [cm/s]	$4.0 \cdot 10^{3}$	$2.3 \cdot 10^{3}$
Electron mobility [cm^2/Vs]	$2.0 \cdot 10^{2}$	$1.5 \cdot 10^{2}$
Recombination Model		
Radiative recombination coefficient [cm^3/s]	$7.2 \cdot 10^{-10}$	$1.8 \cdot 10^{-10}$
Auger electron capture coefficent [cm^6/s]	$1.0 \cdot 10^{-31}$	$1.0 \cdot 10^{-31}$
Auger hole capture coefficent [cm^6/s]	$1.0 \cdot 10^{-32}$	$1.0 \cdot 10^{-31}$
Absorption interpolation model		
Model	See subsection 3.3.3	

Table 3.25: Fixed defect parameters used in the i-layer (layer 3) in the modified p-AlGaAs*/i-GaAs/n-AlGaAs* IPV cells.

Defect properties	
Variable	**Input**
Defect type	Neutral
Capture cross section electrons [cm^2]	$1.0 \cdot 10^{-12}$
Capture cross section holes [cm^2]	$1.0 \cdot 10^{-12}$
Energetic distribution	Single
Reference for defect energy level E_t	Above E_i
Energy level with respect to reference [eV]	0.000
N_t total [cm^{-3}]	$1.0 \cdot 10^{16}$
Refractive index [1]	3
Effective mass of electrons [1]	$6.7 \cdot 10^{-2}$
Effective mass of holes [1]	$4.7 \cdot 10^{-1}$
Effective field ratio [1]	$2.0 \cdot 10^{0}$
Cut off energy [eV]	1.4

Chapter 4

Results and Discussion

This chapter provides all simulation results and the subsequent discussion of the results. Additionally, each section begins with the motivation behind the conducted simulations. The list below presents the sets of simulated cells and their respective section similar to the one given in chapter 3.

- Initially, section 4.1 is a replication of the GaInAsP/InP cells by Santhanam and Fan in Ref. [11]. These cells consist of five layers and there are impurities in all of them.
- Next, section 4.2 applies the design principle to p-GaAs/n-AlGaAs cells. These cells consist of four layers and there are impurities in all of them.
- In section 4.3, the CB offset present in the previous cells is removed to make modified p-GaAs*/n-AlGaAs cells, and the design principle is then applied to these cells. These cells also consist of four layers and there are impurities in all of them.
- In section 4.4, the design principle is applied to GaAs homojunction cells. Again does these cells consist of four layers and there are impurities in all of them.
- Then, in section 4.5, are the IPV cells introduced. Here, the design principle is applied to GaAs homojunction IPV cells. The cells in this section consists of five layers where only the middle layer has impurities.
- Next, section 4.6 repeats the simulations in the previous section but using modified CB offset-free p-GaAs*/i-GaAs*/n-AlGaAs IPV cells. These cells also consists of five layers where only the middle layer has impurities.
- Finally, in section 4.7 are the the the simulations in the previous section repeated, but using modified band offset-free p-AlGaAs*/i-GaAs/n-AlGaAs* IPV cells. Again, these cells also consists of five layers where only the middle layer has impurities.

In order to avoid confusion, a notice on the SRH recombination is given here. In the first four sections, the IPV effect is disabled and impurities causing SRH recombination are present in all layers (except a few impurity free cells). In general the cells in these four sections benefit from a lower SRH recombination rate. In the last three sections is the IPV effect enabled in the middle i-layers of the cell, and no other layers have impurities. In general these cells benefit from a higher SRH recombination rate because SCAPS calculates this as the net generation to recombination via the impurities.

4.1 GaInAsP/InP Cells

The cells in this section consists of p-InP/p-GaInAsP/p-GaInAsP/n-InP/n-InP cells as shown in Figure 3.1, but for convenience are the names shortened to GaInAsP/InP. They are, to best possible extent, a replication of the simulated PV cells by Santhanam and Fan [11]. This means that their design principle, i.e. a increased doping concentration in the p-layer and a decreased doping concentration in the n-layer around the p-n interface, is applied. They did this using the simulation program SimWindows 1.5.0 [27]. The aim of the simulations in this section is to replicate their results but using SCAPS [12]. This is done by simulation one reference cell without impurities, the *GaInAsP/InP - Ref.* cell, one cell with impurities and with homogeneous doping concentration, the *GaInAsP/InP - Hom.* cell, and one cell with impurities and with inhomogeneous doping concentration, the *GaInAsP/InP - Inhom.* cell.

Results

Performance Parameters and IV-curves

The efficiency η, the short-circuit current density J_{SC}, the open-circuit voltage V_{OC}, and the fill-factor FF (from hereon collectively denoted the performance parameters) for the *GaInAsP/InP - Ref.*, *GaInAsP/InP - Hom.*, and *GaInAsP/InP - Inhom.* cells are summarized in Table 4.1. The results showed that the impurity free cell *GaInAsP/InP - Ref.* had the highest efficiency (28.99%), the inhomogeneously doped cell *GaInAsP/InP - Inhom.* had the second highest efficiency (28.79%), and the homogeneously cell *GaInAsP/InP - Hom.* had the lowest efficiency (28.52%). The increase in efficiency due to the inhomogeneous doping concentration was thus 0.94% or 0.27 percentage points.

The IV-curves of the three GaInAsP/InP cells are presented in Figure 4.1. As can be seen in the figure, the three lines are hard to separate.

Table 4.1: Performance parameters for the GaInAsP/InP cells. η is the efficiency, J_{SC} is the short-circuit current density, V_{OC} is the open-circuit voltage, and FF is the fill-factor.

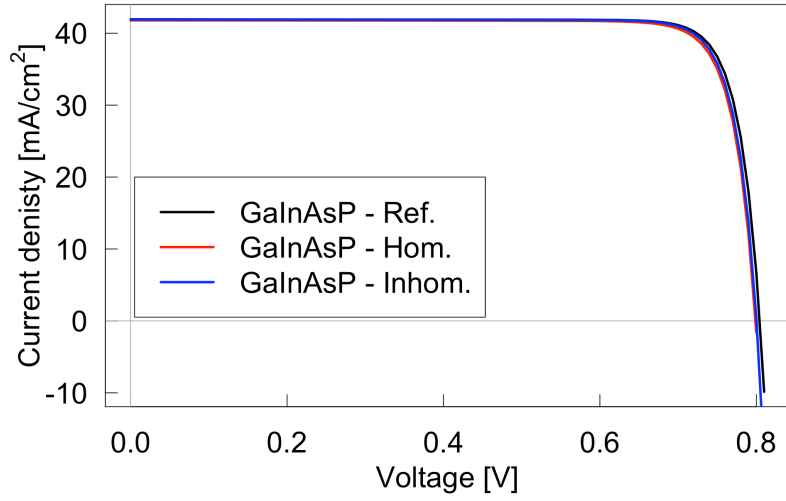|	η [%]	J_{SC} [mA/cm^2]	V_{OC} [V]	FF [%]
GaInAsP/InP - Ref.	28.99	41.93	0.80	85.96
GaInAsP/InP - Hom.	28.52	41.79	0.80	85.41
GaInAsP/InP - Inhom.	28.79	41.90	0.80	85.87

Figure 4.1: IV-curves of the *GaInAsP/InP - Ref.*, *GaInAsP/InP - Hom.*, and *GaInAsP/InP - Inhom.* cells.

Energy Band Diagrams

The energy band diagrams at $V = V_{\mathrm{OC}}$ for the *GaInAsP/InP - Hom.* and the *GaInAsP/InP - Inhom.* cells showing the CB edge E_{C}, the VB edge E_{V}, the quasi-Fermi level for electrons E_{Fn}, and the quasi-Fermi level for holes E_{Fp} are given in Figure 4.2a and Figure 4.2b, respectively. The energy band diagram for the *GaInAsP/InP - Ref.* cell is not presented as the interesting aspect of these figures is how the bands changes when the doping is changed.

(a) *GaInAsP/InP - Hom.*
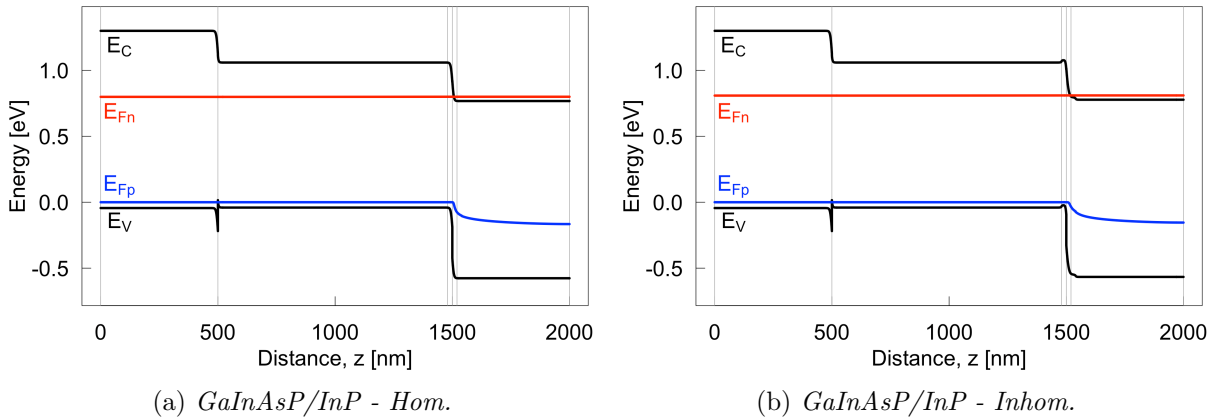
(b) *GaInAsP/InP - Inhom.*

Figure 4.2: Energy band diagrams at $V = V_{\mathrm{OC}}$ for (a) the *GaInAsP/InP - Hom.* cell and (b) the *GaInAsP/InP - Inhom.* cell. E_{C} is the CB edge, E_{V} is the VB edge, E_{Fn} is the quasi-Fermi level for electrons, and E_{Fp} is the quasi-Fermi level for holes. The vertical lines indicates the interfaces between the layers.
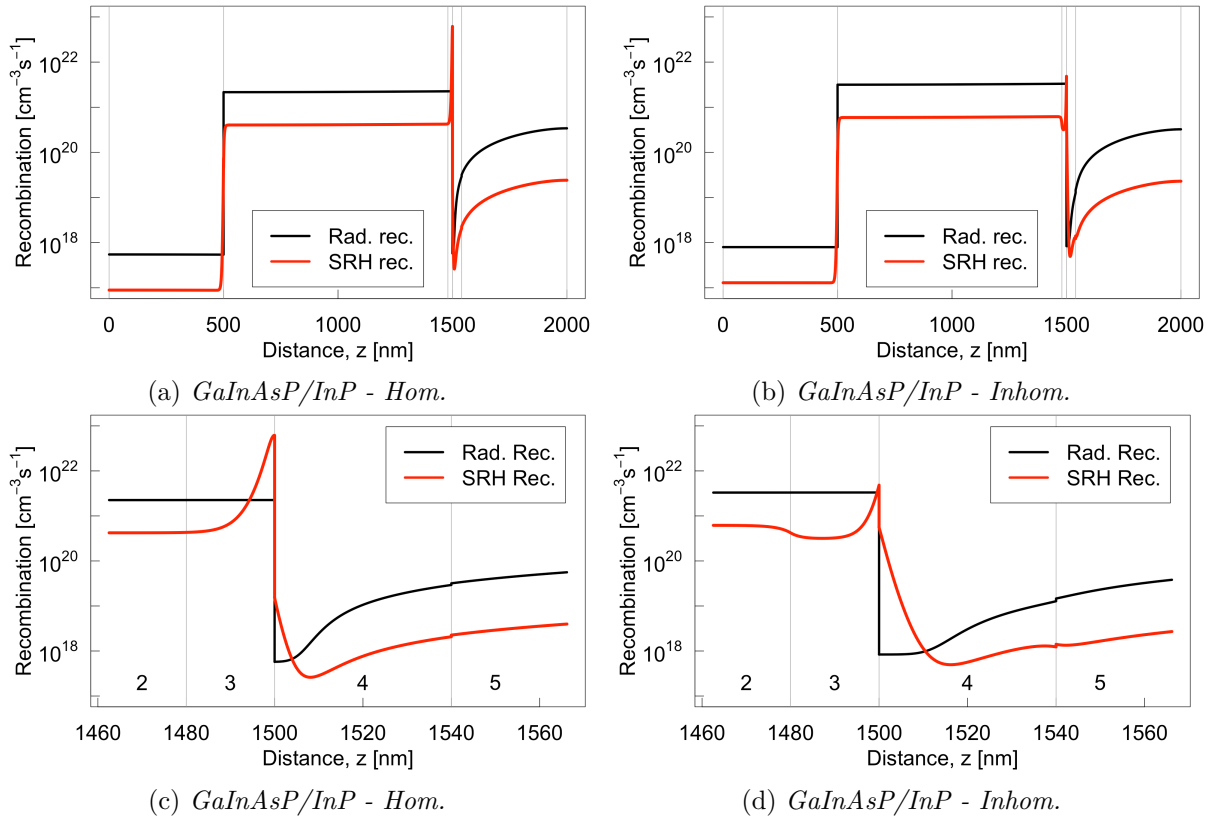
Recombination Rates

The radiative and SRH recombination rates at $V = V_{\text{OC}}$ for the *GaInAsP/InP - Hom.* and the *GaInAsP/InP - Inhom.* cells are shown in Figure 4.3a and Figure 4.3b, respectively. The peak of the SRH recombination rate at $z = 1500$ nm (z is from hereon the variable describing the position in the cells), i.e. at the interface between layers 3 and 4, drops with a factor 12.7 from $6.16 \cdot 10^{22}$ cm^{-3}s^{-1} to $4.84 \cdot 10^{21}$ cm^{-3}s^{-1} between the uniformly doped cell and the cell with inhomogeneous doping. As the SRH recombination rate for the *GaInAsP/InP - Ref.* cell is constant zero, are the plots for this cell omitted also here.

In order to better observe the change in recombination rates in the layers where the doping concentration was changed, Figure 4.3c and Figure 4.3d shows the recombination rates from $z = 1460$ nm to $z = 1560$ nm in the *GaInAsP/InP - Hom.* and *GaInAsP/InP - Inhom.* cells, respectively.

(a) *GaInAsP/InP - Hom.*   (b) *GaInAsP/InP - Inhom.*

(c) *GaInAsP/InP - Hom.*   (d) *GaInAsP/InP - Inhom.*

Figure 4.3: The radiative and SRH recombination rates at $V = V_{\text{OC}}$ for the *GaInAsP/InP - Hom.* and *GaInAsP/InP - Inhom.* cells. (a) and (b) shows the the entire cells, while (c) and (d) only shows from $z = 1460$ nm to $z = 1560$ nm. The vertical lines indicates the interfaces between the layers. The numbers 1 to 4 in (c) and (d) indicates the layers in the cells.

Discussion

In general, the relative performance of the three cells was as expected. The impurity free cell (*GaInAsP/InP - Ref.*) had the highest efficiency at 28.99%. This is simply because this cell does not have any recombination centers in the bandgap and thus no SRH recombination, a loss mechanism that reduces the efficiency. Compared to this cell, the cell with the inhomogeneous doping concentration (*GaInAsP/InP - Inhom.*) had a slightly lower drop in efficiency than the cell with the homogeneous doping concentration (*GaInAsP/InP - Hom.*). This means that an inhomogeneous doping profile gives a higher performance, a result consistent with the findings by Santhanam and Fan [11]. It also demonstrates that SCAPS is capable of simulating the effect, which was the aim of the simulations in this section.

To understand why the inhomogeneous doping concentration increases the efficiency one first needs to observe the canges in the band diagrams between the *GaInAsP/InP - Hom.* and *GaInAsP/InP - Inhom.* cells in Figure 4.2a and Figure 4.2b, respectively. As can be seen from these figures, the inhomogeneous doping concentration raises E_C on both sides of the p-n interface at around $z = 1500$ nm. This effectively moves the depletion region towards the wider bandgap material InP. The peak value of the SRH recombination rate scales with the intrinsic carrier concentration, a quantity that is smaller in InP than GaInAsP. Therefore, as is most easily seen in the recombination rates in Figure 4.3c and Figure 4.3d for the *GaInAsP/InP - Inhom.* and *GaInAsP/InP - Hom.* cells, respectively, does the peak value drops for the inhomogeneously doped cell. This reduces the total the total SRH recombination. By summing up all SRH recombination in Figure 4.3a and Figure 4.3b, one can find out that the total SRH recombination for the *GaInAsP/InP - Hom.* cell is $1.06 \cdot 10^{24}$ cm^{-3}s^{-1} and $1.41 \cdot 10^{23}$ cm^{-3}s^{-1} for the *GaInAsP/InP - Inhom.* cell. This result, together with the efficiencies of the cells, are summarized in Table 4.2. This reduced total recombination is the reason why the efficiency increases.

Table 4.2: Total SRH recombination at $V = V_{OC}$ and the efficiency for the *GaInAsP/InP - Hom.* and *GaInAsP/InP - Inhom.* cells.

Cell	*GaInAsP/InP - Hom.*	*GaInAsP/InP - Inhom.*
Total SRH recombination	$1.06 \cdot 10^{24}$ cm^{-3}s^{-1}	$1.41 \cdot 10^{23}$ cm^{-3}s^{-1}
Efficiency	28.52%	28.70%

The difference in efficiency between the *GaInAsP/InP - Inhom.* and *GaInAsP/InP - Hom.* cells is 0.95% or 0.27 percentage points. This performance increase is marginal, which also can be seen from the almost identical IV-curves in Figure 4.1. Even though higher efficiencies are always desired, one could think that such a low increase in almost negligible. However, as stated by Santhanam and Fan, their design principle only have a *significant* impact on lower quality cells, especially on cells with lower voltages. As can be seen by the high values of all the performance parameters in Table 4.1, none of the simulated cells here are of low quality. It is thus not surprising that the observed increase in the efficiency when their design principle was applied is low.

In addition to lower quality cells, the design principle is also less effective on cells where the SRH recombination not is the dominant loss mechanism. Such cells are characterized by having carriers with longer SRH lifetimes, i.e. the average time it takes for a minority carrier to recombine through the SRH mechanism. In their paper, they compared the effect the design principle on a cell with SRH lifetime of $\tau_{SRH} = 10$ ns and a cell with $\tau_{SRH} = 10$ ps (they used the same value for electrons and holes, i.e. $\tau_{SRH} = \tau_n = \tau_p$). Their results showed that the cell with the low lifetime (10 ps) had a 25% improvement in total power and efficiency due to

the design principle, while the cell with the high lifetime (10 ns) only improved by 1%. These results are summarized in Table 4.3. For the *GaInAsP/InP - Inhom.* cell simulated in this thesis, SCAPS calculated the lifetimes of the electrons and holes in the different layers. The values are listed in Table 4.3, and they are in general in the same order of magnitude as the high-lifetime cells by by Santhanam and Fan. This means that the 0.95% efficiency increase observed in the simulations conducted here when the design principle was applied corresponds well with the results by Santhanam and Fan.

Table 4.3: The SRH lifetimes and the efficiency increase due to the design principle by Santhanam and Fan in Ref. [11] for their high-lifetime cell, their low-lifetime cell, and the *GaInAsP/InP - Inhom.* cell from this thesis. The lifetime for Santhanam and Fan's cells are the same in all layers and for electrons and holes, while for the *GaInAsP/InP - Inhom.* cell the values varies. These values are calculated by SCAPS from the input values (Table 3.4 and Table 3.5).

	Material	τ_n	τ_p	Efficiency Increase
Higher lifetime cell	*NA*	10 ns	10 ns	1%
Lower lifetime cell	*NA*	10 ps	10 ps	25%
GaInAsP/InP - Inhom.	p-GaInAsP	22 ns	56 ns	0.95%
	n-InP	26 ns	59 ns	

There is one dominant problem with the simulations presented in this section, and it is the biggest hindrance for continuing working with GaInAsP/InP cells. This problem is the lack of reliable material parameters for this cell. As can be seen in Table 3.5, no source for the defect parameters were found in the paper nor in any other source. In addition, several of the material parameters, the recombination model, and the absorption interpolation model listed in Table 3.4 are without a source in Ref. [11]. This uncertainty in parameters can cause erroneous results, e.g. having the quasi-Fermi level for electrons exceed the CB edges such as in Figure 4.2a and Figure 4.2b. Therefore, a natural next step is to continue investigating the design principle in materials where material parameters are more readily available in literature. Santhanam and Fan states that, among others, that their principle is applicable to group III-V semiconductors. Two such materials are Gallium arsenide (GaAs) and Aluminium gallium arsenide (AlGaAs), and they are the chosen ones for the subsequent simulations in this work as they are well known, have reliable material parameters is available, they form a heterojunction, and a previous master student at NTNU, Tore Bysting, simulated GaAs cells using SCAPS in his master thesis [18].

4.2 GaAs/AlGaAs Cells

The aim of this section is to recreate the effect of the design principle presented by Santhanam and Fan [11] but using a p-GaAs/n-$Al_{0.3}Ga_{0.7}As$ heterojuntion. As only $Al_{0.3}Ga_{0.7}As$ is used in these simulations, the fraction of aluminium and gallium is from hereon omitted. The results from these cells and the subsequent discussion is divided into three parts: Impurities (subsection 4.2.1), Inhomogeneous Doping Concentration (subsection 4.2.2), and Varying Doping Concentrations (subsection 4.2.3).

4.2.1 Impurities

Two cells were simulated to verify that the found material parameters resulted in realistic performing cells. This was done by simulating one p-GaAs/n-AlGaAs impurity free cell labelled the *AlGaAs - Imp. free* cell, and one p-GaAs/n-AlGaAs cell with impurities labelled the *AlGaAs - Imp.* cell.

Results

Performance Parameters and IV-curves

The performance parameters for the *AlGaAs - Imp. free* and *AlGaAs - Imp.* cells are summarized in Table 4.4. As can be seen in the table, the efficiency dropped from 31.31% to 27.31% when the impurities were introduced.

The IV-curves for the *AlGaAs - Imp. free* and *GaAs - Imp.* cells are given in Figure 4.4. As can be seen from the figure, does the impurity free cell perform best.

Table 4.4: Performance parameters for the *AlGaAs - Imp. free* and *AlGaAs - Imp.* cells.

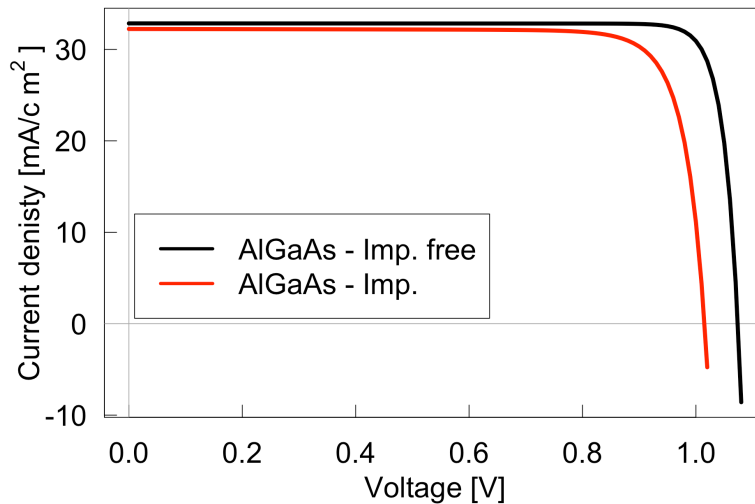|	η [%]	J_{SC} [mA/cm^2]	V_{OC} [V]	FF [%]
AlGaAs - Imp. free	31.31	32.85	1.07	88.75
AlGaAs - Imp.	27.31	32.24	1.02	83.44

Figure 4.4: IV-curves of the *AlGaAs - Imp. free* and *AlGaAs - Imp.* cells.

Energy Band Diagram and Recombination Rates

The energy band diagram and the radiative and SRH recombination rates at $V = V_{\text{OC}}$ for the *AlGaAs - Imp.* cell are given in Figure 4.5a and Figure 4.5b, respectively. Only the graphs for the cell with impurities are presented as this is the one that is relevant for the further simulations.
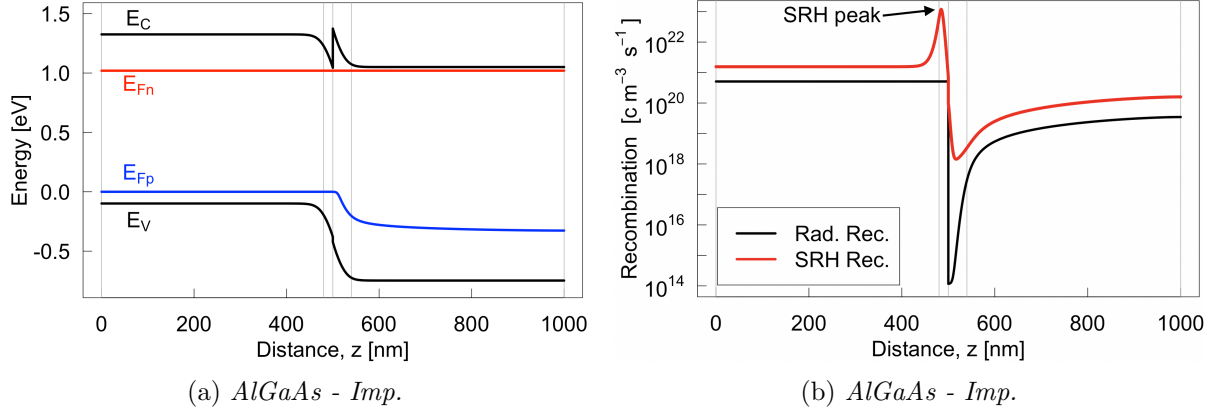

(a) *AlGaAs - Imp.*   (b) *AlGaAs - Imp.*

Figure 4.5: The energy band diagram and the radiative and SRH recombination rates at $V = V_{\text{OC}}$ for the *AlGaAs - Imp.* cell. The position of the peak value of the SRH recombination is indicated in (b). The vertical lines indicates the interfaces between the layers.

Discussion

As expected and in accordance with the results from the GaInAsP/InP cells in section 4.1, the impurity free cell (*AlGaAs - Imp. free*) performs better than the cell with impurities (*AlGaAs - Imp.*). Again is this because the impurities introduces the possibility for SRH recombination which reduces the cell efficiency. The energy band diagram for the *AlGaAs - Imp.* (Figure 4.5a) looks as expected with the characteristic CB offset ΔE_{C} for GaAs/AlGaAs p-n junctions [28]. In contrast to the quasi-Fermi level for electrons in the GaInAsP/InP cells, is E_{Fn} below the CB edge for the whole cell here, due to more appropriate doping concentrations. The peak of the SRH recombination is found in the middle of the depletion region at $z = 500$ nm (indicated in Figure 4.5b), and reducing this peak is the aim of the following simulations.

The efficiency of the *AlGaAs - Imp.* cell is very high at 27.31%. No simulations of similar cells could be found, but the calculated efficiency for both cells are not far off from similar cells such as Devendra *et. al.* [29], Green *et. al.* [30], and Bysting [18]. It is higher than what is currently achievable for real GaAs/AlGaAs cells [30], but importantly lower than the SQ limit [6]. This can be explained by the fact that the material parameters used are within a realistic range, but the simulating program works under optimal conditions omitting real-life efficiency reducing effects. In addition does high absorption coefficient of AlGaAs used in this work slightly increase the efficiency of the cells. Therefore, the results here are regarded as good enough, meaning they are realistic and can be used to investigate the design principle by Santhanam and Fan [11]. Apart from contribution to the verification of the material parameters is the impurity free cell *AlGaAs - Imp. free* not very interesting in the context here and will not be discussed further. This is because the aim is to reduce the SRH recombination which this cell does not have.

This section showed that the simulations resulted in acceptable GaAs/AlGaAs solar cells. Therefore, the next step is to simulate new cells where the doping concentrations around the depletion region is adjusted according to the design principle by Santhanam and Fan [11].

4.2.2 Inhomogeneous Doping Concentration

The aim of this section is apply the the design principle by Santhanam and Fan on the GaAs/AlGaAs cells, i.e. increasing the doping concentration in the p-layer and decreasing the doping concentration in n-layer near the p-n interface. The values of the doping concentrations and the thicknesses of the layers where the doping concentrations are varied, are the same as in the work by Santhanam and Fan. In addition, the reverse of the principle, i.e. a low doping concentration in the p-layer and a high doping concentration in the n-layer, is also investigated to observe the effect this has. Two cells were simulated, namely *AlGaAs - HL* and *AlGaAs - LH*. *H* and *L* denotes *high* and *low* doping concentration in layer 2 and then layer 3 compared to the doping concentration in layers 1 and 4 (see Figure 3.2 for a schematic illustration of the layers in the GaAs/AlGaAs cells). To remind the reader of the layer thicknesses and their doping concentrations are the values repeated in Table 4.5.

Table 4.5: Doping concentrations in the *AlGaAs - Imp.*, *AlGaAs - HL*, and *AlGaAs - LH* cells. The orange color represents values that changes from the previous row.

Cell	p-GaAs (480 nm) N_A [cm^{-3}]	p-GaAs (20 nm) N_A [cm^{-3}]	n-AlGaAs (40 nm) N_D [cm^{-3}]	n-AlGaAs (460 nm) N_D [cm^{-3}]
AlGaAs - Imp.	$2.0 \cdot 10^{17}$	$2.0 \cdot 10^{17}$	$2.0 \cdot 10^{17}$	$2.0 \cdot 10^{17}$
AlGaAs - HL	$2.0 \cdot 10^{17}$	$4.0 \cdot 10^{17}$	$1.0 \cdot 10^{17}$	$2.0 \cdot 10^{17}$
AlGaAs - LH	$2.0 \cdot 10^{17}$	$1.0 \cdot 10^{17}$	$4.0 \cdot 10^{17}$	$2.0 \cdot 10^{17}$

Results

Performance Parameters and IV-curves

The performance parameters for the *AlGaAs - HL* and *AlGaAs - LH* cells are summarized in Table 4.6. The parameters for the *AlGaAs - Imp.* cell from the previous section are also included for comparison. Compared to the *AlGaAs - Imp.* cell, the *AlGaAs - HL* cell showed a substantial efficiency decrease at 16.92% or 4.62 percentage points, while the *AlGaAs - LH* cell only showed a slightly efficiency decrease at 0.37% or 0.10 percentage points.

Table 4.6: Performance parameters for the *AlGaAs - Imp.*, *AlGaAs - HL*, and *AlGaAs - LH* cells.

	η [%]	J_{SC} [mA/cm^2]	V_{OC} [V]	FF [%]
AlGaAs - Imp.	27.31	32.24	1.02	83.44
AlGaAs - HL	22.69	32.27	1.05	67.11
AlGaAs - LH	27.21	32.11	1.01	83.58

51

The IV-curves for the *AlGaAs - HL* and *AlGaAs - LH* cells are given in Figure 4.6. The IV-curves for the *AlGaAs - Imp. free* and *AlGaAs - Imp.* cells are also included for comparison. In accordance with the performance parameters, the IV-curve for the *AlGaAs - HL* cell is substantially worse than the other cells.
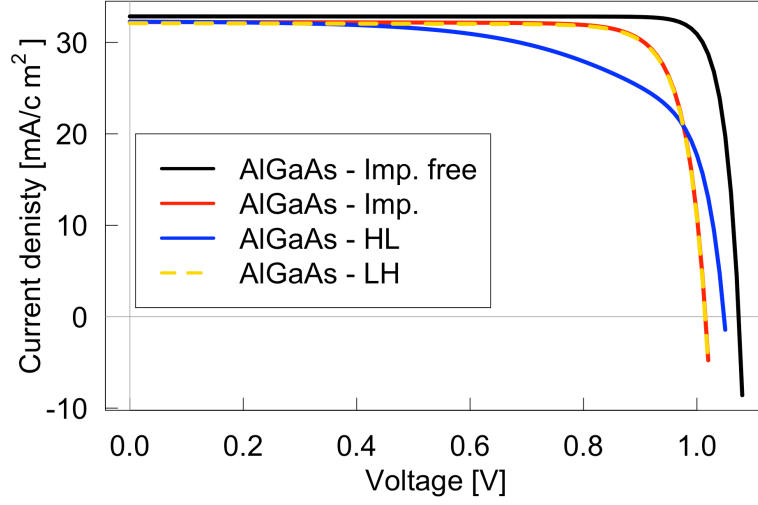

Figure 4.6: IV-curves for the *AlGaAs - Imp. free*, *AlGaAs - Imp.*, *AlGaAs - HL*, and *AlGaAs - LH* cells.

Energy Band Diagrams

The energy band diagrams at $V = V_{OC}$ for the *AlGaAs - HL* and *AlGaAs - LH* cells are given in Figure 4.7a and Figure 4.7b, respectively. As the doping concentrations are dissimilar between the cells are the shape of the bands also dissimilar.

(a) *AlGaAs - HL*
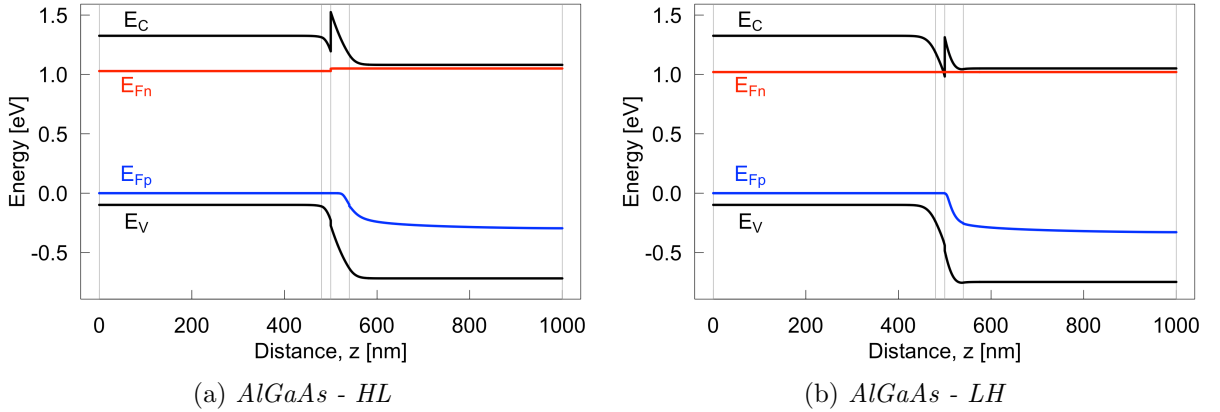
(b) *AlGaAs - LH*

Figure 4.7: The energy band diagrams at $V = V_{OC}$ for (a) the *AlGaAs - HL* cell and (b) the *AlGaAs - LH* cell. The vertical lines indicates the interfaces between the layers.

Recombination Rates

The radiative and SRH recombination rates at $V = V_{OC}$ for the *AlGaAs - HL* and *AlGaAs - LH* cells are given in Figure 4.8a and Figure 4.8b, respectively.

In order to more easily observe the change in recombination rates in layers 2 and 3 (see Figure 3.2) does Figure 4.8c and Figure 4.8d show the recombination rates from $z = 460$ nm to $z = 560$ nm at $V = V_{OC}$ for *AlGaAs - HL* and *AlGaAs - LH*, respectively.
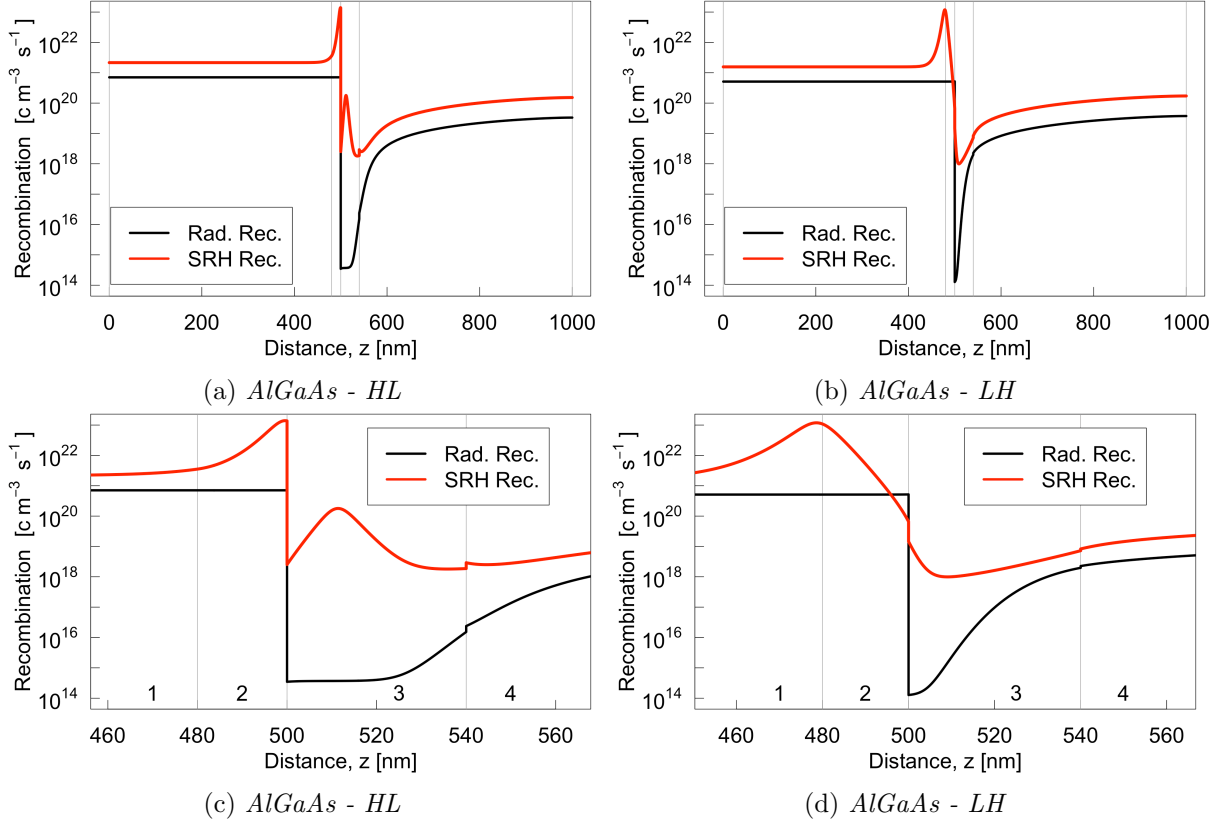

Figure 4.8: The radiative and SRH recombination rates at $V = V_{OC}$ for the *AlGaAs - HL* and *AlGaAs - LH* cellss. (a) and (b) shows the the entire cells, while (c) and (d) only shows from $z = 460$ nm to $z = 560$ nm. The vertical lines indicates the interfaces between the layers. The numbers 1 to 4 in (c) and (d) indicates the layers in the cells.

Discussion

Contrarily to the results from the GaInAsP/InP cells both here and in the paper by Santhanam and Fan, the increase in doping concentration in the p-layer and decrease in doping concentration in the n-layer close to the p-n interface resulted in a *reduction* in efficiency. This reduction was substantial at almost 17%. Two possible reasons are suggested to why this result is observed. Firstly, as the values of the doping concentrations used for the GaAs/AlGaAs cells are directly taken from GaInAsP/InP cells, it could be that these values are far from the optimal values for the GaAs/AlGaAs cells. It is therefore possible that all doping concentration values must be changed to observe a positive effect. By varying the doping concentrations in all layers and finding a set of values that results in the same effect as described by Santhanam and Fan in Ref. [11], this theory can be verified. However, this is likely not the reason as the observed reduction in efficiency is larger than one can expect from this explanation.

The second and more likely reason why the GaAs/AlGaAs had a substantial reduction in efficiency when the design principle was applied is that the CB offset in GaAs/AlGaAs seen in both Figure 4.7a and Figure 4.7b, changes how the cell behaves and responds to the changes. Figure 4.9a shows the CB offset for the *AlGaAs - Imp.* cell from $z = 460$ nm to $z = 560$ nm with the direction of electron flow *in* the CB (the blue arrow in the figure), the energy distance between the bulk position of the E_C in the p-type, and the minimum and maximum of the E_C in the p-n interface indicated. Figure 4.9b shows the same but for the *AlGaAs - HL* cell.

(a) *AlGaAs - Imp.*
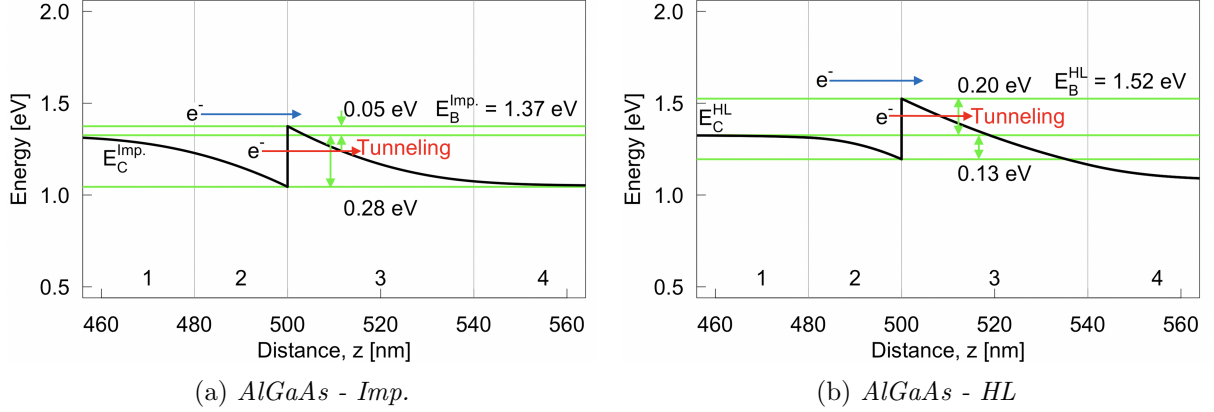
(b) *AlGaAs - HL*

Figure 4.9: The CB diagram at $V = V_{OC}$ from $z = 460$ nm to $z = 560$ nm for (a) the *AlGaAs - Imp.* cell and (b) the *AlGaAs - HL* cell. The blue arrows indicates the direction of the electron (e^-) flow *in* the CB. The red arrows indicates the direction of the electron (e^-) flow due to intra-band tunneling. The green lines are, from top to bottom, the maximum CB level in the p-n interface, the CB level in the bulk of the n-type, and the minimum CB level in the p-n interface. The green arrows and corresponding numbers are the energy distance between lines 1 and 2 and lines 2 and 3. The numbers 1 to 4 indicates the layers in the cells. The vertical lines indicates the interfaces between the layers.

Both Figure 4.9a and Figure 4.9b shows that there is a barrier for the electrons when they flow from the p-side to the n-side, and both barriers are of equal height at 0.23 eV. However, in the *AlGaAs - Imp.* cell is the difference between the peak value of E_C at $z = 500$ nm and the bulk value of E_C in layer 1 only 0.05 eV. Meanwhile, in *AlGaAs - LH* cell is the same difference four times larger at 0.20 eV. The efficiency of the *AlGaAs - Imp.* cell is high at $\eta = 27.31\%$, while the efficiency of the *AlGaAs - LH* cell is significantly lower at $\eta = 22.69\%$. It could therefore be that the increased difference between the bulk value of E_C and the peak value of E_C increases the negative effect the barrier has. This corresponds well with the fact that the other cell, *AlGaAs - LH*, has a very similar energy band diagram (Figure 4.7b) to the *AlGaAs - Imp.* cell (Figure 4.5a) without this increased difference in E_C, and their performances are almost identical. The subsequent paragraphs suggest one explanation to why this lift in the CB decreases the efficiency.

By using Eq.(2.3) with the quasi-Fermi level for electrons and integrating from the barrier energy E_B (as seen in e.g. Figure 4.9a) to the top of the CB E_{Top}, one obtains the total number of electrons in the CB above the barrier. This number is relevant because it tells how many electrons that can flow above the barrier and contribute to the current. For the *AlGaAs - Imp.* cell, using $m_n = 0.07\,m_e$, $E_{Fn} = 1.02$ eV, and $T = 300$ K, the number of electrons $n_{Imp.}$ above the barrier $E_B^{Imp.}$ is calculated to be

$$n_{Imp.} = \int_{E_B^{Imp.} = 1.37\,\mathrm{eV}}^{E_{Top} = 3\,\mathrm{eV}} N(E) \cdot F(E)\,\mathrm{d}E = 8.8 \cdot 10^{25}\,\mathrm{m}^{-3} \tag{4.1}$$

54

For the *AlGaAs - HL* cell, changing only the bottom integral limit to be E_{B}^{HL}, the number of electrons n_{HL} above the barrier is calculated to be

$$n_{\mathrm{HL}} = \int_{E_{\mathrm{B}}^{HL} = 1.52\,\mathrm{eV}}^{E_{\mathrm{Top}} = 3\,\mathrm{eV}} N(E) \cdot F(E)\,\mathrm{d}E = 8.1 \cdot 10^{25}\,\mathrm{m}^{-3} \tag{4.2}$$

For both integrals, the upper integration limit is chosen to be $E_{\mathrm{Top}} = 3\,\mathrm{eV}$. The only requirement for this integral limit is that it is high enough so that all electrons in the CB is included, and 3 eV is sufficiently high for these cells. Comparing $n_{\mathrm{Imp.}}$ and n_{HL} one can see that it is about 8.64% more available electrons in the *AlGaAs - Imp.* cell than in the *AlGaAs - HL* cell. This means fewer electrons can contribute to the current and the efficiency of the cells is reduced. Figure 4.10 illustrates the quantities $n_{\mathrm{Imp.}}$ and n_{HL}. In the figure, the black curve is the product of the density of states $N(E)$ and the Fermi-Dirac distribution $F(E)$. By convention is the energy on the y-axis and the electron density on the x-axis. Integrating with respect to the y-axis from E_{B}^{HL} to 3 eV then gives n_{HL}, which is illustrated by the red area. Next, integrating with respect to the y-axis from $E_{\mathrm{B}}^{Imp.}$ to 3 eV then gives $n_{\mathrm{Imp.}}$, which is illustrated by the sum of the red and blue areas.
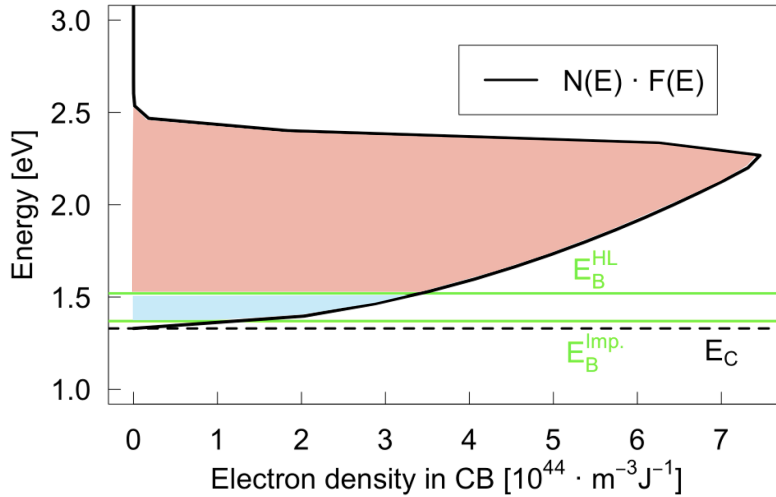

Figure 4.10: The black curve is the product of the density of states $N(E)$ and the Fermi-Dirac distribution $F(E)$. The red area is the total number of electrons n_{HL} above E_{B}^{HL}, and is calculated to be $8.1 \cdot 10^{25}\,\mathrm{m}^{-3}$. The sum of the red and the blue areas is the total number of electrons $n_{\mathrm{Imp.}}$ above $E_{\mathrm{B}}^{Imp.}$, and is calculated to be $8.8 \cdot 10^{25}\,\mathrm{m}^{-3}$.

To summarize, the reason why the CB offset hinders the positive effect of the design principle is that the change in doping raises the barrier in the CB which again reduces the electron flow. From this result one can also see that the decreased doping in the n-layer is the main problem, as this is what increases the CB. This corresponds well with the fact that the performance drop for the *AlGaAs - LH* cell is much less than for the *AlGaAs - HL* cell.

As stated in section 3.1, one of the fixed parameters for all the simulations is that no tunneling is allowed. However, in a CB barrier such as in the *AlGaAs - HL* and *AlGaAs - LH* cells, intra-band tunneling can occur. The electrons would then flow as indicated by the red arrow in Figure 4.9a and Figure 4.9b and contribute to the current. This will then effectively increase the number of available electrons, and although not all electrons will tunnel, the efficiency will improve. It is possible to allow for intra-band tunneling in SCAPS to investigate this further. However, due to time limitations this is not done in this thesis.

By comparing the recombination rates for the *AlGaAs - Imp.* and *AlGaAs - LH* cells (Figure 4.5b and Figure 4.8a, respectively), one can see that the most prominent difference is the shape of the SRH recombination curve in the thin n-AlGaAs layer at distance $z > 500$ nm. The *AlGaAs - HL* cell has an additional peak at $z \approx 515$ nm that the *AlGaAs - Imp.* does not have. Similarly, the *AlGaAs - LH* cell does not have this extra peak. This suggests that the barrier described above also creates location where the SRH recombination increases. To investigate this, the occupation probability of electrons in the impurities for the *AlGaAs - Imp.* and *AlGaAs - HL* cells are shown in Figure 4.11a and Figure 4.11b, respectively. Only in terms of the occupation probability of electrons, will the SRH recombination mechanism be most dominant where the probability is 50%. This is because then it will be an equal number of electrons and holes in the impurities, resulting in efficient carrier recombination. If the number is larger than 50%, there will not be enough holes for each electron to recombine with. By this logic it can seem counterintuitive that there are any SRH recombination when the occupation probability is 0% or 100% in the figures. The simple reason is that the values never are exactly 0% or 100%, just very close. This is not possible to see in the figures due to low vertical resolution, but have been verified in the simulation output files. Thus, even at a very low or a very high occupation probability, can the SRH recombination be high with a sufficient flow of carriers to the impurities.

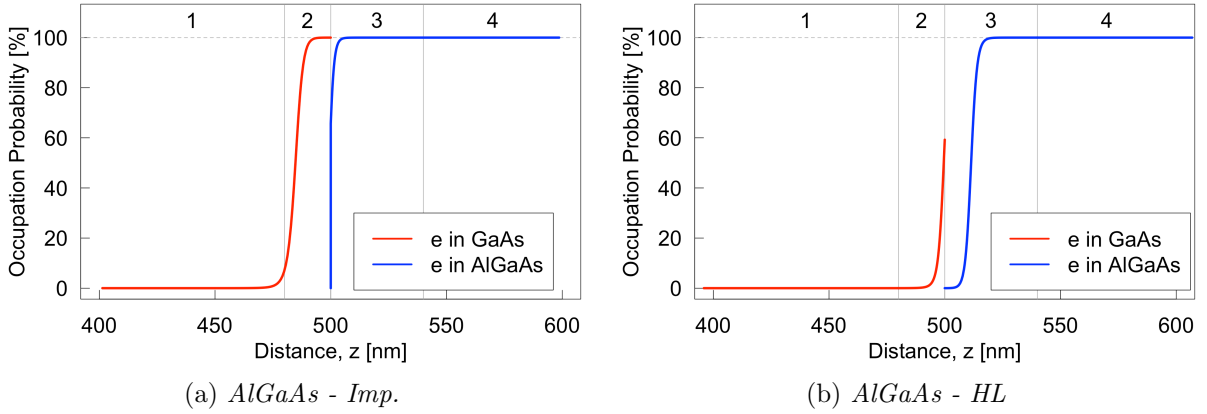(a) *AlGaAs - Imp.*   (b) *AlGaAs - HL*

Figure 4.11: The occupation probability of electrons in the impurities at $V = V_{OC}$ between $z = 400$ nm and $z = 600$ nm for (a) the *AlGaAs - Imp.* cell and (b) the *AlGaAs - HL* cell. The red curve represents the probability in the GaAs and the blue curve the probability in the AlGaAs. The numbers 1 to 4 indicates the layers in the cells, and the vertical lines indicates the interfaces between the layers.

Comparing the blue curves in Figure 4.11a and Figure 4.11b, one can see that the curve is less steep and shifted to the right for the *AlGaAs - HL* cell. This indicates that the SRH recombination rate is larger in first n-AlGaAs layer in the *AlGaAs - HL* cell than in the *AlGaAs - Imp.* cell. This is verified by their recombination rates in Figure 4.8a and Figure 4.5b, respectively. Then, comparing the red curves in the occupation probability figures, one can see that the value around 50% is shifted to the right. This would indicate more SRH recombination closer to the p-n interface in the *AlGaAs - HL* cell than in the *AlGaAs - Imp.* cell, which also is confirmed by their recombination rates.

Next, comparing the SRH recombination rates in the p-side ($z < 500$ nm) for the *AlGaAs - HL* and *AlGaAs - LH* cells (which is most easily seen in Figure 4.8c and Figure 4.8d), one can qualitatively see that the area under the curve for the recombination rate is largest for the *AlGaAs - LH* cell. A larger area under the SRH recombination curve means more total SRH recombination. In contrast, on the n-side and described above, the area under the SRH recombination curve is largest for the *AlGaAs - LH* cell. This suggests that it can be possible

the create a cell with increased doping concentration in both the p- and n-layers in proximity to the p-n interface to reduce the total SRH recombination. A possible explanation to this is that by increasing the doping concentrations, one effectively decreases the depletion region width. As the SRH recombination scales with $\exp\{(qV)/(k_{\mathrm{b}}T)\}$ outside the depletion region and with $\exp\{(qV)/(2\cdot k_{\mathrm{b}}T)\}$ within, can a narrower depletion region result in less SRH recombination. By this logic one can question why the doping of the whole cell shouldn't be increased. For these cells it could be true that a total increase in doping concentration would increase the efficiency as the doping concentrations are not optimized, but in general this is not true because an increased doping concentration also increases the band-to-band recombination. However, a reduction in depletion region width does also have drawbacks, and it is necessary to simulate such a high/high doping concentration cells before concluding on whether that configuration is beneficial.

Even though the most likely cause of the reduction in efficiency in the *AlGaAs - HL* is due to the CB offset, the subsequent subsection aims to first verify that the problem is not due to the numeric values of the doping concentrations. Also, this gives the opportunity to simulate a high/high doping concentration cell.

4.2.3 Varying Doping Concentrations

In this section, numerous cells have been simulated with the aim of finding the doping concentrations in layers 1, 2, 3, and 4 (the two former are p-doped and the two latter n-doped, see Figure 3.2) that results in the highest efficiency. The impurity parameters were kept equal to the ones in the cells in the previous section, and the thicknesses of the layers have been kept constant. Only the three most interesting cells have been given a name and are included here. These are the *AlGaAs - HH* cell (higher doping concentrations in layers 2 and 3 than in layers 1 and 4), the *AlGaAs - Uni.* cell (a new uniform optimized doping concentration in all layer), and the *AlGaAs - Uni. HH* cell (higher doping concentrations than the new uniform concentration in layers 2 and 3 than in layers 1 and 4). The doping concentrations for these cells are summarized in Table 3.6

Table 4.7: The three most interesting GaAs/AlGaAs cells from this section. The orange color in table represents values that changes from the previous row.

| Cell | Imp. | Doping Cons. $|N_{\mathrm{D}} - N_{\mathrm{A}}|$ [cm^{-3}] | | | |
		Layer 1	Layer 2	Layer 3	Layer 4
AlGaAs - HH	Yes	$2.0 \cdot 10^{17}$	$4.0 \cdot 10^{17}$	$4.0 \cdot 10^{17}$	$2.0 \cdot 10^{17}$
AlGaAs - Uni.	Yes	$9.0 \cdot 10^{17}$	$9.0 \cdot 10^{17}$	$9.0 \cdot 10^{17}$	$9.0 \cdot 10^{17}$
AlGaAs - Uni., HH	Yes	$9.0 \cdot 10^{17}$	$2.0 \cdot 10^{18}$	$2.0 \cdot 10^{18}$	$9.0 \cdot 10^{17}$

Results

Efficiencies

Table 4.8 shows the resulting efficiency when the doping concentration in the outer layers 1 (p-type) and 4 (n-type) (see Figure 3.2) is kept constant at $2 \cdot 10^{17}$ cm^{-3} and doping concentrations the middle layers 2 and 3 are varied between a lower value ($1 \cdot 10^{17}$ cm^{-3}), the same value ($2 \cdot 10^{17}$ cm^{-3}), and a higher value ($9 \cdot 10^{17}$ cm^{-3}). As can be seen from the table, three of these combinations have previously been simulated, namely the *AlGaAs - Imp.*, *AlGaAs - LH*, and *AlGaAs - HL* cells. Compared to the uniformly doped cell (*AlGaAs - Imp.*), only the cell with increased doping concentration in both middle layers, the *AlGaAs - HH* cell, saw an improvement in efficiency. The increase in efficiency in this cell compared to the uniformly doped cell was 0.12 percentage points from 27.31% to 27.43%.

Table 4.8: The relevant name, doping concentrations, and efficiency of nine GaAs/AlGaAs cells. The doping concentration in layers 1 and 4 is kept constant at $2 \cdot 10^{17}$ cm^{-3} and is not included in the table. The red color indicates a lower efficiency than that of the *AlGaAs - Imp.* cell, while the green color indicates a higher efficiency.

| | Doping Concentration | | |
| | N_A [cm^{-3}] | N_D [cm^{-3}] | |
Cell	GaAs - Layer 2	AlGaAs - Layer 3	Efficiency
AlGaAs - Imp.	$2.0 \cdot 10^{17}$	$2.0 \cdot 10^{17}$	27.31%
	$1.0 \cdot 10^{17}$	$1.0 \cdot 10^{17}$	27.29%
	$2.0 \cdot 10^{17}$	$1.0 \cdot 10^{17}$	26.73%
	$4.0 \cdot 10^{17}$	$2.0 \cdot 10^{17}$	26.94%
	$2.0 \cdot 10^{17}$	$4.0 \cdot 10^{17}$	27.23%
	$1.0 \cdot 10^{17}$	$2.0 \cdot 10^{17}$	27.29%
AlGaAs - LH	$1.0 \cdot 10^{17}$	$4.0 \cdot 10^{17}$	27.22%
AlGaAs - HL	$4.0 \cdot 10^{17}$	$1.0 \cdot 10^{17}$	22.69%
AlGaAs - HH	$4.0 \cdot 10^{17}$	$4.0 \cdot 10^{17}$	27.43%

Then, the doping concentrations in all layers were kept the equal and varied between $2 \cdot 10^{15}$ cm^{-3} and $1 \cdot 10^{19}$ cm^{-3}. Figure 4.12 shows how the efficiency was affected by this. The highest efficiency was found to be 27.85% at a uniform doping concentration of $9 \cdot 10^{17}$ cm^{-3}, and the cell with this concentration is labelled *AlGaAs - Uni.* The *AlGaAs - Uni.* has 4.5 times higher doping concentration than the *AlGaAs - Imp.* cell, and its efficiency is 0.54 percentage points higher.
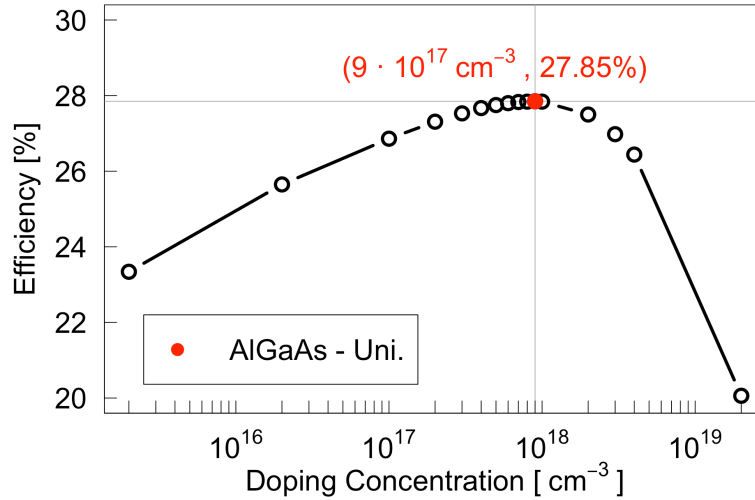

Figure 4.12: The efficiency as a function of uniform doping concentration in the GaAs/AlGaAs cells. The highest efficiency is found at a doping concentration of $9 \cdot 10^{17}$ cm^{-3} and this cell is labelled *AlGaAs - Uni.*

Using the new doping concentration of $9 \cdot 10^{17}$ cm^{-3} in layers 1 and 4, the simulations of Table 4.8 was repeated. In the paper by Santhanam and Fan was the concentration of the high doped layers two times higher compared to the bulk doping concentration, while the concentration of the low doped layers was half of the bulk doping concentration. This was used also here, and the lower doping was set to be $0.5 \cdot 9 \cdot 10^{17}$ cm$^{-3} \approx 4 \cdot 10^{17}$ cm^{-3} and the higher doping was set to be $2 \cdot 9 \cdot 10^{17}$ cm$^{-3} \approx 2 \cdot 10^{18}$ cm^{-3}. Table 4.9 summarizes the results from these simulations. Again, the results showed that only the one cell with higher doping concentration in both middle layers saw an improvement in efficiency compared to the uniformly doped cell.

The increase in efficiency in this cell compared to the *AlGaAs - Uni.* cell was 0.22 percentage points from 27.85% to 28.07%. This new cell is labelled *GaAs - Uni., HH*.

Table 4.9: The relevant names, doping concentration, and efficiency of nine GaAs/AlGaAs cells. The doping concentration in layers 1 and 4 is kept constant at $9 \cdot 10^{17}$ cm^{-3} and is not included in the table. The red color indicates a lower efficiency than that of the *AlGaAs - Uni.* cell, while the green color indicates a higher efficiency.

| | Doping Concentration | | |
| | N_A [cm^{-3}] | N_D [cm^{-3}] | |
Cell	GaAs - Layer 2	AlGaAs - Layer 3	Efficiency
AlGaAs - Uni.	$9.0 \cdot 10^{17}$	$9.0 \cdot 10^{17}$	27.85%
	$9.0 \cdot 10^{17}$	$2.0 \cdot 10^{18}$	27.62%
	$9.0 \cdot 10^{17}$	$4.0 \cdot 10^{17}$	26.41%
	$2.0 \cdot 10^{18}$	$9.0 \cdot 10^{17}$	26.67%
	$4.0 \cdot 10^{17}$	$4.0 \cdot 10^{17}$	27.55%
	$2.0 \cdot 10^{18}$	$4.0 \cdot 10^{17}$	18.05%
	4.0E+17	$9.0 \cdot 10^{17}$	27.60%
	4.0E+17	$2.0 \cdot 10^{18}$	26.98%
AlGaAs - Uni., HH	$2.0 \cdot 10^{18}$	$2.0 \cdot 10^{18}$	28.07%

The doping concentration in layers 2 (p-type) and 3 (n-type) was kept the same and varied between $1 \cdot 10^{18}$ cm^{-3} and $5 \cdot 10^{18}$ cm^{-3} while the doping concentration in layers 1 (p-type) and 4 (n-type) were kept constant at $9 \cdot 10^{17}$ cm^{-3}. Figure 4.13 graphically shows how the efficiency was affected by this. The highest efficiency was found to be at $2 \cdot 10^{18}$ cm^{-3}, i.e. previously simulated *AlGaAs - Uni., HH* cell.
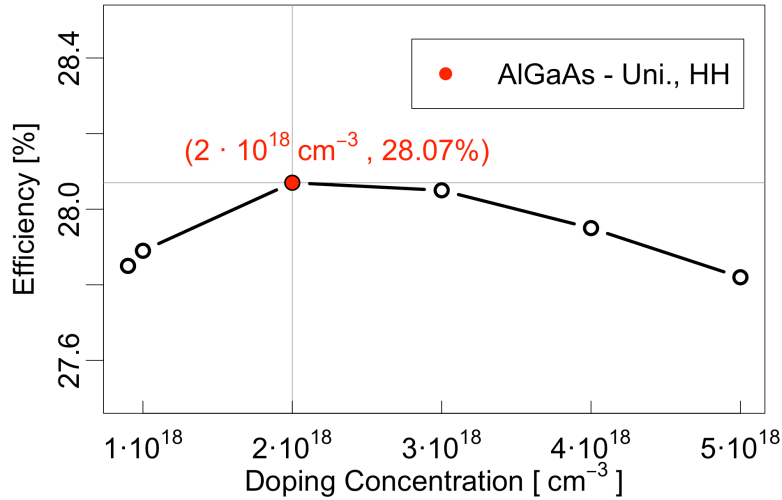
Figure 4.13: The efficiency as a function of the doping concentration in in the middle layers. The doping concentration in the outer layers were kept constant at $9 \cdot 10^{17}$ cm^{-3}.

Performance Parameters and IV-curves

The performance parameters for the *AlGaAs - HH*, *AlGaAs - Uni.*, and *AlGaAs - Uni., HH* cells are summarized in Table 4.10. The values for the previous cells are included for comparison. This table shows the same as described above, that the *AlGaAs - Uni., HH* cell performs best. The IV-curves for the *AlGaAs - HH*, *AlGaAs - Uni.*, and *AlGaAs - Uni., HH* cells are shown in Figure 4.14. Also here are the previous cells included for comparison. As can be seen in the figure are the curves hard to separate.

Table 4.10: The performance parameters for the *AlGaAs - HH*, *AlGaAs - Uni.*, and *AlGaAs - Uni., HH* cells

	η [%]	J_{SC} [mA/cm^2]	V_{OC} [V]	FF [%]
AlGaAs - Imp.	27.31	32.24	1.02	83.44
AlGaAs - HL	22.69	32.27	1.05	67.11
AlGaAs - LH	27.21	32.11	1.01	83.58
AlGaAs - HH	27.43	32.17	1.02	83.76
AlGaAs - Uni.	27.85	31.53	1.04	84.85
AlGaAs - Uni., HH	28.07	31.32	1.05	85.38
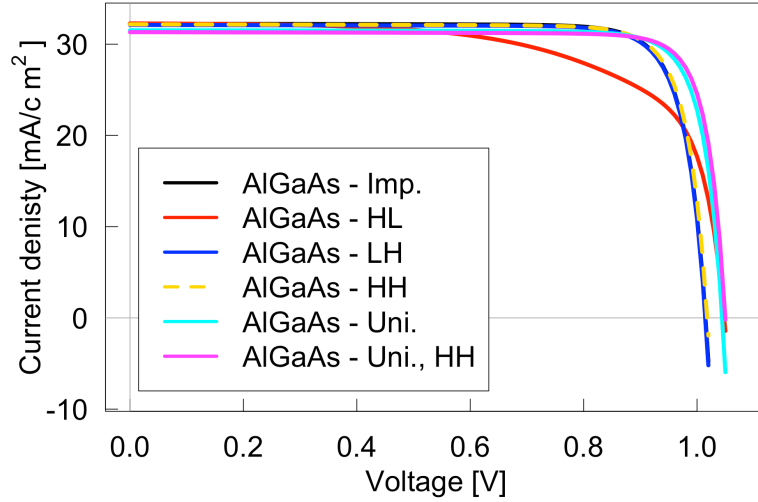
Figure 4.14: IV-curves for the *AlGaAs - HH*, *AlGaAs - Uni.*, and *AlGaAs - Uni., HH* cells.

Energy Band Diagrams

The energy band diagram at $V = V_{\text{OC}}$ for the *AlGaAs - Imp.*, *AlGaAs - HH*, *AlGaAs - Uni.*, and (d) the *AlGaAs - Uni., HH* cells are shown in Figure 4.15a, Figure 4.15b, Figure 4.15c, and Figure 4.15d, respectively. The energy band diagram for the *AlGaAs - Imp.* cell is shown again here so it is easily comparable to the other energy band diagrams.

Recombination Rates

The radiative and SRH recombination rates at $V = V_{\text{OC}}$ for the *AlGaAs - Imp.* and *AlGaAs - HH* cells are given in Figure 4.16a and Figure 4.16b, respectively. The figure for the *AlGaAs - Imp.* cell is repeated here also for comparison. To better inspect the effect of the changed doping concentrations, Figure 4.16c and Figure 4.16d shows the the recombination rates from $z = 460$ nm to $z = 560$ nm at $V = V_{\text{OC}}$ for the *AlGaAs - Imp.* and *AlGaAs - HH* cells, respectively.

Next, the radiative and SRH recombination rates at $V = V_{\text{OC}}$ for the *AlGaAs - Uni.* and *AlGaAs - Uni., HH* cells are given in Figure 4.17a and Figure 4.17b, respectively. The peaks of the SRH recombination curves for the these cells hits the edge of the figure but does not exceed it. The y-axes are not changed so comparisons with the other SRH recombination rates are more convenient. Again, to better inspect the effect of the changed doping concentrations, Figure 4.17c and Figure 4.17d shows the the recombination rates from $z = 460$ nm to $z = 560$ nm at $V = V_{\text{OC}}$ for the *AlGaAs - Uni.* and *AlGaAs - Uni., HH* cells, respectively.

(a) *AlGaAs - Imp.*

(b) *AlGaAs - HH*

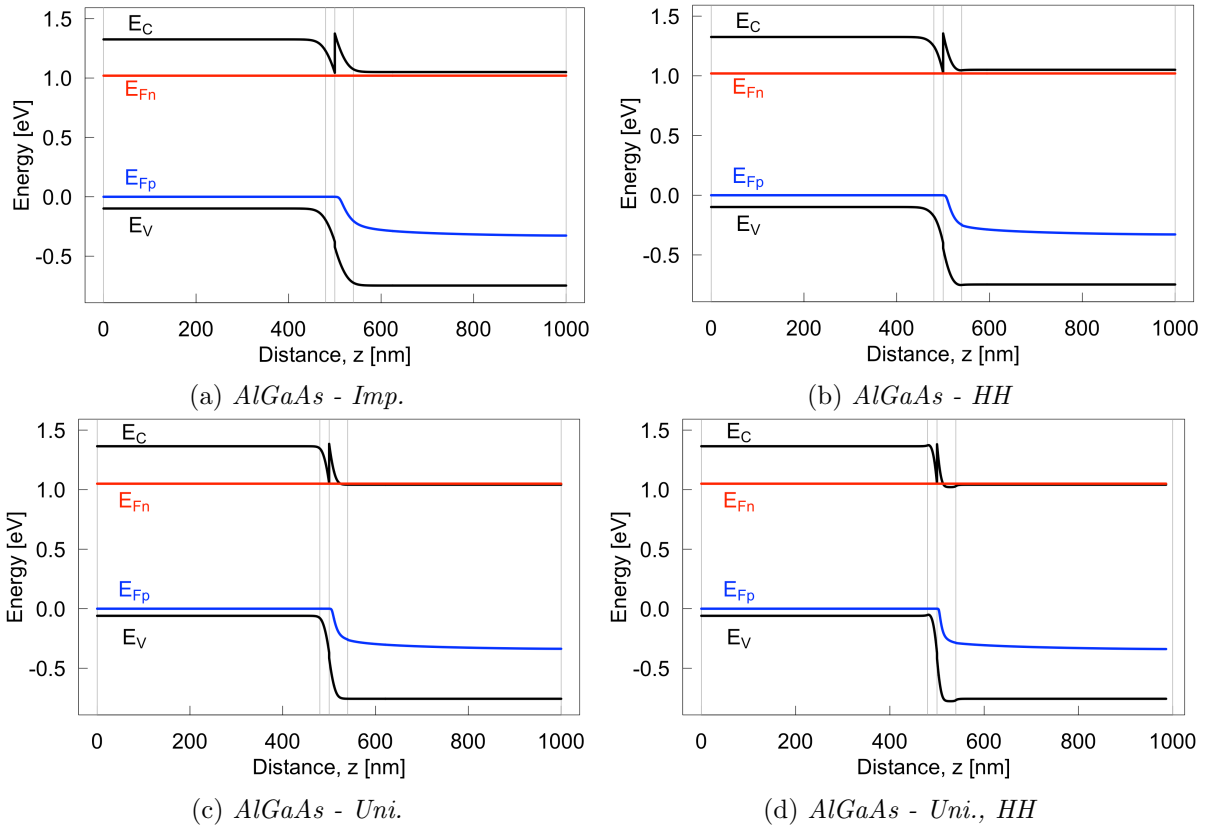(c) *AlGaAs - Uni.*

(d) *AlGaAs - Uni., HH*

Figure 4.15: The energy band diagrams at $V = V_{\text{OC}}$ for (a) the *AlGaAs - Imp.* cell, (b) the *AlGaAs - HH* cell, (c) the *AlGaAs - Uni.* cell, and (d) the *AlGaAs - Uni., HH* cell. The vertical lines indicates the interfaces between the layers.
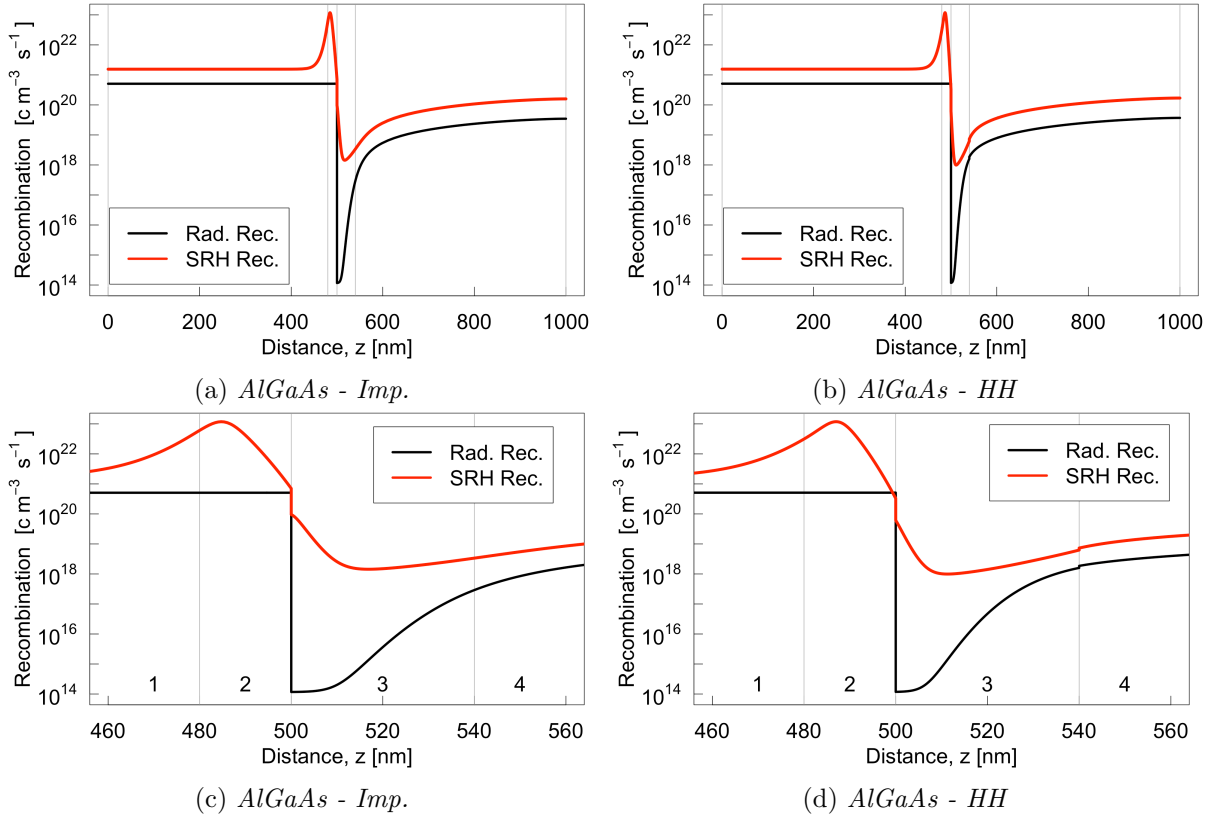
Figure 4.16: The radiative and SRH recombination rates at $V = V_{\text{OC}}$ for the $AlGaAs$ - $Imp.$ and $AlGaAs$ - HH cells. (a) and (b) shows the the entire cells, while (c) and (d) only shows from $z = 460$ nm to $z = 560$ nm. The vertical lines indicates the interfaces between the layers. The numbers 1 to 4 in (c) and (d) indicates the layers in the cells.

(a) *AlGaAs - Uni.*

(b) *AlGaAs - Uni., HH*

(c) *AlGaAs - Uni.*
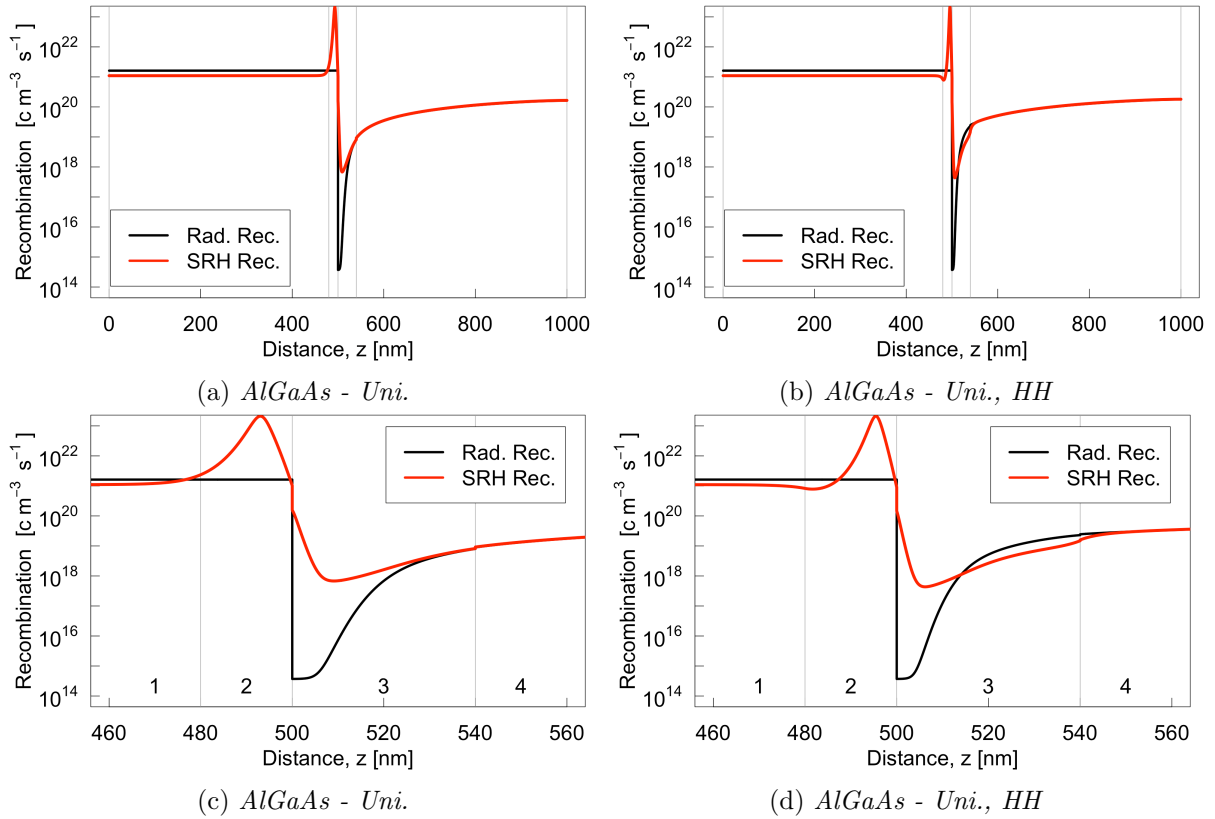
(d) *AlGaAs - Uni., HH*

Figure 4.17: The radiative and SRH recombination rates at $V = V_{OC}$ for the *AlGaAs - Uni.* and *AlGaAs - Uni., HH* cells. (a) and (b) shows the the entire cells, while (c) and (d) only shows from $z = 460$ nm to $z = 560$ nm. The vertical lines indicates the interfaces between the layers. The numbers 1 to 4 in (c) and (d) indicates the layers in the cells.

Discussion

As suggested in subsection 4.2.2, the results in Table 4.8 show that the cell with increased doping concentration in both middle layers, i.e. the *AlGaAs - HH* cell, saw an improvement in efficiency. Compared to the uniformly doped cell (*AlGaAs - Imp.*), the improvement was 0.12 percentage points. In addition, *only* the *AlGaAs - HH* cell had a positive effect of the changes. However, this effect is not the same as the one in the paper by Santhanam and Fan [11]. Actually, as can be seen by the SRH recombination rates of the *AlGaAs - Imp.* and *AlGaAs - HH* cells in Figure 4.15a and Figure 4.15b, respectively, the peak value *increased* slightly (from $1.183 \cdot 10^{23}$ cm^{-3}s^{-1} to $1.184 \cdot 10^{23}$ cm^{-3}s^{-1}). This is the opposite effect of what Santhanam and Fan achieved. Instead, as can more easily be seen when the recombination rates are shown between $z = 460$ nm and $z = 560$ nm in Figure 4.16c and Figure 4.16d, the improvement comes from a decrease in width of the SRH recombination curve in layer 2 and a slightly larger dip in layer 3.

The best uniform doping concentration was found to be $9 \cdot 10^{17}$ cm^{-3}. As the initial used value was taken from the GaInAsP/InP cells, it is not surprising that a new, better value was found. As can be seen from the curve of the efficiency as a function of doping concentration in Figure 4.12, there is an optimum value due to a trade-off when increasing the doping concentration. Initially, between a doping concentration of $2 \cdot 10^{15}$ cm^{-3} and $9 \cdot 10^{17}$ cm^{-3}, the efficiency increases with increasing doping concentration. This is because with with higher doping concentration will the energy difference between the quasi-Fermi levels also increase. This will, as described by Eq.(2.5), increase the voltage the cell can produce, which results in a higher efficiency. However, between a doping concentration of $9 \cdot 10^{17}$ cm^{-3} and $1 \cdot 10^{19}$ cm^{-3} does the efficiency drop with increased doping concentration. This is because with increased doping concentration, do the carrier populations in the bands also increase, which results in a higher band-to-band recombination rate. This makes the doping concentration a trade-off problem, and for the *AlGaAs - Uni.* cell is the concentration of $9 \cdot 10^{17}$ cm^{-3} the value that best balances this.

Comparing the radiative recombination rates for the lower uniformly doped cell *AlGaAs - Imp.* and the optimal uniformly doped cell *AlGaAs - Uni.* (Figure 4.16a and Figure 4.17a, respectively), one can see that the radiative recombination rate increases in the latter. For the bulk of the first GaAs layer (layer 1), this value increases by approximately 219% from $5.094 \cdot 10^{20}$ cm^{-3}s^{-1} to $1.627 \cdot 10^{21}$ cm^{-3}s^{-1}. However, by comparing the efficiencies and open-circuit voltages for the same cell shown in Table 4.10, one can see that both improves for the *AlGaAs - Uni.* cell. This shows what was described in the paragraph above, that increased doping concentration increases band-to-band recombination and the voltage, and that the *AlGaAs - Uni.* cell optimizes this better than the *AlGaAs - Imp.* cell.

From the results in Table 4.9, one can see that even at the optimized, uniform doping concentration did an increase in the doping concentration in the middle layers result in an increase in efficiency. As can be in Figure 4.13, the optimum value of this middle layer doping concentration was the value initially tried. Again, the improvement due to the high-high doping cannot be the same as what was observed by Santhanam and Fan. This is because they aim to move the peak SRH recombination value out of the depleting region and into the wide bandgap material where it scales with the intrinsic carrier concentration. This does not happen here as the doping concentration is changed equally on both sides of the p-n interface, causing no movement in the depletion region. Instead the improvement is due to an optimization of the doping concentration and the depletion region width. As described previously, an optimized doping concentration balances the voltage and the band-to-band recombination. A smaller depletion region results in a smaller area where the SRH recombination scales with $\exp\{qV/2k_\mathrm{b}T\}$, which results in a lower total SRH recombination. A larger depletion region results in a larger area

with an electric field, which results in a larger area where an generated electron-hole pair can be separated. However, this also depends on other factor, such as the lifetime of the carriers. The *AlGaAs - Uni., HH* cell balances these factors optimally to produce a better performing cell.

It is always desirable to make better performing cells, so it could in theory be useful to further investigate cells with higher doping concentrations around the p-n interface. However, the improvement between the *AlGaAs - Uni.* cell and the *AlGaAs - Uni., HH* is very small at only 0.80%. In addition are both cell performances already very good, and simply making a real version of the *AlGaAs - Uni.* cell would be a substantial improvement of today's solar cell technology. The conclusion is thus that since a slightly performance increase is obtained will the high/high doping also be tested in some of the upcoming cells, but the aim is still to obtain the same results as Santhanam and Fan.

The results from this subsection shows showed that the problem with the cells in subsection 4.2.2 not was due to the doping concentrations being far from their optimal values. This strongly suggests that the problems stems from the CB offset ΔE_C between GaAs and AlGaAs. This offset can *mathematically* be removed by changing the electron affinity of the materials. By inspecting the numerical values of E_C at both sides of the p-n interface in the band diagram for the *AlGaAs - Uni* cell (Figure 4.15c), the magnitude of the CB offset $\Delta E_\mathrm{C}^{Uni.}$ was found to be

$$\Delta E_\mathrm{C}^{Uni.} = 1.38 \text{ eV} - 1.05 \text{ eV} = 0.33 \text{ eV} \tag{4.3}$$

Using Anderson's rule and Eq.(2.6) (while keping the value of the electron affinity of AlGaAs χ_AlGaAs constant at 3.740 eV), the following equation modifies the real value of the GaAs electron affinity $\chi_\mathrm{GaAs,\ old}$ to a new value $\chi_\mathrm{GaAs,\ new}$ so that the CB offset becomes zero.

$$\chi_\mathrm{GaAs,\ new} = \chi_\mathrm{GaAs,\ old} - \Delta E_\mathrm{C}^{Uni.} = 4.07 \text{ eV} - 0.33 \text{ eV} = 3.74 \text{ eV} \tag{4.4}$$

In the subsequent simulations this modified value, $\chi_\mathrm{GaAs,\ new} = 3.74$ eV, is used to verify that the CB offset indeed is the cause of the problems. However, it is important to state that the electron affinity is an intrinsic material property. It thus not possible to change this value in real GaAs, and this is only done here to verify the problem. All cells using this modified value of the electron affinity will therefore be marked *GaAs** to separate it from *real* GaAs.

4.3 Modified GaAs Cells

This section aims investigates the design principle by Santhanam and Fan in Ref. [11] and aspects around this on p-GaAs*/n-AlGaAs cells were the electron affinity of the GaAs have been modified as described in subsection 4.2.3 to remove its native CB offset. The section is dividend into five parts: Conduction Band Offset (subsection 4.3.1), Inhomogeneous Doping Concentration (subsection 4.3.2), Low Light Performance (subsection 4.3.3), Low Efficiency Modified GaAs/AlGaAs Cells (subsection 4.3.4), and Layer Thickness Variation (subsection 4.3.5).

4.3.1 Conduction Band Offset

Results

As described in section 4.2.3, Anderson's rule can be applied to remove the CB offset. This was done here, and resulted in a new cell denoted *GaAs* - Uni.*, where the asterisk indicates the modification of the electron affinity. Figure 4.18a and Figure 4.18b compares the energy band diagram at $V = V_{\mathrm{OC}}$ of the *AlGaAs - Uni.* and *GaAs* - Uni.* cells, respectively. The results showed that the offset was changed from $\Delta E_{\mathrm{C}} = 0.33$ eV to $\Delta E_{\mathrm{C}} = 0$ eV.

(a) *AlGaAs - Uni.*   (b) *GaAs* - Uni.*
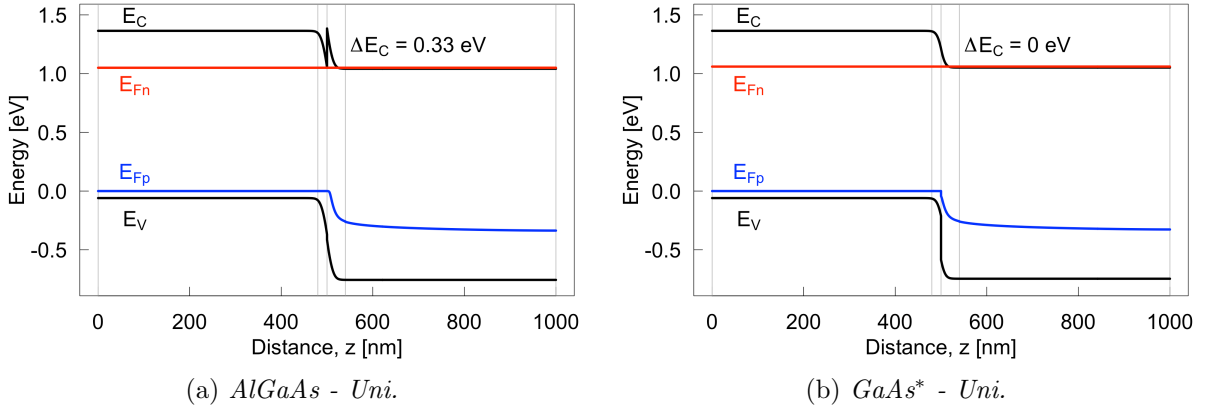
Figure 4.18: The energy band diagrams at $V = V_{\mathrm{OC}}$ of (a) the *AlGaAs - Uni.* cell and (b) the *GaAs* - Uni.* cell. The CB offset ΔE_{C} is 0.33 eV for (a) and 0 eV for (b). The vertical lines indicates the interfaces between the layers.

Discussion

The application of Anderson's rule gave the desired result, i.e. removing the CB offset. It should be noted that as the two band edges E_{V} and E_{C} always are parallel, the modification also slightly changes the shape of the VB edge. Regardless, this new cell (*GaAs* - Uni.*) can now be used to investigate whether the problems with the cells in the two previous sections were due to the offset. It is again reminded that the change in electron affinity is not possible in real GaAs as it is an intrinsic property. However, it is still usefully to investigating modified GaAs*/AlGaAs cells, as this can verify if the CB offset is the cause of the problems. In addition, the subsequent results will be relevant for any band offset-free heterojunctions.

4.3.2 Inhomogeneous Doping Concentration

This subsection aims to apply the design principle by Santhanam and Fan, i.e. changing the doping concentration around the p-n interface, on the new $GaAs^*$ - $Uni.$ cell. This resulted in three new cells: $GaAs^*$ - HL, $GaAs^*$ - LH and $GaAs^*$ - HH, where the H and L denotes a *higher* or *lower* doping concentration in layer 2 (p-type) and layer 3 (n-type) (see Figure 3.4 for schematic illustration of the cell layers).

Results

Performance Parameters and IV-curves

The performance parameters for the four modified GaAs*/AlGaAs cells are presented in Table 4.11. The result shows that both the $GaAs^*$ - HL and $GaAs^*$ - HH cells outperformed the $GaAs^*$ - $Uni.$ cell in efficiency, while the opposite is true for the $GaAs^*$ - LH cell. The efficiency increase between $GaAs^*$ - $Uni.$ and $GaAs^*$ - HL is 1.19 percentage points or 4.19%.

The IV-curves of the $GaAs^*$ - $Uni.$, $GaAs^*$ - HL, $GaAs^*$ - LH, and $GaAs^*$ - HH cells are presented in Figure 4.19. The curves are hard to separate in the figure.

Table 4.11: Performance parameters for the $GaAs^*$ - $Uni.$, $GaAs^*$ - HL, $GaAs^*$ - LH, and $GaAs^*$ - HH cells.

	η [%]	J_{SC} [mA/cm^2]	V_{OC} [V]	FF [%]
$GaAs^*$ - $Uni.$	28.39	31.50	1.05	85.83
$GaAs^*$ - HL	29.58	31.58	1.06	88.39
$GaAs^*$ - LH	27.20	31.20	1.04	83.96
$GaAs^*$ - HH	28.49	31.28	1.05	86.44
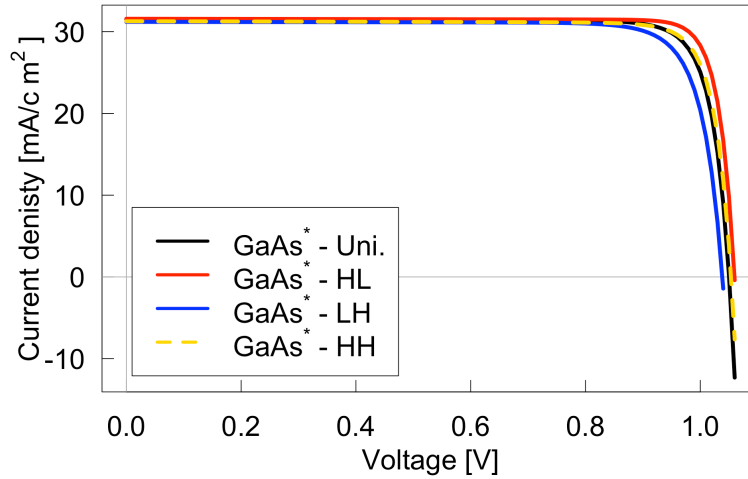
Figure 4.19: IV-curves for the $GaAs^*$ - $Uni.$, $GaAs^*$ - HL, $GaAs^*$ - LH, and $GaAs^*$ - HH cells.

Energy Band Diagrams

The energy band diagrams at $V = V_{OC}$ for the $GaAs^* - Uni.$, $GaAs^* - HL$, $GaAs^* - LH$, and $GaAs^* - HH$ cells can be found in Figure 4.20a, Figure 4.20b, Figure 4.20c, and Figure 4.20d, respectively.

(a) $GaAs^* - Uni.$
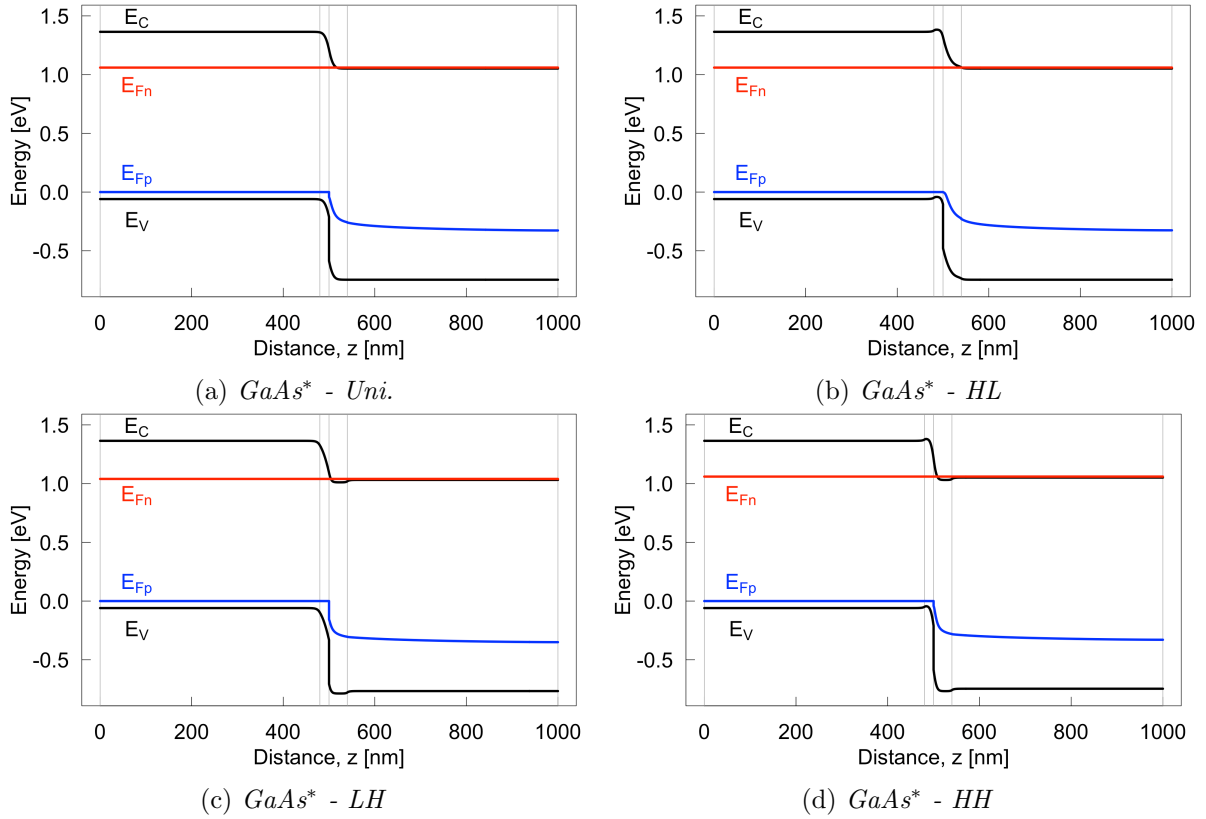
(b) $GaAs^* - HL$

(c) $GaAs^* - LH$

(d) $GaAs^* - HH$

Figure 4.20: The energy band diagrams at $V = V_{OC}$ for (a) the $GaAs^* - Uni.$ cell, (b) the $GaAs^* - HL$ cell, (c) the $GaAs^* - LH$ cell, and (d) the $GaAs^* - HH$ cell. The vertical lines indicates the interfaces between the layers.

Recombination Rates

The radiative and SRH recombination rates $V = V_{OC}$ for the entire cell and between $z = 460$ nm and $z = 560$ nm for the $GaAs^* - Uni.$ cell are given in Figure 4.21a and Figure 4.21b, respectively. Next, the radiative and SRH recombination rates $V = V_{OC}$ for the entire cell and between $z = 460$ nm and $z = 560$ nm for the $GaAs^* - HL$ cell are given in Figure 4.21c and Figure 4.21d, respectively.

(a) $GaAs^* - Uni.$

(b) $GaAs^* - Uni.$
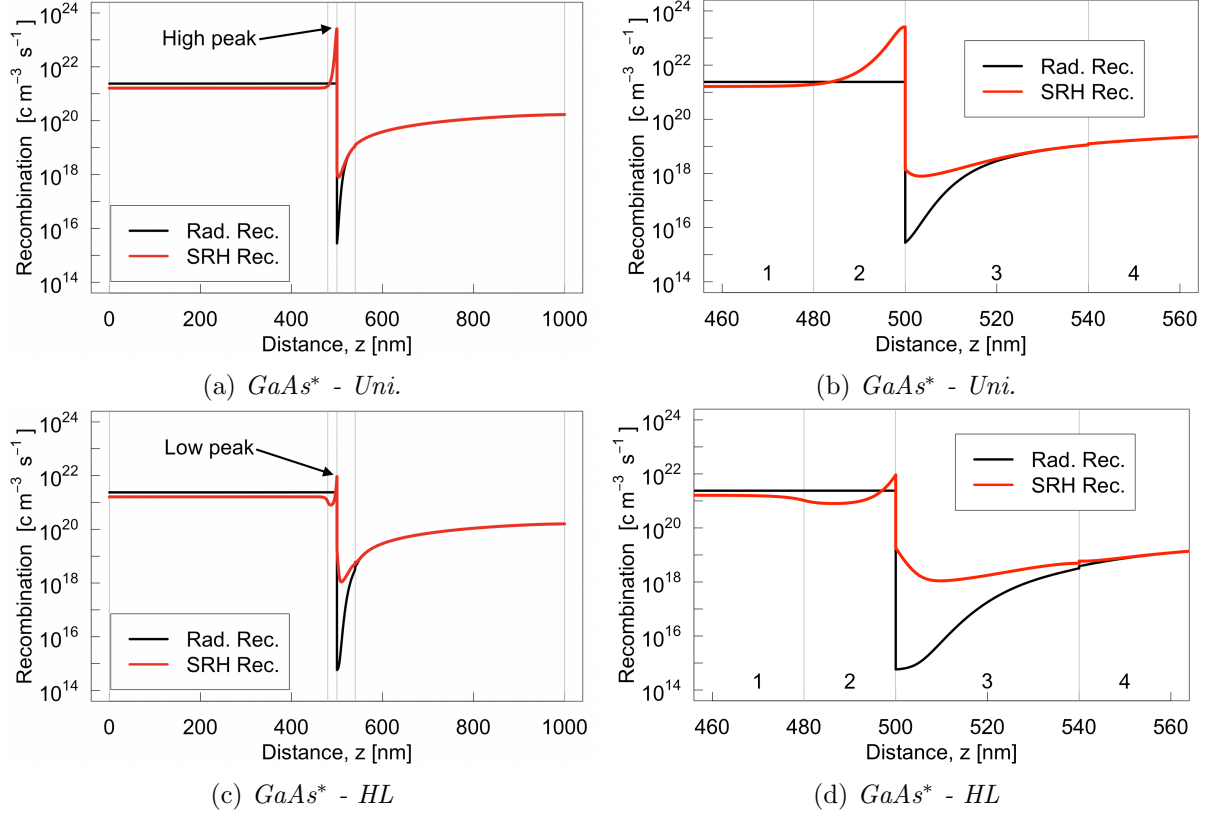
(c) $GaAs^* - HL$

(d) $GaAs^* - HL$

Figure 4.21: Radiative and SRH recombination rates at $V = V_{OC}$. (a) and (b) are the $GaAs^* - Uni.$ cell shown for the entire cell and between $z = 460$ nm to $z = 560$ nm, respectively. (c) and (d) are the $GaAs^* - HL$ cell shown for the entire cell and between $z = 460$ nm to $z = 560$ nm, respectively. The numbers 1 to 4 in (b) and (d) indicates the layers in the cells. The vertical lines indicates the interfaces between the layers.

The radiative and SRH recombination rates $V = V_{\mathrm{OC}}$ for the entire cell and between $z = 460$ nm and $z = 560$ nm for the $GaAs^*$ - LH cell are given in Figure 4.22a and Figure 4.22b, respectively. Next, the radiative and SRH recombination rates $V = V_{\mathrm{OC}}$ for the entire cell and between $z = 460$ nm and $z = 560$ nm for the $GaAs^*$ - HH cell are given in Figure 4.22c and Figure 4.22d, respectively.

(a) $GaAs^*$ - LH

(b) $GaAs^*$ - LH
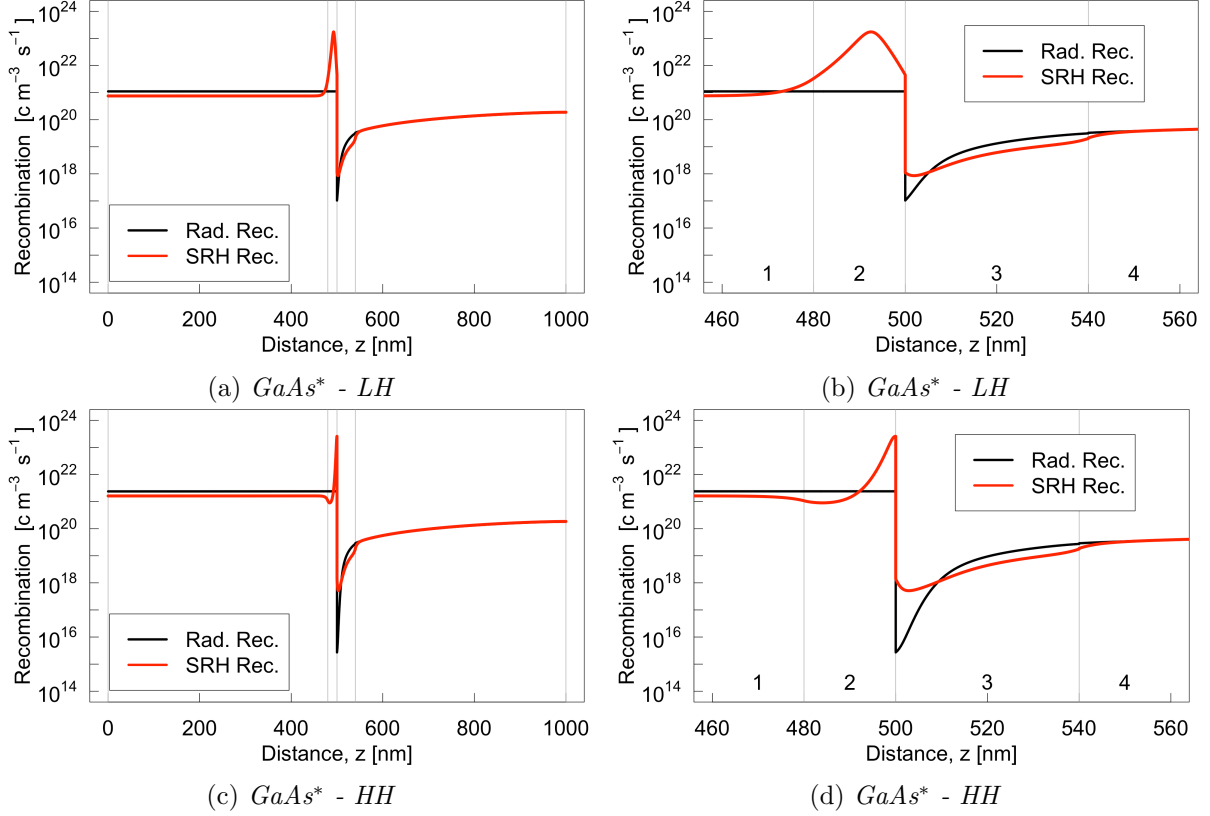
(c) $GaAs^*$ - HH

(d) $GaAs^*$ - HH

Figure 4.22: Radiative and SRH recombination rates at $V = V_{\mathrm{OC}}$. (a) and (b) are the $GaAs^*$ - LH cell shown for the entire cell and between $z = 460$ nm to $z = 560$ nm, respectively. (c) and (d) are the $GaAs^*$ - HH cell shown for the entire cell and between $z = 460$ nm to $z = 560$ nm, respectively. The numbers 1 to 4 in (b) and (d) indicates the layers in the cells. The vertical lines indicates the interfaces between the layers.

Discussion

The main takeaway from these result is that by removing the CB offset in p-GaAs/n-AlGaAs cells did the design principle by Santhanam and Fan have a positive effect, and that this effect is the same as in their paper in Ref. [11]. This can most easily be seen by comparing the SRH recombination rates for the $GaAs^*$ - $Uni.$ and $GaAs^*$ - HL cells in Figure 4.21a and Figure 4.21c, respectively, where the peak SRH recombination values are indicated. This peak value at $z = 500$ nm drops substantially by a factor 27.8 (from $2.57 \cdot 10^{23}$ cm^{-3}s^{-1} to $9.22 \cdot 10^{21}$ cm^{-3}s^{-1}) between the $GaAs^*$ - $Uni.$ and $GaAs^*$ - HL cells. There are two things that occurs to make this happen. Firstly, the change in doping concentration, more specifically a high concentration in the p-layer and a low in the n-layer, moves the depletion region and the SRH recombination peak from the $GaAs^*$ - $Uni.$ cell to the right. This means that the peak now is in the wide bandgap material AlGaAs. As the peak scales with the intrinsic carrier concentration, a quantity that is smaller in AlGaAs than GaAs (both modified GaAs and real GaAs), does the the peak drop substantially. As the peak value of the SRH recombination rate is about 159

times higher than the bulk value in the GaAs*-layer and 1525 times higher than the bulk value of the AlGaAs-layer in the $GaAs^*$ - $Uni.$ cell, does the peak drop substantially contribute to a total drop in SRH recombination and an increase in efficiency.

The $GaAs^*$ - LH performed worse than the $GaAs^*$ - $Uni.$ cell. Comparing the SRH recombination rates for these two cells (Figure 4.22a and Figure 4.21a, respectively), one can see that the peak value in the depletion region still decreases (from $2.57 \cdot 10^{23}$ cm^{-3}s^{-1} to $1.75 \cdot 10^{22}$ cm^{-3}s^{-1}). This is an unexpected result because if one applies the logic behind Santhanam and Fan's principle one should in the $low/high$ configuration move the peak value of the SRH recombination to the GaAs where it scales with (the larger) intrinsic carrier concentration. The fact that the peak SRH recombination decreases and the efficiency also decreases illustrates that there are other effects than the scaling with the intrinsic carrier concentration that occurs when inhomogeneous doping concentrations is applied to the cell. However, as the $low - high$ configuration resulted in lower efficiency anyways, the reason for this unexpected result is not concluded on in this thesis.

For the $GaAs^*$ - HH cell the peak value is almost unchanged (rounded to two decimals are both values $2.57 \cdot 10^{17}$ cm^{-3}s^{-1} but the value is slightly higher for $GaAs^*$ - HL), while the minimum value drops slightly (from $7.95 \cdot 10^{17}$ cm^{-3}s^{-1} to $5.14 \cdot 10^{22}$ cm^{-3}s^{-1}). This is expected as an equal change in doping concentration around the depletion region results in no movement or significant scaling of the SRH recombination peak. However, the efficiency of the $GaAs^*$ - HH cell is still slightly better than for the $GaAs^*$ - $Uni.$ cell, again showing that increasing the doping concentration around the p-n interface can yield in a positive result. The reason for this is not due the same as in the $GaAs^*$ - HL cell and in the cells by Santhanam and Fan, but is the same as for the $AlGaAs$ - $Uni., HH$ cell in section 4.2.3. In summary, these results shows that only the doping combination $High/Low$ in layers 2 (p-type and 3 (n-type) yields in the change in the SRH recombination rates which improves the efficiency in accordance with Santhanam and Fan [11].

The maximum power point P_M and the corresponding voltage V_M of the $GaAs^*$ - $Uni.$ and $GaAs^*$ - HL cells are calculated here for the subsequent discussion on the SRH recombination rate at different voltages. This is done by multiplying the current and the voltage from the black and red curves in Figure 4.19, and plotting this against the voltage. The result of this for the $GaAs^*$ - $Uni.$ and $GaAs^*$ - HL cells are shown in Figure 4.23 again as the black and red curves, respectively. The maximum power points were calculated to be 28.39 mW/cm^2 and 29.57 mW/cm^2 for the $GaAs^*$ - $Uni.$ and $GaAs^*$ - HL cells, respectively. The corresponding voltages, i.e. V_M, were then calculated to be 0.94 V and 0.96 V for the $GaAs^*$ - $Uni.$ and $GaAs^*$ - HL cells, respectively. The numeric values of P_M and V_M are summarized in Table 4.12. These results shows that the maximum power the cell can produce increases when the design principle is applied.

Table 4.12: The maximum power point P_M and the corresponding voltage V_M the $GaAs^*$ - $Uni.$ and $GaAs^*$ - HL cells.

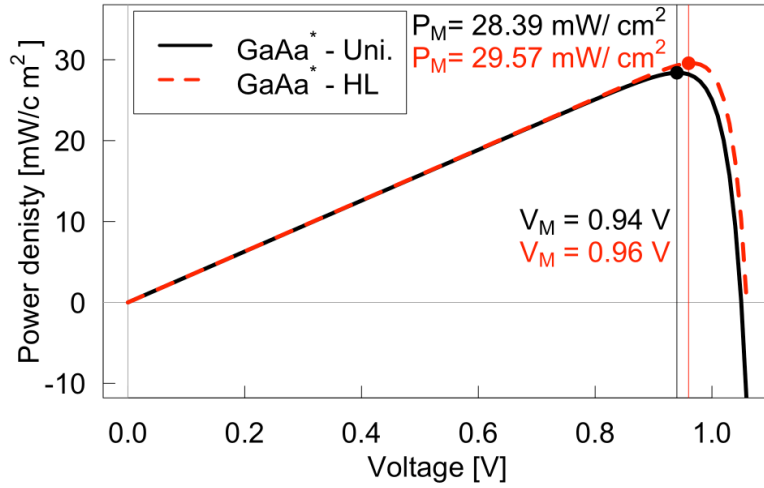|	P_M [mW/cm^2]	V_M [V]
$GaAs^*$ - $Uni.$	28.39	0.94
$GaAs^*$ - HL	29.57	0.96

Figure 4.23: The power curve for the $GaAs^*$ - Uni. and $GaAs^*$ - HL cells. The maximum power point for the two cells are indicated by the black and red circles, while the corresponding voltage is indicated by the black and red vertical lines.

Using the values of V_M calculated above, the SRH recombination rates at these voltages for the $GaAs^*$ - Uni. and the $GaAs^*$ - HL cells can obtained in SCAPS [12]. Thus, the SRH recombination rates at $V = V_{OC}$ and $V = V_M$ the $GaAs^*$ - Uni. and the $GaAs^*$ - HL cells are shown in Figure 4.24a and Figure 4.24b, respectively. The first interesting aspect of these figures is that they shows how the SRH recombination rates scales differently with voltage outside and inside the depletion region, with and without the design principle applied. The SRH recombination rate scales with $\exp\{qV/nk_bT\}$, where n is the ideality factor which is equal to 1 outside the depletion region and 2 within. For the $GaAs^*$ - Uni. cell in Figure 4.24a, the voltage difference between the curves are 0.11 V. As can be seen by the two numbers in the figure, the peak value only drops by a factor 10.15 while the bulk value for GaAs* drops by a factor 64.92. This is the main motivation behind the principle, that at lover voltages will the peak value of the SRH recombination in the depletion region be the dominant loss mechanism, and thus needs to be reduced. For the $GaAs^*$ - HL cell in Figure 4.24b, the voltage difference between the curves are almost the same at 0.10 V. However, the drop in the the peak value is much larger at a factor 24.66 due to the design changes, thus improving on the efficiency.

The second interesting aspect of Figure 4.24a and Figure 4.24b is that they illustrates how much the SRH recombination rates changes between $V = V_{OC}$ and $V = V_M$. This is relevant because both voltages are important for a real solar cell. $V = V_M$ is the voltage that produces the highest output power, and it is desirable that this is the voltage a power producing solar cells operates at. It can therefore be argued that the design principle should be investigated at this voltage. However, $V = V_{OC}$ is the voltage at which the SRH recombination is most dominant, and the design principle aims to reduce this recombination mechanism. It can thus be argued that the simulations should be conducted at this voltage. Until now in this thesis have all energy band diagrams and recombination rates been shown at V_{OC}. It would perhaps be best to plot all figures at several voltages, including $V = V_{OC}$ and $V = V_M$, but due to time limitations this cannot be done. In the rest of the thesis it is chosen to continue plotting the figures at the open-circuit voltage as the SRH mechanism is most dominant here. Another reason why this is chosen is because this is much more convenient to do in SCAPS, as this can be done directly from the simulation results. If one wants to plot the rates at $V = V_M$, one first needs to do one simulation, calculate V_M manually, and then redo the simulation stopping at the calculated V_M.
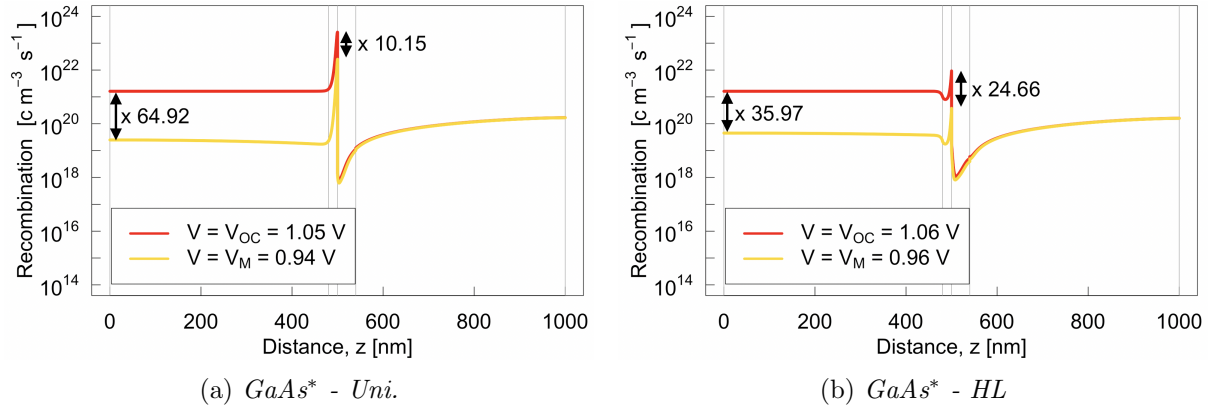
(a) *GaAs* - Uni.*

(b) *GaAs* - HL*

Figure 4.24: The SRH recombination rates for (a) the *GaAs* - Uni.* cell and (b) the *GaAs* - HL* cell. The red curves are plotted at $V = V_{\mathrm{OC}}$ while the yellow are plotted at $V = V_{\mathrm{M}}$. The vertical lines indicates the interfaces between the layers. Where the red curve cannot be seen it lays behind the yellow curve. The numbers in the figures indicates the scaling between the curves at the two voltages.

In their paper, Santhanam and Fan states that the design principle have a more substantial effect in lower performing cells where the SRH recombination is the dominant loss mechanism. In addition, the effect increases for decreasing voltages. The modified GaAs*/AlGaAs cells here benefited from the changes, but their performances were already very good. Therefore, the next step is to simulate worse performing cells and apply the design changes to them. There are several measures that can be taken to reduce a cell's performance. Initially, in the subsequent subsection, will this be achieved by reducing the incident light power. Then, in subsection 4.3.4, the incident light power is set back to the standard conditions, and the capture cross section and the impurity density of the defects are adjusted as this will make the SRH recombination more dominant.

4.3.3 Low Light Performance

This section aims to investigate how the performance of a cell with inhomogeneous doping concentration around the depletion region changes compared to homogeneous doped cell under low light conditions. To do this, the efficiency of the *GaAs* - Uni.* and *GaAs* - HL* cells are calculated at different incident powers. All previous simulations have been conducted under the AM1.5 global spectrum normalized to a P_{in} of 1000 Wm^{-2} as shown as the blue curve in Figure 4.25. The reduction in incident light power is achieved by reducing transmission factor in SCAPS, effectively scaling the AM1.5 global spectrum to give the desired value of P_{in}. The red curve in Figure 4.25 shows the incident light power at 50% transmission.
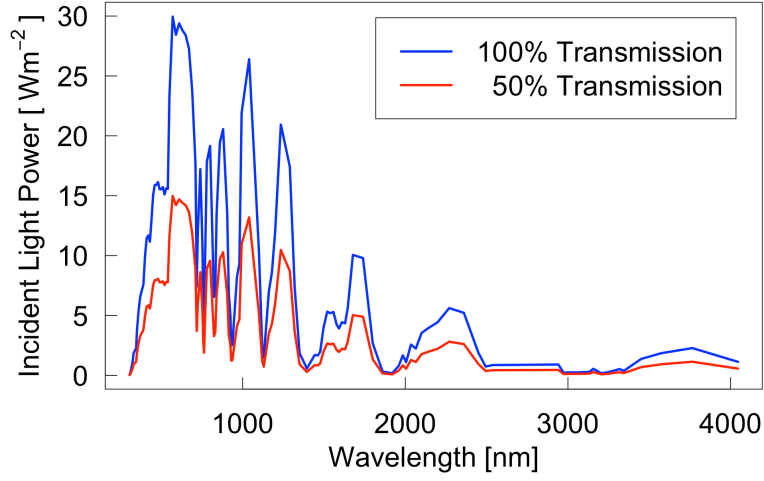
Figure 4.25: The AM1.5 global spectrum used in SCAPS [12]. The blue curve is shows the spectrum at 100% transmission and is normalized to a P_{in} of 1000 Wm^{-2}. The red curve shows the spectrum at 50% transmission.

Results

Efficiency

Figure 4.26a shows the efficiency of the $GaAs^* - Uni.$ and $GaAs^* - HL$ cells (black and red curves, respectively) calculated with the the first relation in Eq.(2.12) with $P_{in} = 1000$ Wm^{-2}. The result shows that the efficiency drops linearly width decreasing incident light power for both cells, and that the efficiency of the $GaAs^* - HL$ cell always is the highest. In Figure 4.26b, the black line shows the percentage efficiency increase $\Delta\eta_\%$ between the efficiencies of the $GaAs^* - Uni.$ cell $\eta_{Uni.}$ and the $GaAs^* - HL$ cell η_{HL} when the incident light power is reduced calculated by the following relation

$$\Delta\eta_\% = \frac{\eta_{HL} - \eta_{Uni.}}{\eta_{Uni.}} \cdot 100\% \tag{4.5}$$

The red line Figure 4.26b shows the absolute efficiency increase $\Delta\eta_{Abs.}$ between the same cells calculated by the following relation

$$\Delta\eta_{Abs.} = \eta_{HL} - \eta_{Uni.} \tag{4.6}$$

The result shows that the percentage efficiency increase is larger at lower incident light power, while the absolute efficiency increase is almost the same for all incident light power.
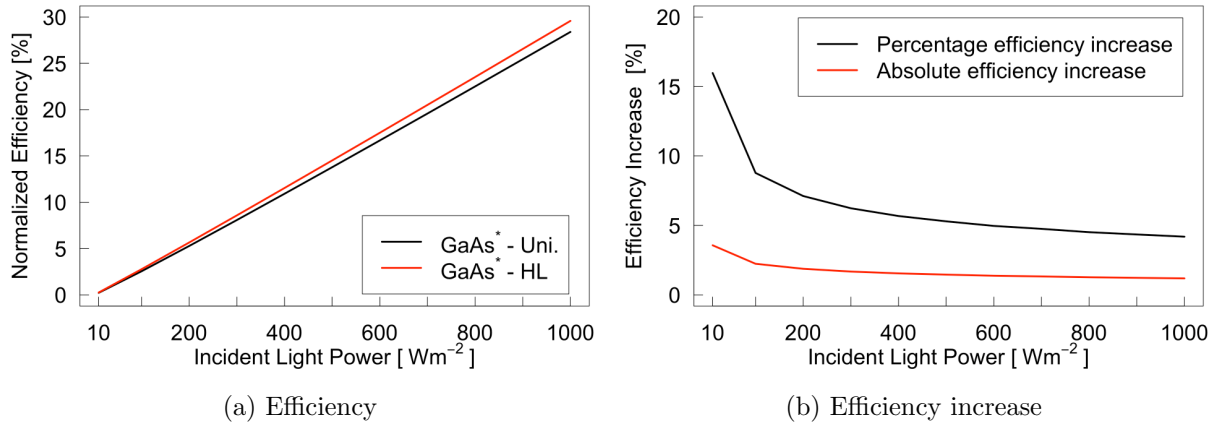
74

(a) Efficiency (b) Efficiency increase

Figure 4.26: (a) The efficiency normalized to a input power of 1000 Wm^{-2} when the incident light power is varied for the $GaAs^*$ - $Uni.$ and $GaAs^*$ - HL cells. (b) The increase in efficiency between the $GaAs^*$ - $Uni.$ and $GaAs^*$ - HL cells in percentage increase (black line) and absolute increase (red line) when the incident light power is reduced.

Discussion

As described in subsection 2.1.5, it is know that a solar cell open-circuit voltage V_{OC} changes to a new value V'_{OC} depending on the incident light power X in accordance with Eq.(2.11). As stated by Santhanam and Fan in Ref. [11], the design principle has a greater effect at lower voltages. Therefore, it could be that at a lower incident light power the effect of the principle could also be greater. If this is true, the design principle could increase the efficiency of cells in low light conditions, such as during high cloud concentration or in the morning/evening.

The results from Figure 4.26a showed that the inhomogeneously doped cell ($GaAs^*$ - HL) had a higher efficiency for all incident light powers. The mean difference between them is 1.71 ± 0.69 percentage points, with the maximum value at 10 Wm^{-2} being 3.57 percentage points and the minimum value at 1000 Wm^{-2} being 1.19 percentage points. This means that even though the $GaAs^*$ - HL cell performed best, the increase in efficiency at lower light is about the same, especially since both values of the efficiencies are low at low incident powers. This can also be seen from Figure 4.26b, where the red curve stays relatively flat. The reason for why the black curve increases more substantially is that at lower light power does the increase in efficiency result in a higher percentage increase as the absolute increase is about the same.

The results from this subsection shows that the principle does not contribute to a considerable increase in efficiency for under low light conditions. The performance is higher, but at low light conditions are the performances of both the $GaAs^*$ - $Uni.$ and $GaAs^*$ - HL cells low. A likely explanation to why it did not work is that the ratio between the generation and SRH recombination, the recombination mechanism aimed to reduce, stays relatively constant between the different light conditions, making the improvement constant. The conclusion is thus that the design principle will result in slightly better low light performance, but the increase is about the same as under standard conditions.

75

4.3.4 Low Efficiency Modified GaAs/AlGaAs Cells

In this subsection is the capture cross section (CCS) σ (which will be kept the same for electrons and holes) and the impurity density N_t first varied to create a low efficiency (LE) cell labelled the *GaAs* * *- LE* cell. Then, the design principle by Santhanam and Fan is applied to this cell, i.e. higher H doping concentration in layer 2 (p-type) and lower L doping concentration in layer 3 (n-type) (see Figure 3.4). In addition, both a cell with the reverse configuration and a cell with high-high configuration were also simulated. This resulted in three new cells labelled *GaAs* * *- LE, HL, GaAs* * *- LE, LH,* and *GaAs* * *- LE, HH.* Collectively are these four cells labelled the modified LE cells.

Results

Capture Cross Section and Impurity Density

The heat map in Figure 4.27 presents how the efficiency changes when the CCS and impurity density changes. The fully white squares indicates that the simulation program SCAPS was not able to calculate these cells due to conversion errors. In the figure, the values of the CCS and the impurity density for the *GaAs* * *- Uni.* and *GaAs* * *- LE* cells are marked by white and black boxes, respectively. For the *GaAs* * *- LE* cell, these values are $\sigma = 10^{-12}$ cm^2 and N_t $= 10^{16}$ cm^{-3}, and its efficiency is 3.29%. This is substantially lower than the efficiency of the *GaAs* * *- Uni.* cell (28.39%).
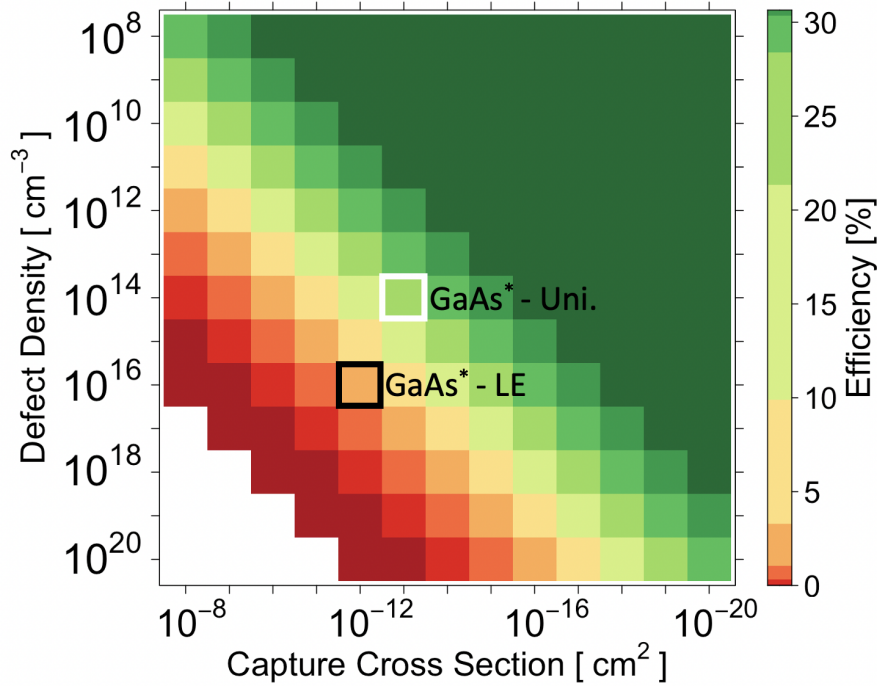

Figure 4.27: Heat map showing the efficiency when the capture cross section (CCS) is varied between 10^{-18} cm^2 and 10^{-20} cm^2 and the impurity density between 10^8 cm^{-3} and 10^{20} cm^{-3}. The filled white squares indicates *NA* values. The white and black boxes indicates the CCS and impurity density values for the *GaAs* * *- Uni.* and *GaAs* * *- LE* cells, respectively.

Performance Parameters and IV-curves

The performance parameter for the four modified LE cells are summarized in Table 4.13. Similarly to the modified high efficiency GaAs*/AlGaAs cells in subsection 4.3.2 did the efficiency of the inhomogeneous doped cell (*GaAs* - LE, HL*) increase with respect to the homogeneous doped cell (*GaAs* - LE*). This increase was 0.44 percentage points or 13.37%. In addition, the short circuit current density between these cells dropped from 6.68 mA/cm^2 to 5.26 mA/cm^2, while the open circuit voltage increased from 0.70 V to 0.89 V. The efficiency for both *GaAs* - LE, LH* and *GaAs* - LE, HH* droped with respect to the *GaAs* - LE* cell, where the High/High dropped most at 0.47 percentage points or 16.67%.

The IV-curves for the four modified LE cells are presented in Figure 4.28. As can be seen from the figure is the open-circuit voltage and the short-circuit current density for the *GaAs* - LE, HL* cell higher and lower, respectively, in comparison with the other three LE cells.

Table 4.13: Performance parameters for the *GaAs* - LE, GaAs* - LE, HL, GaAs* - LE, LH*, and *GaAs* - LE, HH* cells.

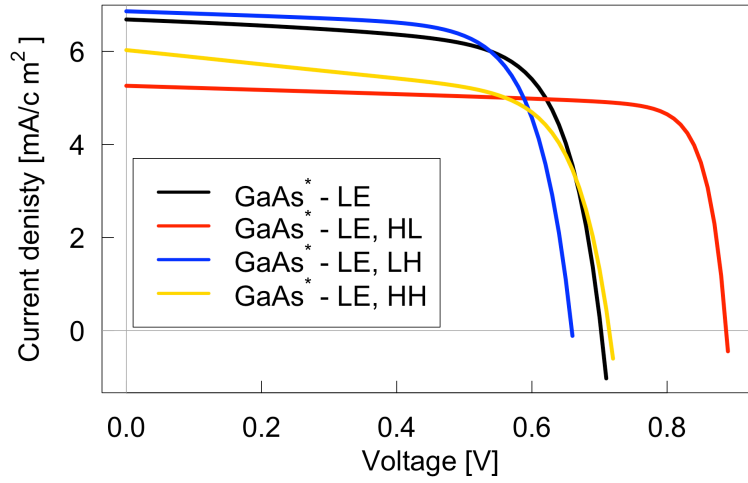|	η [%]	J_{SC} [mA/cm^2]	V_{OC} [V]	FF [%]
GaAs - LE*	3.29	6.68	0.70	70.13
GaAs - LE, HL*	3.73	5.26	0.89	79.79
GaAs - LE, LH*	3.23	6.86	0.66	71.50
GaAs - LE, HH*	2.82	6.03	0.71	65.69

Figure 4.28: IV-curves for the *GaAs* - Uni., GaAs* - HL, GaAs* - LH*, and *GaAs* - HH* cells.

Energy Band Diagrams

The energy band diagrams $V = V_{\text{OC}}$ for the $GaAs^*$ - LE, $GaAs^*$ - LE, HL, $GaAs^*$ - LE, LH, and $GaAs^*$ - LE, HH cells are shown in Figure 4.29a, Figure 4.29b, Figure 4.29c, and Figure 4.29d, respectively.
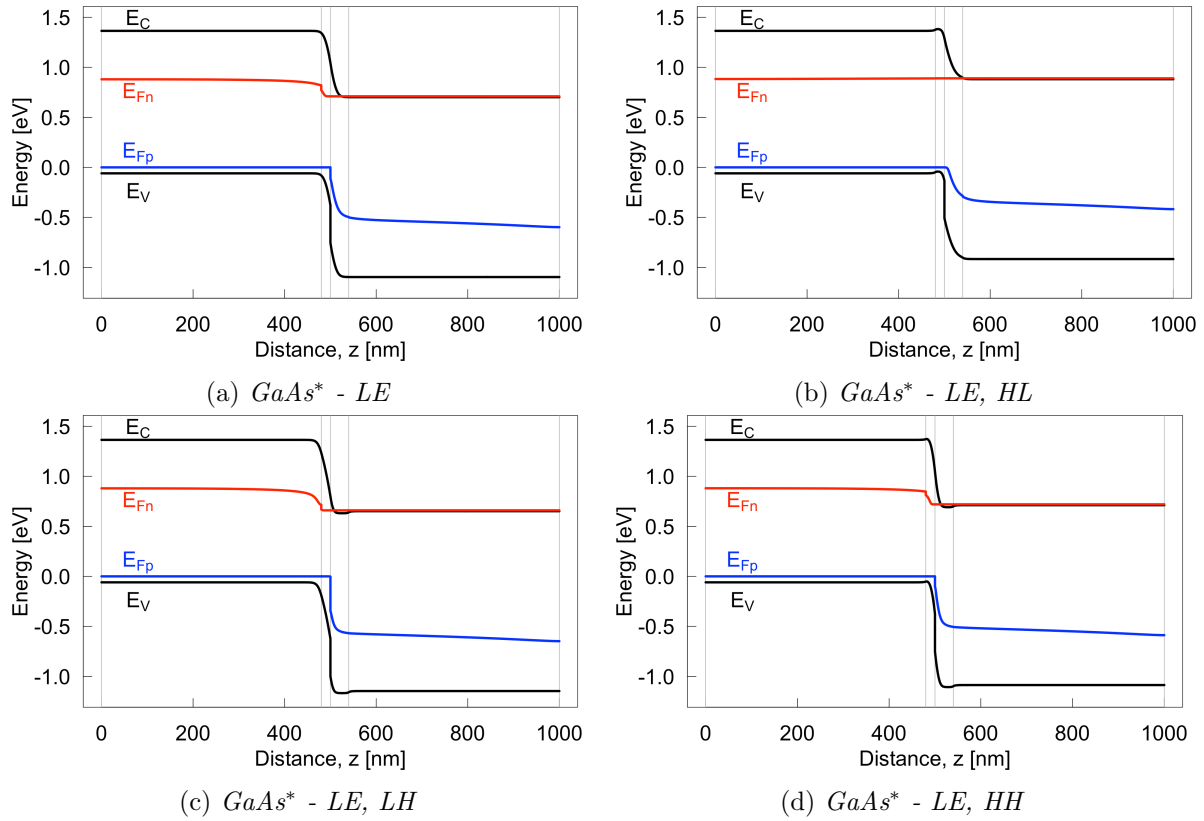

(a) $GaAs^*$ - LE

(b) $GaAs^*$ - LE, HL

(c) $GaAs^*$ - LE, LH

(d) $GaAs^*$ - LE, HH

Figure 4.29: The energy band diagrams $V = V_{\text{OC}}$ for (a) the $GaAs^*$ - LE cell, (b) the $GaAs^*$ - LE, HL cell, (c) the $GaAs^*$ - LE, LH cell, and (d) the $GaAs^*$ - LE, HH cell. The vertical lines indicates the interfaces between the layers.

Recombination Rates

The radiative and SRH recombination rates $V = V_{OC}$ for the entire cell and between $z = 460$ nm and $z = 560$ nm for the $GaAs^*$ - LE ce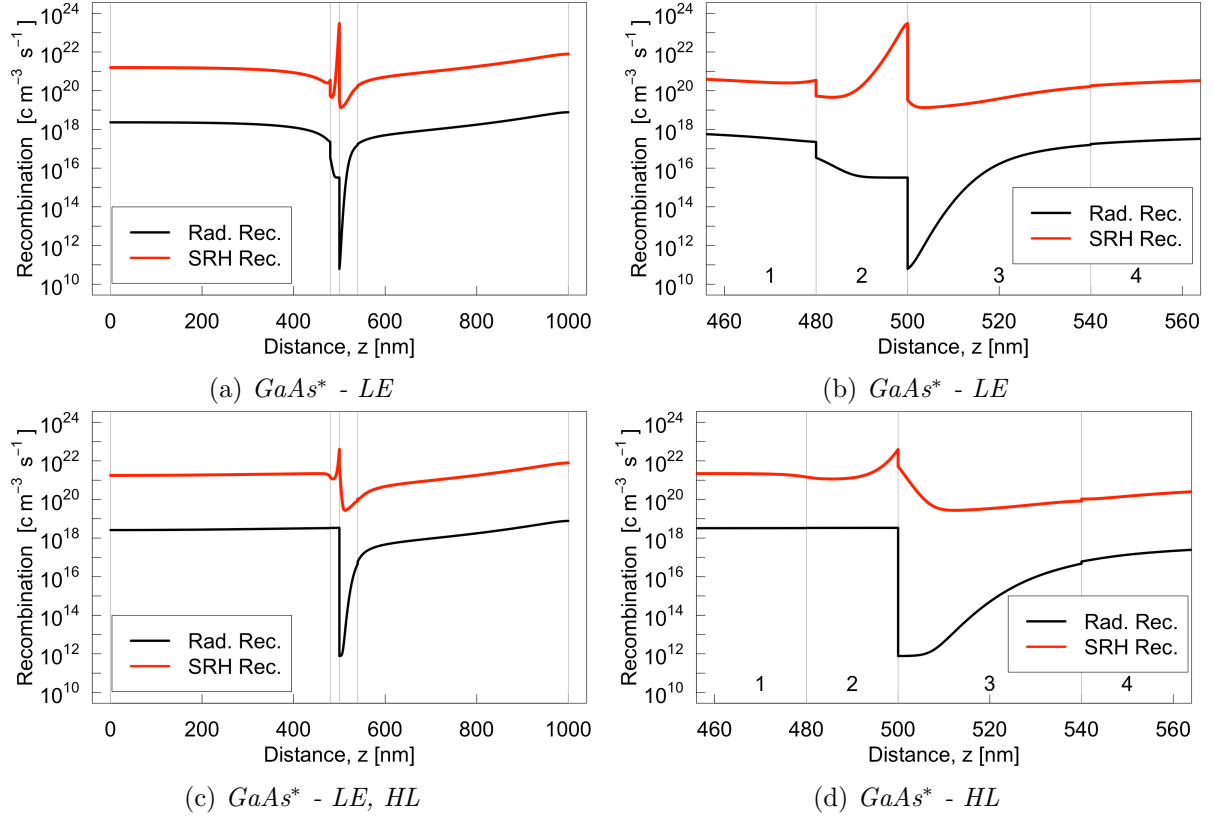ll are given in Figure 4.30a and Figure 4.30b, respectively. Next, the radiative and SRH recombination rates $V = V_{OC}$ for the entire cell and between $z = 460$ nm and $z = 560$ nm for the $GaAs^*$ - LE, HL cell are given in Figure 4.30c and Figure 4.30d, respectively.
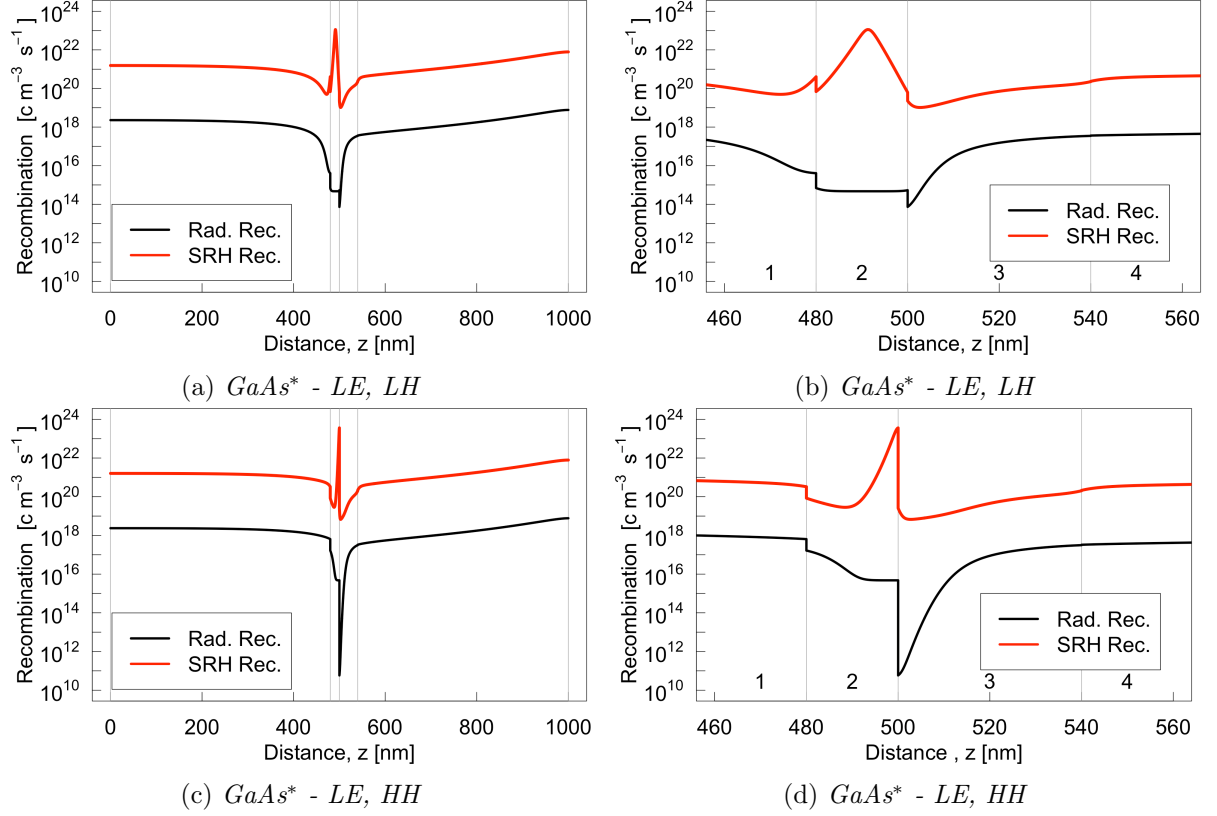

Figure 4.30: Radiative and SRH recombination rates at $V = V_{OC}$. (a) and (b) are the $GaAs^*$ - LE cell shown for the entire cell and between $z = 460$ nm to $z = 560$ nm, respectively. (c) and (d) are the $GaAs^*$ - LE, HL cell shown for the entire cell and between $z = 460$ nm to $z = 560$ nm, respectively. The numbers 1 to 4 in (b) and (d) indicates the layers in the cells. The vertical lines indicates the interfaces between the layers.

The radiative and SRH recombination rates $V = V_{\mathrm{OC}}$ for the entire cell and between $z = 460$ nm and $z = 560$ nm for the $GaAs^*$ - LE, LH cell are given in Figure 4.31a and Figure 4.31b, respectively. Next, the radiative and SRH recombination rates $V = V_{\mathrm{OC}}$ for the entire cell and between $z = 460$ nm and $z = 560$ nm for the $GaAs^*$ - LE, HH cell are given in Figure 4.31c and Figure 4.31d, respectively.

Figure 4.31: Radiative and SRH recombination rates at $V = V_{\mathrm{OC}}$. (a) and (b) are the $GaAs^*$ - LE, LH cell shown for the entire cell and between $z = 460$ nm to $z = 560$ nm, respectively. (c) and (d) are the $GaAs^*$ - LE, HH cell shown for the entire cell and between $z = 460$ nm to $z = 560$ nm, respectively. The numbers 1 to 4 in (b) and (d) indicates the layers in the cells. The vertical lines indicates the interfaces between the layers.

Discussion

The heat map in Figure 4.27 shows the effect on the efficiency when the CCS and the impurity density were varied. In general, a higher CCS resulted in a lower efficiency. The CCS of a defect in a semiconductor describes the effectiveness of the defects to capture a carriers and is a measure of how close the carriers needs to come to the defects to be captured. A higher CCS will thus result in more SRH recombination and a lower efficiency. For the impurity density, the trend is the same, i.e a higher densitiy results in lower efficiency. This is because when the density increases, there are more possible traps for the carriers, and thus the SRH recombination rate increases and the efficiency decreases. In fact is the SRH recombination rate proportional to both the CCS and the impurity density as described by Eq.(2.4). This is the reason why diagonal lines with the same efficiency appears in Figure 4.27. For example, the product of σ = 10^{-12} cm^2 and $N_{\mathrm{t}} = 10^{16}$ cm^{-3} is equal to the product of $\sigma = 10^{-10}$ cm^2 and $N_{\mathrm{t}} = 10^{14}$ cm^{-3}, and when the all other parameters are kept the same, will the SRH recombination be the same.

The cells with the darkest red color in Figure 4.27, e.g. $\sigma = 10^{-8}$ cm^2 and $N_t = 10^{16}$ cm^{-3}, had an efficiency of 0.00% when rounded to two decimals. The white squares in the figure indicates values SCAPS were not able to calculate. This is because the SRH recombination rates of these cells are so large that their efficiencies approaches zero and a conversion error occurs in the program. These missing cells are disregarded as they are not interesting in the context here. The cells with the darkest green color, e.g. $\sigma = 10^{-10}$ cm^2 and $N_t = 10^8$ cm^{-3}, all have an efficiency of 30.65%. This is the highest achievable efficiency of these cells when varying the CCS and the impurity density, and it is because the SRH recombination is minimized and other loss mechanisms dominates.

The values of the CCS and impurity density for the $GaAs^*$ - LE cell were chosen to be $\sigma = 10^{-12}$ cm^2 and $N_t = 10^{16}$ cm^{-3}, which resulted in an efficiency of 3.29%. These values were chosen as they are not too far from the original values (the CCS changes with a factor 10 and the impurity density with a factor 100), and the resulting efficiency was substantially lower while still not being too low. The value of the CCS is usually in the order of atomic dimensions, so the chosen value of 10^{-12} cm^2 is definitely on the lager side. The value of the impurity density can more easily be adjusted by introducing or removing impurities, and the chosen value of 10^{16} cm^{-3} is a obtainable. Nevertheless, the choice is somewhat arbitrarily and other cells in proximity to the chosen one could be used as the goal is to see how the design principle affects low efficiency cells. The important part is that these cell parameters stay constant throughout the simulations so that they affect the result equally.

The performance parameters in Table 4.13 showed that the cell where the design principle by Santhanam and Fan ($GaAs^*$ - LE, HL) was applied had the largest efficiency increase. The efficiency increase of 13.37% is substantially larger than the increase of 4.19% between the high efficiency $GaAs^*$ - $Uni.$ and $GaAs^*$ - HL cells from subsection 4.3.2. This corresponds well with Santhanam and Fan's results in Ref. [11], where they showed that the effect is greater for worse performing cells. This is due to the fact that the SRH recombination mechanism, i.e. the loss mechanism to be reduced, is more dominant in LE cells.

Another interesting aspect of the changes in performance parameters between $GaAs^*$ - LE and $GaAs^*$ - LE, HL is that the short-circuit current density decreases while the open-circuit voltage increases (as seen in Figure 4.28), and that this in total have a positive effect. The reason for the increased voltage is that when the doping is changed do the distance between the two quasi-Fermi levels also change. As explained by Eq.(2.5) does a larger difference between E_{Fn} and E_{Fp} result in a larger voltage. This happens between the $GaAs^*$ - LE cell and $GaAs^*$ - LE, HL cell, as can clearly be seen in their energy band diagram, Figure 4.29a and Figure 4.29b, respectively. A possible explanation to why the short-circuit current density decreases is that this quantity depends on the diffusion length of the carriers, which again depends on the carrier lifetime. These relations are described by Eq.(2.8) and Eq.(2.9), and from them one can see that a shorter lifetime result lower a short-circuit current density. Table 4.14 summarizes the lifetimes of the carriers in the GaAs* and AlGaAs layers for the $GaAs^*$ - HL and $GaAs^*$ - LE, HL cells. It can there be seen that the lifetimes of the LE cell is 1000 times smaller than for the high efficiency cell. Therefore, it is possible that in the $GaAs^*$ - LE, HL cell does the short lifetime of the carriers limit the J_{SC}.

Table 4.14: The electron and hole carrier lifetimes τ_n and τ_p, respectively, for the $GaAs^*$ - HL and $GaAs^*$ - LE, HL cells for the GaAs* and AlGaAs layers.

	GaAs*		AlGaAs	
	τ_n [ns]	τ_p [ns]	τ_n [ns]	τ_p [ns]
$GaAs^*$ - HL	2.3	5.6	2.7	6.1
$GaAs^*$ - LE, HL	0.023	0.056	0.027	0.061

All recombination rates curves for the LE cells are less smooth than the same curves for the high efficiency modified GaAs/AlGaAs cells from subsection 4.3.2. This is likely due to the fact that the SRH recombination is more dominant in the LE cells and they are thus more sensitive to the changes in the doping concentrations. Comparing the SRH recombination rates for the $GaAs^*$ - LE and $GaAs^*$ - LE, HL cells (Figure 4.30a and Figure 4.30c, respectively), one can clearly see that the peak in the p-n interface at $z = 500$ nm drops substantially for the latter. It droops with a factor 7.57 from from $2.97 \cdot 10^{23}$ cm^{-3}s^{-1} to $3.92 \cdot 10^{22}$ cm^{-3}s^{-1}. This drop is smaller than the drop between the $GaAs^*$ - $Uni.$ and $GaAs^*$ - HL cells, which dropped with a factor 27.8 (from $2.57 \cdot 10^{23}$ cm^{-3}s^{-1} to $9.22 \cdot 10^{21}$ cm^{-3}s^{-1}). This is counterintuitive when comparing the *percentage* efficiency increase between the homogeneously doped cells and the cells with the HL configuration, as the increase was 13.37% for the LE cells and only 4.19% for the high efficiency cells. However, the increase in percentage points is only 0.44% for the LE cells while it is 1.19% for the high efficiency cells. This shows than one needs to be precise when quantifying the improvement due to the design principle. The absolute increase in efficiency is the most important aspect, as this is what tells the performance of the cell. The result here showed that this increase is larger for the high efficiency cell. This does not contradict the results to Santhanam and Fan in Ref. [11], as they focused on percentage increase.

In general, the results here corresponded well with the results by Santhanam and Fan. Lower efficiency cells with higher SRH recombination have a higher positive percentage effect of the design principle. However, the it might be possible to gain a larger absolute efficiency increase by optimizing the layer thicknesses, as they until now only have been directly copied from the GaInAsP/InP cells by Santhanam and Fan. Therefore, the next step will be to keep the total cell thickness constant while varying the relative thicknesses of the layers.

4.3.5 Layer Thickness Variation

This subsection aims to find out the optimum thicknesses of the four layers (see Figure 3.4) in the LE modified GaAs/AlGaAs cells. This is done while keeping the whole cell thickness constant at 1000 nm, and doping concentrations of $9.0 \cdot 10^{17}$ cm^{-3} in layers 1 (p-type) and 4 (n-type), $4.0 \cdot 10^{17}$ cm^{-3} in layer 2 (p-type), and $2.0 \cdot 10^{18}$ cm^{-3} in layer 3 (n-type). Firstly, the thicknesses of layers 2 and 3 were varied between 0 nm and 80 nm with a 5 nm increment. Next, the same was done but between 0 nm and 10 nm with a 1 nm increment. Finally, this was done between 0 nm and 15 nm for the second GaAs*-layer and between 0 nm and 130 nm for the first AlGaAs-layer with a 5 nm increment.

Results

Efficiency

The heat map in Figure 4.32 shows the effect on the efficiency when the layer thicknesses were varied. The highest efficiency was found to be 4.52% when the second GaAs*-layer was 5 nm and the first AlGaAs-layer was between 70 and 80 nm. The lowest efficiency was found to be 3.43% when the same layers were 0 nm, i.e. removed. The white box in the figure shows the configuration for the $GaAs^*$ - LE, HL cell. The blue box shows the area of the upcoming Figure 4.33 and the black box parts of the area of the upcoming Figure 4.34. The three grey boxes are cell that are elaborated on in the discussion and in Figure 4.35.

The heat map in Figure 4.33 again shows the effect on the efficiency when the layer thicknesses were varied, only in this figure the layers are varied between 0 and 10 nm with 1 nm increment. The highest efficiency was found to be 4.39% when the second GaAs*-layer was 5 nm and the first AlGaAs-layer was 10 nm.
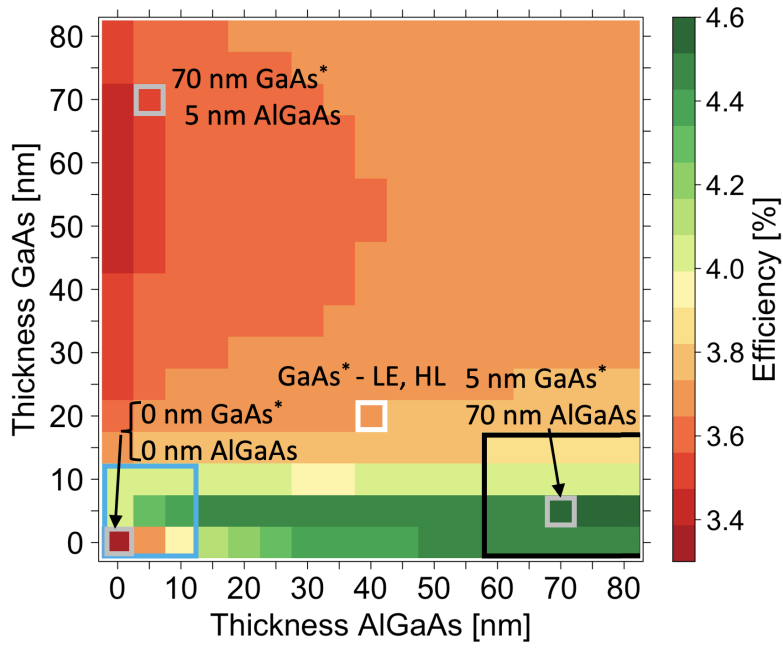
Figure 4.32: Effect on the efficiency when the layer thicknesses of layers 2 and 3 (see Figure 3.4) are varied from 0 to 80 nm with 5 nm increment in the *GaAs* - *LE, HL* cell. The white box is the original *GaAs* - *LE, HL* cell, the blue box is Figure 4.33, and the black box is parts of Figure 4.34. The three grey boxes are cell that are elaborated on in the discussion and in Figure 4.35.
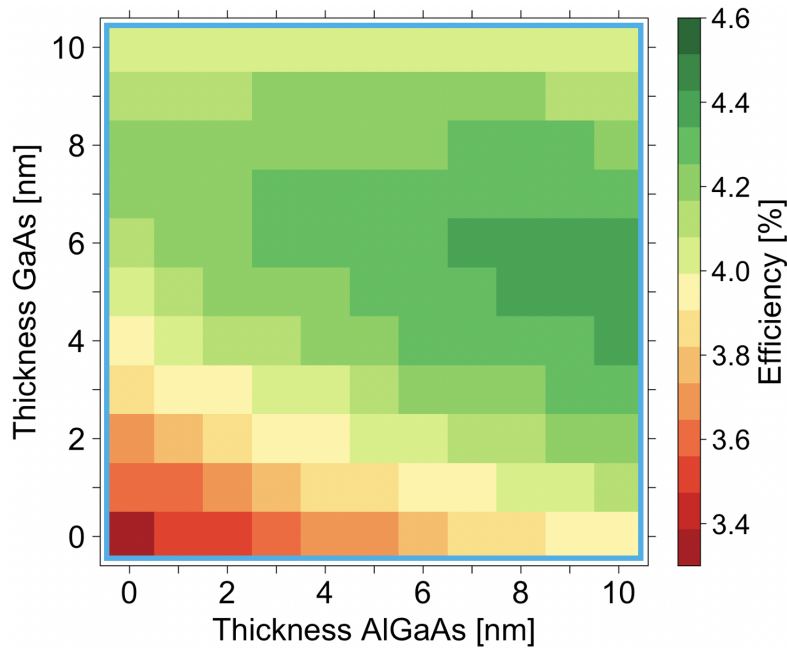

Figure 4.33: Effect on the efficiency when the layer thicknesses of layers 2 and 3 (see Figure 3.4) are varied from 0 to 10 nm with 1 nm increment in the *GaAs* - *LE, HL* cell.

The heat map in Figure 4.34 shows the effect on the efficiency when the second GaAs* layer was varied between 0 and 15 nm and the first AlGaAs layer was varied between 60 and 130 nm, both with with 5 nm increment. The highest efficiency was found to be 4.52% when the first GaAs*-layer was 5 nm and the second AlGaAs-layer was between 70 and 100 nm.
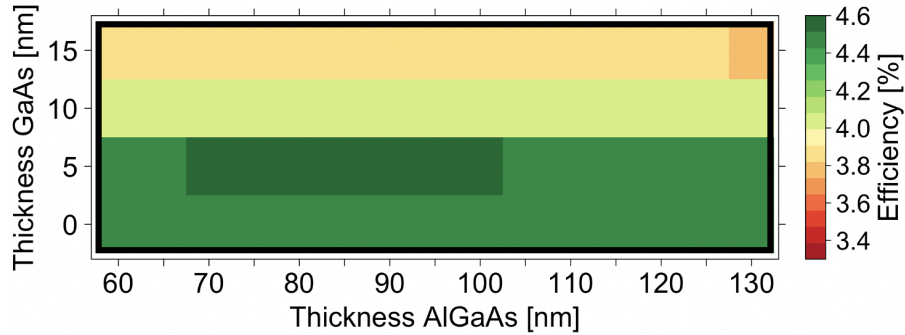

Figure 4.34: Effect on the efficiency when the second GaAs* layer thickness is varied between 0 and 15 nm and the first AlGaAs layer thickness (see Figure 3.4) is varied between 60 and 130 nm (5 nm increment) in the *GaAs* - LE, HL* cell.

Discussion

The results in this section showed that for the previous simulated *GaAs* - LE, HL* cell there exists better configurations of the layer thicknesses then what was used. This is not surprising as the original thicknesses where taken from the p-GaInAsP/n-InP cells from the simulations by Santhanam and Fan, which are not optimized for the materials used here. However, in their paper they do not give any reasoning for the used thicknesses, and a useful results would be to understand how the effect of the design principle changes with varying thicknesses of the layers. The four layers in the *GaAs* - LE, HL* cell (see Figure 3.4) were 480 nm, 20 nm, 40 nm, and 460 nm, and its efficiency was 3.73%. The optimum configuration was found to be 495 nm, 5 nm, 70-100 nm, and 430-400 nm for layers 1, 2, 3, and, 4, respectively, which can be seen in both Figure 4.32 and Figure 4.34. The efficiency was then found to be 4.52%. The cell with only the two outer layers at 500 nm had an efficiency of 3.43%. This means that the when including the inhomogeneous doping concentration in this cell the efficiency can increase by as much as 31.78%.

The results indicates that the thickness of the low doping concentration layer in the n-type material must be substantially larger than the thickness of the high doping concentration layer in the p-type material to reach the maximum efficiency. Figure 4.35 shows the SRH recombination rates at $V = V_{OC}$ between $z = 350$ nm and $z = 650$ nm for three cells where the second layer of GaAs* and first layer of AlGaAs are 0 nm x 0 nm, 70 nm x 5 nm, and 5 nm x 70 nm, respectively. The results shows that the cell with a 5 nm GaAs* layer and a 70 nm AlGaAs layer has the lowest SRH recombination peak. It suggests that this configuration best moves the depletion region into the wide bandgap material. A even larger AlGaAs layer would move the depletion region further to the left, and one could expect that this would increase the efficiency even more. However, then a too large portion of the cell will have a decreased doping concentration, which negatively effects the voltage and thus the efficiency.

Another interesting aspect of Figure 4.35 is that visually does the yellow curve appear to in total be substantially lower than the other curves. The same is true for the blue curve (70 nm x 5 nm) compared to the red curve (5 nm x 70 nm). This is initially surprising as the red curve corresponds to the best cell ($\eta = 4.52\%$), the blue to the second best ($\eta = 3.55\%$), and yellow to the worst ($\eta = 3.43\%$), and one would expect that the best cell has the lowest SRH recombination. However, this is exactly what is happening. Due to the fact that the SRH

recombination rate is plotted on a logarithmic scale does the peak value contribute much more than the lower bulk value. Table 4.15 summarized the layer thicknesses of the thin layers of GaAs* and AlGaAs of the thee cells in Figure 4.35, and their corresponding efficiency and total SRH recombination. It can there be seen that indeed the cell with the highest efficiency has the lowest total recombination rate.
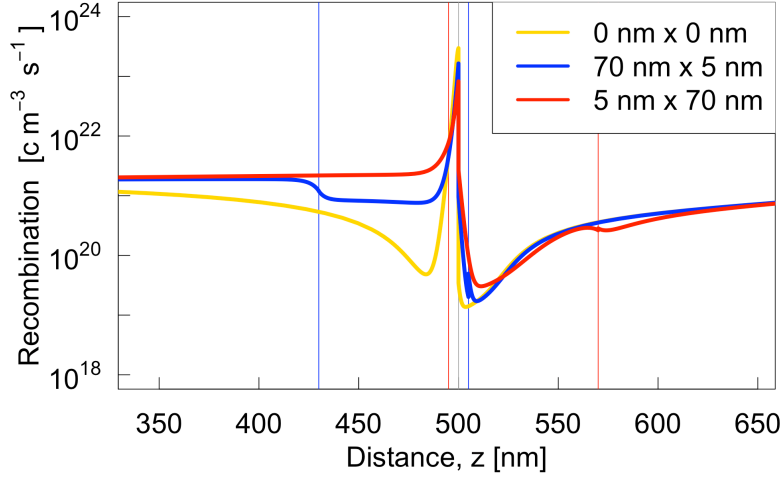

Figure 4.35: The SRH recombination rates at $V = V_{OC}$ between $z = 350$ nm and $z = 650$ nm for three low efficiency GaAs*/AlGaAs cells. The numbers indicate the thicknesses of the thin layers of GaAs* and AlGaAs at the p-n interface at $z = 500$ nm, e.g. the blue line with 70 nm x 5 nm have a 70 nm thick second GaAs* layer and a 5 nm first AlGaAs layer. The three configurations are also marked by grey boxes in Figure 4.32. Where the yellow curve cannot be seen it lays behind the blue curve. The vertical lines indicates the interfaces between the layers corresponding to the curve of the same color.

Table 4.15: The thicknesses of the thin layers of GaAs* and AlGaAs in three cells, and their corresponding efficiency and total SRH recombination. It can be seen from the table that the efficiency increases with decreasing total SRH recombination.

Thickness GaAs*	Thickness AlGaAs	Efficiency	Total SRH Recombination
0 nm	0 nm	3.43%	$3.63 \cdot 10^{24}$ cm^{-3}s^{-1}
70 nm	5 nm	3.55%	$2.13 \cdot 10^{24}$ cm^{-3}s^{-1}
5 nm	70 nm	4.52%	$2.06 \cdot 10^{24}$ cm^{-3}s^{-1}

The results from Figure 4.33 shows that even very thin layers with inhomogeneous doping concentration can result in a substantial increase in the efficiency. This is because even a slightly unbalance in doping in enough to move the peak value of the SRH recombination into the wide bandgap material causing the SRH recombination to decrease. However, if one where to produce real versions of the cells simulated here (disregarding the fact that this is not possible due to the modified value of GaAs's electron affinity) it would be no significant difference in producing the thin layers to be 5 nm x 5 nm than the optimum at 5 nm x 70 nm. It is therefore no reason not to produce the optimum configuration, and the thin layers in Figure 4.33 is not discussed any further.

An important notice for all the results in this subsection is that the findings only holds for the exact cell simulated here. There is thus no way to argue that 5 nm x 70 nm is the optimum configuration for another cell. Instead, the conclusion from these result is that before making a cell with the design principle by Santhanam and Fan, similar simulations to the ones that have been conducted here most be repeated so that the best configuration is found. In addition, it should be noted that similar result could be obtained by instead of varying the layer thicknesses,

the layer doping concentrations could be varied. Figure 4.36 schematically illustrates that the layer thicknesses variation gives the same effect as a variation of the doping concentration. It could be that varying the layer thicknesses are in practice more easily achieved, especially if the optimum doping configuration at a set thickness is very high. However, this is beyond the scope of this thesis and thus not discussed any further.
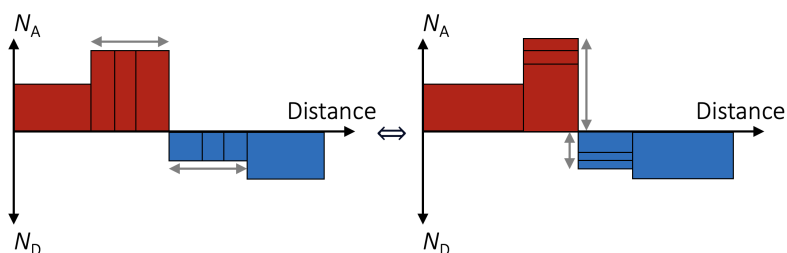

Figure 4.36: Schematic illustration showing that varying the thicknesses of the inhomogeneously doped layers results in the same as changing the doping concentrations of the same layers.

During the simulations presented in Figure 4.32, an unexpected result was discovered. The cell with zero thickness in both layers, i.e. only consisting of two layers of thicknesses 500 nm, had an efficiency of 3.43%. This cell is now labelled $GaAs^*$ - $2L$, where $2L$ indicates two layers. The doping concentrations in this cell is $N_A = N_D = 9.0 \cdot 10^{17}$ cm^{-3}. A previous simulated cell, the $GaAs^*$ - LE cell, consistes of four layers of thicknesses 480 nm, 20 nm, 40 nm, and 460 nm, and has the same doping concentrations at $N_A = N_D = 9.0 \cdot 10^{17}$ cm^{-3}. The materials, number of layers, layer thicknesses, and doping concentrations of the $GaAs^*$ - LE cell and the $GaAs^*$ - $2L$ cell are schematically illustrated in Figure 4.37a and Figure 4.37b, respectively. However, the unexpected result is that the efficiency of the $GaAs^*$ - LE cell was found to be 3.29%, i.e. not the same as for the $GaAs^*$ - $2L$ cell. In fact, they differ by 0.14 percentage points or 4.26%. In theory these cells should have the exact same performance, but clearly something different happens in the simulation program. This can potentially adding a non-insignificant amount of uncertainty to all previous simulations, as the efficiency changes due to a splitting of the layers alone (in contrast to when the layers are spitted and changed in terms of the doping conentrations). This phenomena is investigated further in the subsequent section, and no suggestion to the cause of this is thus not presented at this point.

The next section aims to repeat the design principle in GaAs homojunctions. If this works it has the benefit of removing the need for modified GaAs, but it is expected to not work as the intrinsic carrier concentration is the same in all layers. Additionally, the next section will also be used to investigate further how the simulated cell efficiencies varies depending on the number and thicknesses of the layers in the cell.
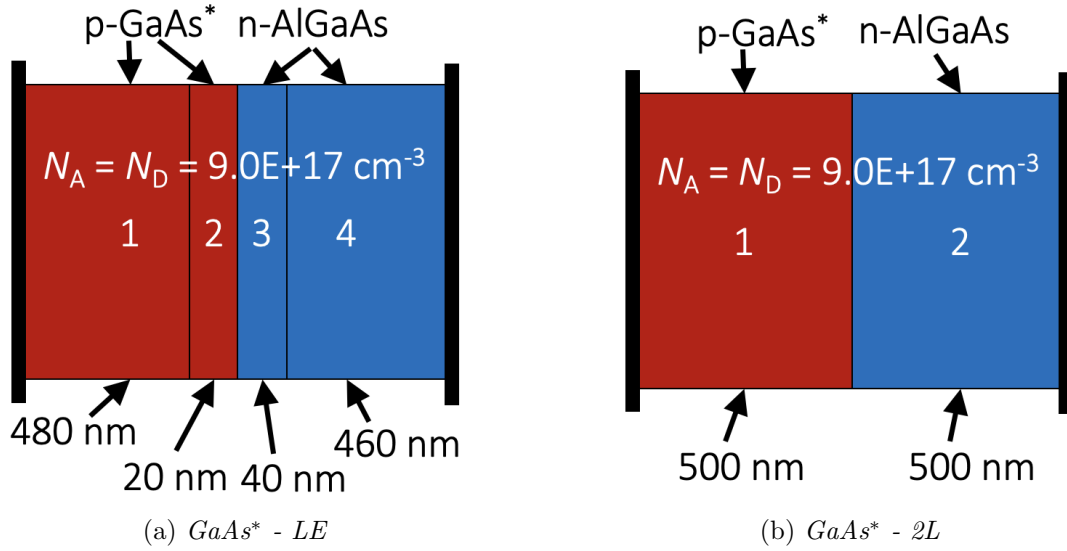
Figure 4.37: The materials, number of layers, layer thicknesses, and doping concentrations of (a) the *GaAs* - LE* cell and (b) the *GaAs* - 2L* cell. The efficiency of the *GaAs* - LE* cell is 3.29% and the efficiency of the *GaAs* - 2L* cell is 3.43%.

4.4 GaAs Homojunction Cells

This section is divided into two parts. First, in subsection 4.4.1, the design principle by Santhanam and Fan, i.e. higher doping concentration in the p-layer and lower doping concentration in the n-layer in proximity to the p-n interface, is applied to a GaAs homojunctions (HJ) cell (HJ can be a confusing abbreviation as it could also mean *heterojunction*, but is exclusively used for homojunctions in this thesis). This resulted in two cells labelled *GaAs, HJ - Uni.* and *GaAs, HJ - HL*, where the design changes have been applied to the latter. Then, the reverse configuration (i.e. low/high) and a high/high configuration was applied, which resulted in two cells labelled *GaAs, HJ - LH* and *GaAs, HJ - HH*. Then, in subsection 4.4.2, the effect of varying numbers and thicknesses of layers has on the simulated efficiency in SCAPS is investigated further. This was done by simulation five HJ cells with different structures labelled *GaAs, HJ - 1, GaAs, HJ - 2, GaAs, HJ - 3, GaAs, HJ - 4*, and *GaAs, HJ - 5*.

4.4.1 Varied Doping Concentrations in Homojunctions

The four initial GaAs homojunctions cells were simulated with different doping concentrations in the middle two layers (see Figure 3.5). The *high* doping was set to be $2 \cdot 10^{18}$ cm^{-3}, the middle to be $9 \cdot 10^{17}$ cm^{-3}, and the *low* to be $4 \cdot 10^{17}$ cm^{-3}.

Results

Performance Parameters and IV-curves

The performance parameters for the *GaAs, HJ - Uni., GaAs, HJ - HL, GaAs, HJ - LH*, and *GaAs, HJ - HH* cells are summarized in Table 4.16. The performance parameters shows a drop in efficiency from the homogeneously doped cell to all inhomogeneously doped cells. This drop is biggest for the *GaAs, HJ - HH* cell at 0.32 percentage points or 19.39%.

The IV-curves for the four homojunction GaAs cells are show in Figure 4.38.

Table 4.16: Performance parameters for the *GaAs, HJ - Uni.*, *GaAs, HJ - HL*, *GaAs, HJ - LH*, and *GaAs, HJ - HH* cells.

	η [%]	J_{SC} [mA/cm^2]	V_{OC} [V]	FF [%]
GaAs, HJ - Uni.	1.97	4.43	0.65	68.92
GaAs, HJ - HL	1.82	4.20	0.63	69.25
GaAs, HJ - LH	1.79	4.00	0.63	70.54
GaAs, HJ - HH	1.65	3.81	0.66	65.88
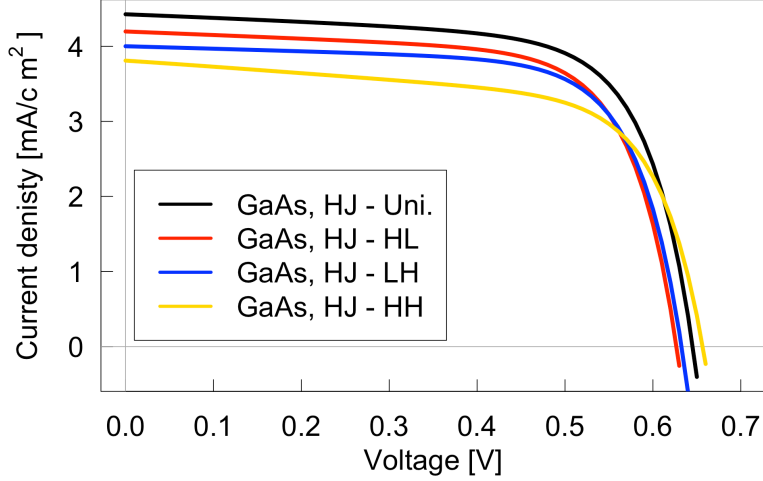
Figure 4.38: IV-curves for the *GaAs, HJ - Uni.*, *GaAs, HJ - HL*, *GaAs, HJ - LH*, and *GaAs, HJ - HH* cells.

Energy Band Diagrams

The energy band diagrams at $V = V_{\text{OC}}$ for the *GaAs, HJ - Uni.*, *GaAs, HJ - HL*, *GaAs, HJ - LH*, and *GaAs, HJ - HH* cells are shown in Figure 4.39a, Figure 4.39b, Figure 4.39c, and Figure 4.39d, respectively.

Recombination Rates

The radiative and SRH recombination rates $V = V_{\text{OC}}$ for the entire cell and between $z = 460$ nm and $z = 560$ nm for the *GaAs, HJ - Uni.* cell are given in Figure 4.40a and Figure 4.40b, respectively. Next, the radiative and SRH recombination rates $V = V_{\text{OC}}$ for the entire cell and between $z = 460$ nm and $z = 560$ nm for the *GaAs, HJ - HL* cell are given in Figure 4.40c and Figure 4.40d, respectively.

The radiative and SRH recombination rates $V = V_{\text{OC}}$ for the entire cell and between $z = 460$ nm and $z = 560$ nm for the *GaAs, HJ - LH* cell are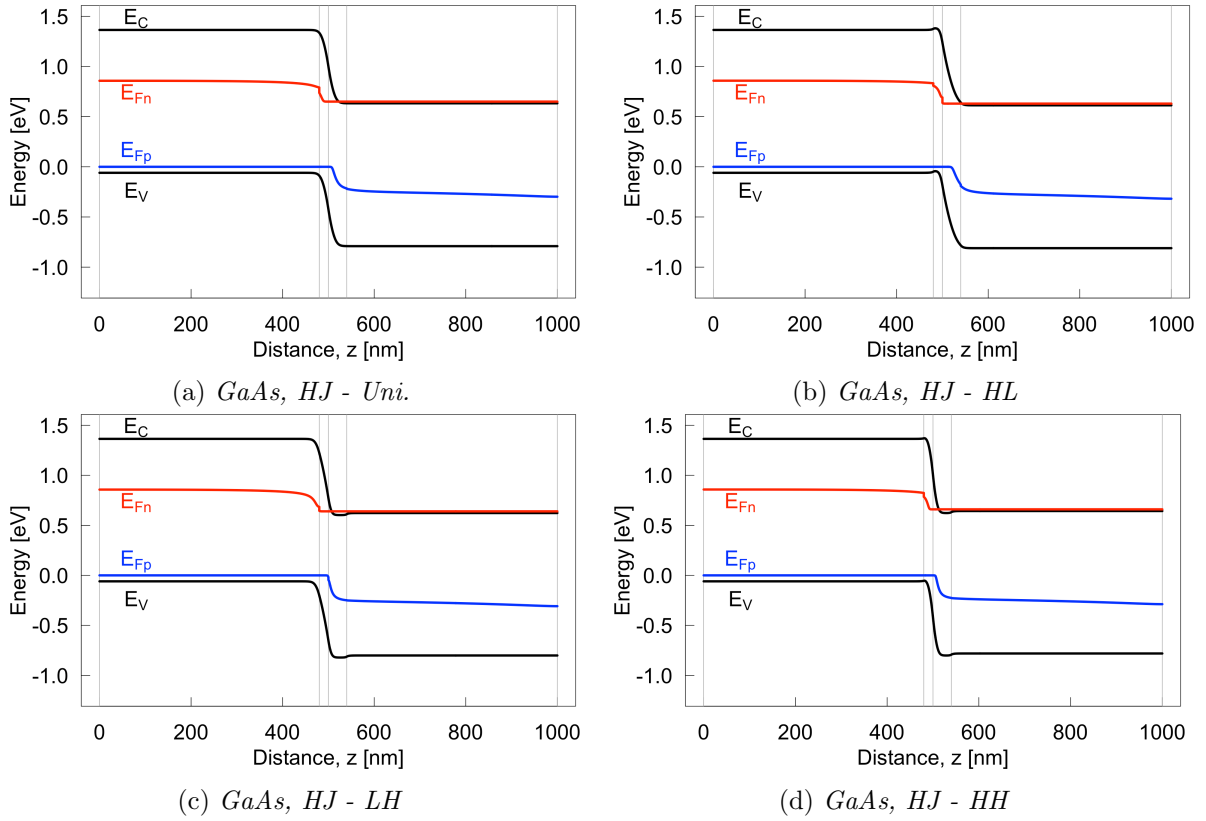 given in Figure 4.41a and Figure 4.41b, respectively. Next, the radiative and SRH recombination rates $V = V_{\text{OC}}$ for the entire cell and between $z = 460$ nm and $z = 560$ nm for the *GaAs, HJ - HH* cell are given in Figure 4.41c and Figure 4.41d, respectively.

Figure 4.39: The energy band diagrams at $V = V_{\text{OC}}$ for (a) the *GaAs, HJ - Uni.* cell, (b) the *GaAs, HJ - HL* cell, (c) the *GaAs, HJ - LH* cell, and (d) the *GaAs, HJ - HH* cell. The vertical lines indicates the interfaces between the layers.
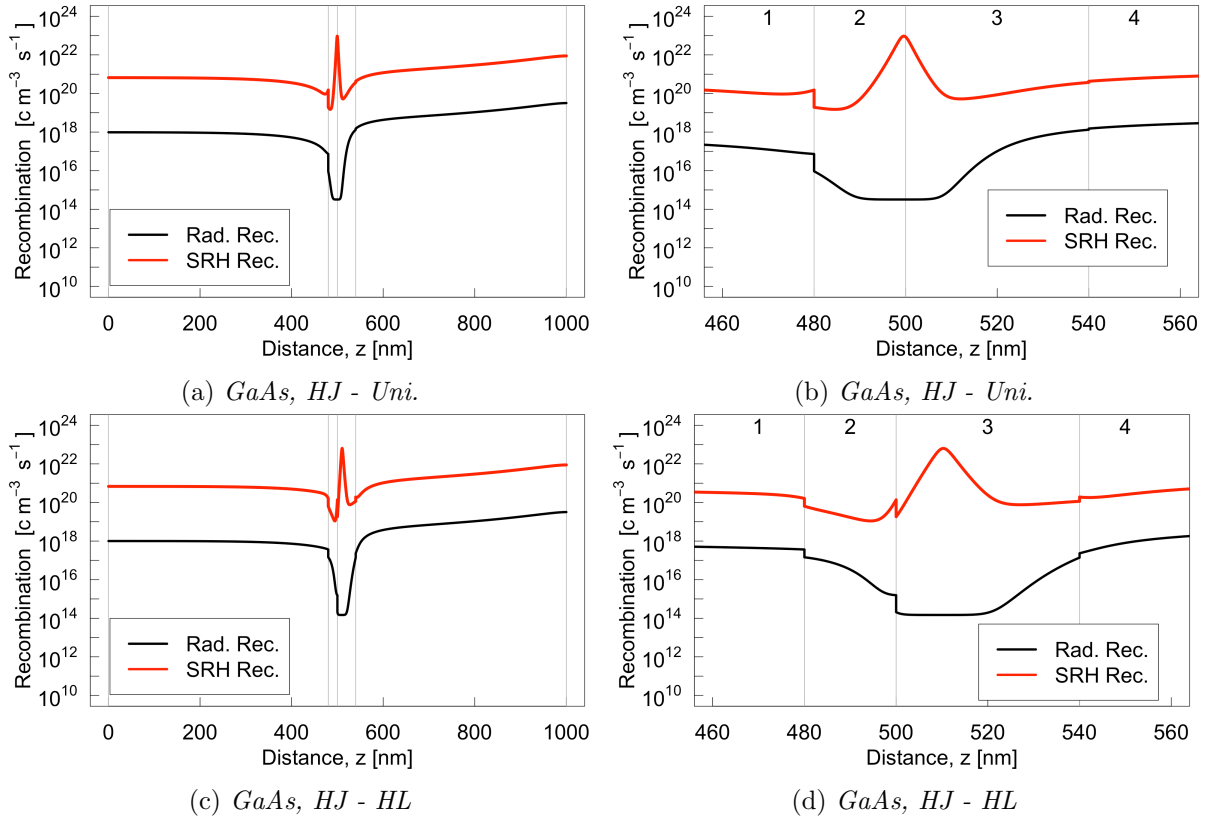
(a) *GaAs, HJ - Uni.*

(b) *GaAs, HJ - Uni.*

(c) *GaAs, HJ - HL*

(d) *GaAs, HJ - HL*

Figure 4.40: Radiative and SRH recombination rates at $V = V_{\text{OC}}$. (a) and (b) are the *GaAs, HJ - Uni.* cell shown for the entire cell and between $z = 460$ nm to $z = 560$ nm, respectively. (c) and (d) are the *GaAs, HJ - HL* cell shown for the entire cell and between $z = 460$ nm to $z = 560$ nm, respectively. The numbers 1 to 4 in (b) and (d) indicates the layers in the cells. The vertical lines indicates the interfaces between the layers.
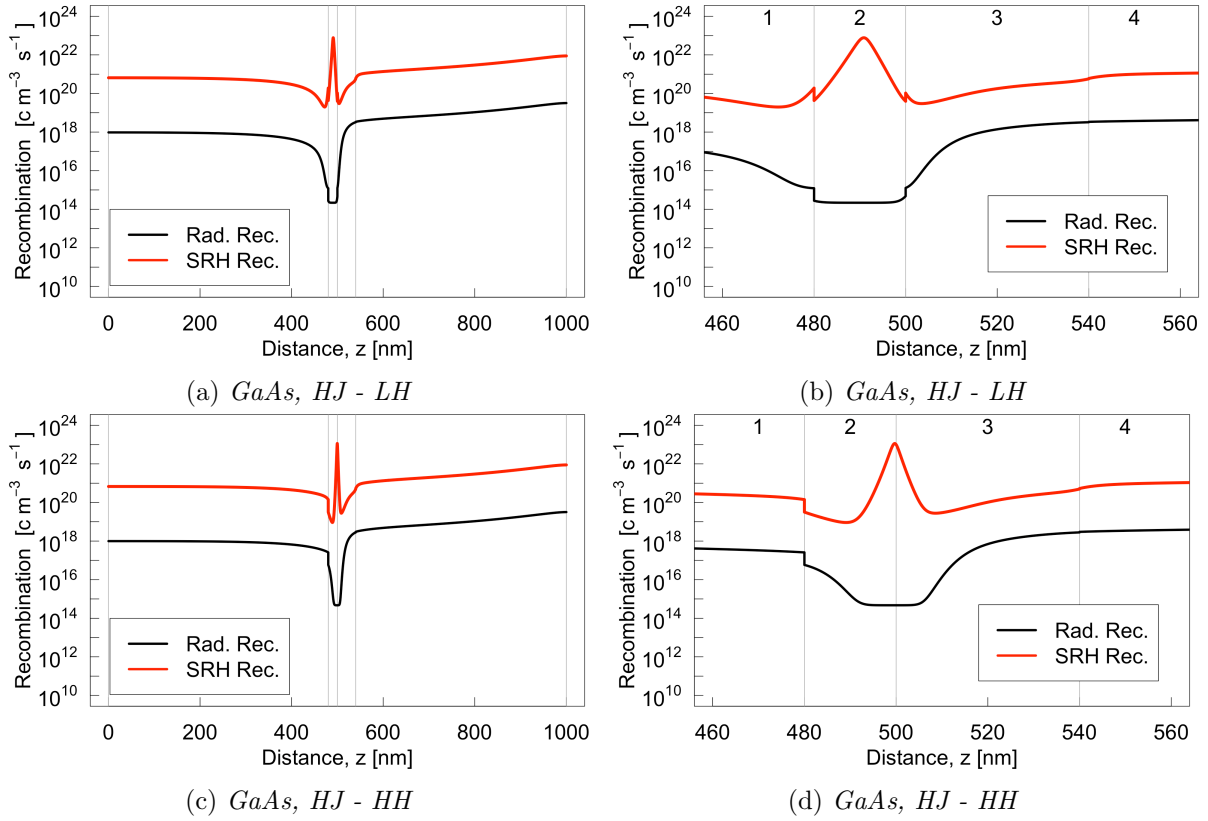
(a) *GaAs, HJ - LH*

(b) *GaAs, HJ - LH*

(c) *GaAs, HJ - HH*

(d) *GaAs, HJ - HH*

Figure 4.41: Radiative and SRH recombination rates at $V = V_{\mathrm{OC}}$. (a) and (b) are the *GaAs, HJ - LH* cell shown for the entire cell and between $z = 460$ nm to $z = 560$ nm, respectively. (c) and (d) are the *GaAs, HJ - HH* cell shown for the entire cell and between $z = 460$ nm to $z = 560$ nm, respectively. The numbers 1 to 4 in (b) and (d) indicates the layers in the cells. The vertical lines indicates the interfaces between the layers.

Discussion

In contrast to every other previous simulated cells in this thesis were the cells in this section homojunctions instead of heterojunctions. This change resulted in a switch from a positive impact to a negative impact when the design principle by Santhanam and Fan was applied. Comparing the recombination rates of the *GaAs, HJ - Uni.* cell and the *GaAs, HJ - HL* cell (Figure 4.40b and Figure 4.40d, respectively), one can clearly see that the peak has moved from the middle of the junction at $z = 500$ nm to the n-type GaAs at $z \approx 515$ nm. Similarly, the peak is moved to the p-type GaAs at $z \approx 490$ nm in the *GaAs, HJ - LH* cell (Figure 4.41b) and have stayed stationary at $z = 500$ nm in the *GaAs, HJ - HH* cell (Figure 4.41d). This happens because the change in doping concentration changes the position of the depletion region in the junction, and the peak value of the SRH recombination rate follows the position of the depletion region. This is also what one wants to achieve if one is to utilize the design principle. However, this is not enough alone, and the missing part is that the intrinsic carrier concentration is equal in every the layer. As the SRH recombination rate is proportional to the intrinsic carrier concentration, the peak value thus stays the same in all homojunction cells regardless of the position of the peak. To summarize, a inhomogeneous doping concentrating around the p-n interface in a heterojunction results in both a shift and a reduction of the peak SRH recombination rate, while the peak value in a homojunction only is shifted. The conclusion is thus that homojunctions are not applicable for the design principle.

It seems contradictory that the SRH recombination peak only is shifted and not reduced in the inhomogeneously doped cells while at the same time do the performance parameters in Table 4.16 show that the efficiency of those cells are reduced. It could be that the *total* SRH recombination rate is higher in the inhomogeneously doped cells, but as can be seen in Table 4.17, this rate is largest for the most efficient cell (*GaAs, HJ - Uni.*). In addition, there are no definite trend between the efficiency and total SRH recombination found in theses cells. It could then be that the radiative (band-to-band) recombination rates increases due to the higher doping, which is true for the *GaAs, HJ - LH* and *GaAs, HJ - HH* cells. However, as the values are both not far from the value for the *GaAs, HJ - Uni.* cell and much smaller than the SRH recombination rates, is this likely not the reason. The cause of the efficiency drop is therefore some other effect that occurs when the doping concentrations are changed. However, as the result showed that the design principle does not work for homojunctions, the exact reason for why the inhomogeneos doped cells perform worse than a homogeneously doped cell is not essential to this thesis an not concluded on here.

Table 4.17: The efficiency, the total SRH recombination, and the total radiative recombination at $V = V_{\text{OC}}$ for the *GaAs, HJ - Uni.*, *GaAs, HJ - HL*, *GaAs, HJ - LH*, and *GaAs, HJ - HH* cells.

	GaAs, HJ - Uni.	*GaAs, HJ - HL*	*GaAs, HJ - LH*	*GaAs, HJ - HH*
Efficiency	1.97%	1.82%	1.79%	1.65%
Tot. SRH rec. rate	$2.89 \cdot 10^{24}$	$1.24 \cdot 10^{24}$	$1.77 \cdot 10^{24}$	$2.60 \cdot 10^{24}$
Tot. Rad. rec.	$1.62 \cdot 10^{21}$	$1.54 \cdot 10^{21}$	$1.78 \cdot 10^{21}$	$1.75 \cdot 10^{21}$

4.4.2 Layer Thicknesses

Five GaAs homojunctions labelled *GaAs, HJ - 1* to *GaAs, HJ - 5* (the reader is reminded that HJ denotes homojunction in this thesis) with different numbers and thicknesses of the layers have been simulated. Table 4.18 summarizes relevant parameters for these cells All layers have the same doping concentrations of $N_{\text{A}} = N_{\text{D}} = 9 \cdot 10^{17}$ cm^{-3}.

Results

Efficiency

The last column in Table 4.18 presents the simulated efficiencies of the the *GaAs, HJ - 1* to *GaAs, HJ - 5* cells The average efficiency was found to be $2.01 \pm 0.02\%$, the lowest being for the *GaAs, HJ - 3* cell at 1.97% and the highest for the *GaAs, HJ - 1* cell at 2.03%. While the layer thicknesses of the *GaAs, HJ - 2* and *GaAs, HJ - 5* are substantially different, they both resulted in the same efficiency at 2.02%.

Table 4.18: The number of layers, the layer thicknesses, and the simulated efficiency for the *GaAs, HJ - 1*, *GaAs, HJ - 2*, *GaAs, HJ - 3*, *GaAs, HJ - 4*, and *GaAs, HJ - 5* cells. The *HJ* denotes *homojunction*

GaAs, HJ - #	**Layer 1**		**Layer 2**		**Efficiency** [%]
1	500 nm		500 nm		2.03

GaAs, HJ - #	**Layer 1**	**Layer 2**	**Layer 3**	**Layer 4**	**Efficiency** [%]
2	250 nm	250 nm	250 nm	250 nm	2.02
3	480 nm	20 nm	40 nm	460 nm	1.97
4	20 nm	480 nm	460 nm	40 nm	2.03
5	495 nm	5 nm	5 nm	495 nm	2.02

Discussion

As no interfaces between the layers in the *GaAs, HJ - 1* to *GaAs, HJ - 5* cells were defined, they should all be identical and result in the same efficiency. This is clearly not what is happening in SCAPS. Likely, this is due the way SCAPS defines the mesh of points where the numerical calculations are done, because this is dependent on the layers. This is explained in the SCAPS manual [12], but it is elaborated on is the subsequent paragraphs.

As described in section 2.5, SCAPS uses appropriate boundary conditions at the interfaces and contacts together with Eq.(2.14), Eq.(2.15), and Eq.(2.16) to form a system of coupled differential equations. SCAPS then numerically calculates a steady state and a small signal solution of this system. Hereto, the cell is first discretized, i.e. creating a mesh. The meshing algorithm of SCAPS provides (taken directly from the SCAPS manual [12]):

– Coarse meshing in the middle of a layer.

– Finer meshing near the interfaces and contacts.

– Two discretization points (with identical spatial coordinate) for each interface.

– The mesh can be optimized during calculation.

The purpose of the meshing algorithm is to provide a greater number of points in regions where properties experience large variations (e.g. close to interfaces/contacts) and fewer points where the properties are expected to remain fairly constant (e.g. in the bulk). The SCAPS manual then states that this method may be insufficient with strong gradings, with multivalent defects or with the IPV-effect. To solve this, the distance between the mesh points can be adjusted under *Mesh generator settings* in SCAPS. The results from the simulations conducted here suggests that the standard mesh algorithm also may be insufficient when the cells consists of several (and especially thin) layers. In theory, this could also be fixed with an adjustment of the mesh generator settings. However, this would require that the settings are adjusted to each simulated cell with different layers, and that the adjustment are done so that the result is equal between different cells. Using Figure 4.32 as an example, where $17^2 = 289$ simulations with

different layer thicknesses were conducted, this would at best be very time consuming, but more realistically be impossible to get consistent. Therefore, no attempt in this thesis have been done to do this on any previous or upcoming simulations.

As the problem with the mesh setting not will be fixed in this thesis, it is necessary to understand the how this changes the simulated cells and the magnitude of the error. For all cells in section 4.1, section 4.2, and section 4.3, except where the layer thicknesses were varied in subsection 4.3.5, all cells have had the same layer thicknesses and all homogeneously doped cells have been simulated with four layers. This means that for these cells, the mesh settings have been the same. As a consequence, the error between the inhomogenously doped cells are likely of the same magnitude as the result found in Table 4.18, a few hundredth of a percentage point. This is substantially less than the difference between the cells and can thus be disregarded.

However, for the a homogeneously doped cell with four layers and similar cell with only two layers (which is relevant because this is how a real version of such a cell would be made) is the error likely larger. This is because here are the numbers of layer different and thus the mesh setting as well. Using the $GaAs^*$ - LE (homogeneously doped with four layers), the $GaAs^*$ - $2L$ (homogeneously doped with two layers), and the $GaAs^*$ - LE, HL (inhomogeneously doped with four layers) cells as an example, one can see how the mesh setting changes the magnitude of the efficiency increase when the design principle is applied. The efficiency increase between the $GaAs^*$ - LE and $GaAs^*$ - LE, HL cells is 13.37%. However, the efficiency increase between the $GaAs^*$ - $2L$ and $GaAs^*$ - LE, HL cells, the "correct" comparison, is less at 9.12%. However, the difference in efficiency between the $GaAs^*$ - LE and $GaAs^*$ - $2L$ cells is less than the increase when the design principle is applied. Therefore is the conclusion that all trends found until now holds true regardless of the problems with the mesh settings, but the magnitude of the positive effect of the design principle is lower than what the numeric values indicates.

For the cells where the layer thicknesses and thus the mesh settings have been varied (subsection 4.3.5), it is likely that all calculated efficiencies are both slightly incorrect and inconsistent between themself. However, the conclusion from that section was that such a thickness variation must be conducted in order to optimally utilize the design principle, and this conclusion holds true regardless. The numeric values are anyways of little interest there because they are only relevant for the exact cells that were simulated, and these used a modified value of the electron affinity that cannot be reproduced in real solar cells.

The next section aims to investigate the effect of inhomogeneous doping around the depletion region in IPV cells. Initially, this is done in GaAs homojunction IPV cell, where only the middle i-layer has impurities and thus is the only layer where the IPV effect can take place. A homojunction will be used in the first IPV simulations regardless of the findings in this section that showed that the design principle does not work for such homojunctions, because it is easier to work with a homojunction. After this, in section 3.7 and section 3.8, will the design principle be tested on IPV heterojuntions.

4.5 GaAs Homojunction IPV Cells

This section aims to introduce and optimize inhomogeneous doping concentrations around the middle i-layer in a p-i-n GaAs IPV homojunction (the green layer in Figure 4.42). This is done by first optimizing the doping concentrations and the i-layer thickness (subsection 4.5.1), then splitting the n- and p-layers and varying the doping and thicknesses of the layers in contact with the i-layer (subsection 4.5.2 and subsection 4.5.3, respectively). In order to keep track of the doping, layer numbers, and layer names of the cells, are this summarized Figure 4.42. As seen in the figure, the original p-layer is labelled p*, and layer split into two layer labelled p and p$^-$. Similarly, the original n-layer is labelled n*, and later split into two layers labelled n$^-$ and n. The inhomogeneous doping concentrations are only applied to the p$^-$ and n$^-$ layers. This notation is also used for the IPV cells in the next two sections.
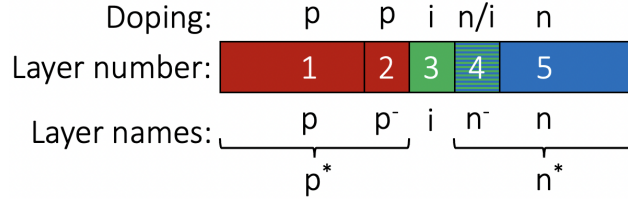

Figure 4.42: The doping, layer numbers, and layer names of the IPV cells in this thesis. As illustrated, $t_\text{p}^* = t_\text{p} + t_\text{p}^-$ and $t_\text{n}^* = t_\text{i}^- + t_\text{n}$, where t labels thickness.

It is explicitly noted that only the middle i-layer (the green layer in Figure 4.42) have defects in these cells. This deliberate choice was made for two reasons. Firstly, in an IPV cell, it is desirable that defects only are present where the IPV effect can take place. This is because defects without the possibility for optical generation only can contribute negative to the cell via the SRH recombination mechanism. Secondly, it is possible to fabricate near defect-free materials, so the simulations with defect-free layers are possible to recreate experimentally.

4.5.1 p-i-n IPV Cells

Initially, two identical cells, except only one has the IPV effect enabled, were simulated. These are labelled *GaAs, No IPV* and *GaAs, IPV*. Then, the doping concentrations of the p*- and n*-layers and the i-layer thickness t_i, were optimized for the *GaAs, IPV* cell. This resulted in a new cell labelled *GaAs, IPV - pin*.

Results

Reference Cell Performance Parameters

The performance parameters for the *GaAs, No IPV* and *GaAs, IPV* cells are summarized in Table 4.19. The results shows that the activation of optical generation of the carriers via the impurities, i.e. the IPV effect, increased the efficiency.

Table 4.19: Performance parameters for the *GaAs, No IPV* and *GaAs, IPV* cells.

	η [%]	J_SC [mA/cm^2]	V_OC [V]	FF [%]
GaAs, No IPV	28.16	30.33	1.05	88.90
GaAs, IPV	29.17	31.44	1.06	87.90

Efficiency vs. Doping concentration and i-layer Thickness

As shown in Figure 4.43a, at a fixed acceptor doping concentration $N_A = 9 \cdot 10^{17}$ cm^{-3}, was the donor doping concentration varied. The highest efficiency was found to be 31.26% at $N_D = 1 \cdot 10^{17}$ cm^{-3}. Then, as show in Figure 4.43b, using the found value of N_D, was the acceptor doping concentration varied. The highest efficiency was found to be 31.64% at $N_A = 1 \cdot 10^{17}$ cm^{-3}. Thus, the optimum doping concentration for the *GaAs, IPV* cell was found to be $N_D = N_A = 1 \cdot 10^{17}$ cm^{-3}.

(a) Donor doping in n*-layer   (b) Acceptor doping in p*-layer
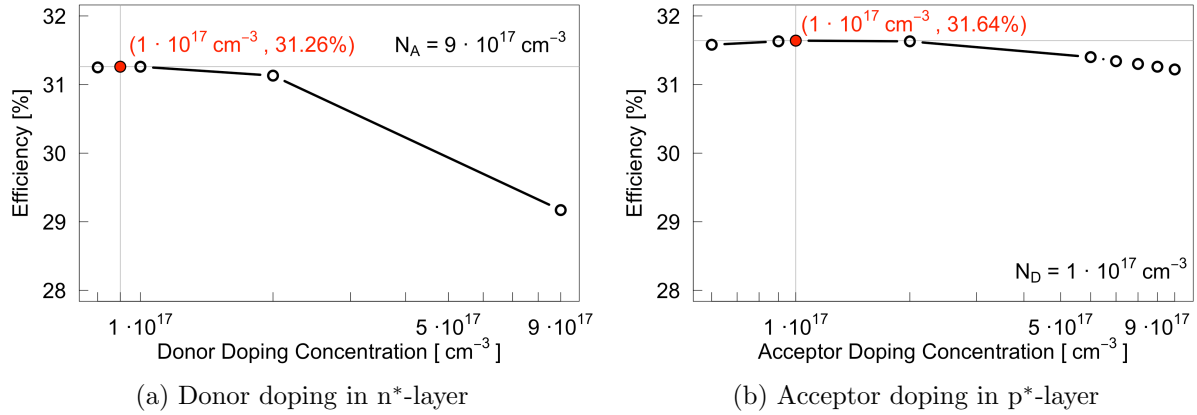
Figure 4.43: The effect on the efficiency when the (a) the donor doping and (b) the acceptor doping were varied in the n*- and p*-layer in *GaAs, IPV* cell, respectively.

Using the found values of the acceptor and donor doping concentration, was the i-layer thickness t_i varied while the p*- and n*-layer thicknesses t_p^* and t_n^* were kept at a constant thickness at 495 nm each. The highest efficiency was found to be 33.90% at a i-layer thickness of 100 nm. Thus, the total cell thickness using the optimum thickness of the i-layer is 1090 nm. This cell is labelled *GaAs, IPV - pin*.
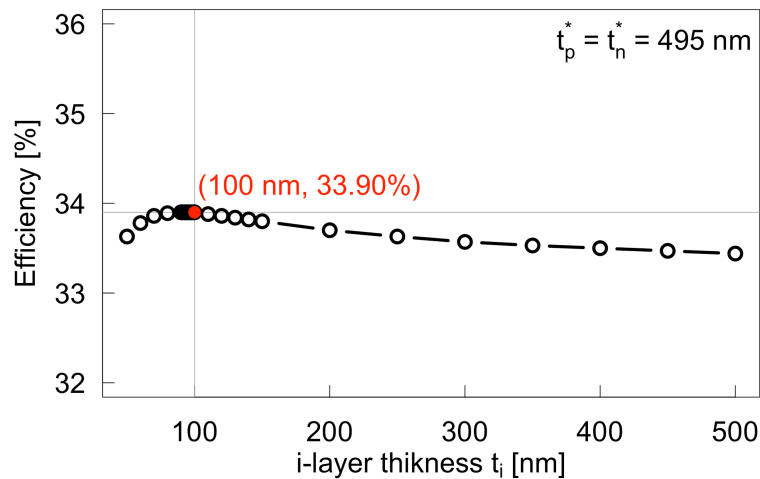

Figure 4.44: The effect on the efficiency when the i-layer thickness t_i in the *GaAs, IPV* cell is varied. The thicknesses of the p*- and n*-layer were kept constant at $t_p^* = t_n^* = 495$ nm.

Performance Parameters

The performance parameters of the *GaAs, IPV - pin* cell are summarized in Table 4.20. Compared to the *GaAs, IPV*, is the efficiency of the *GaAs, IPV - pin* is 16.22% or 4.73 percentage pints higher.

Table 4.20: Performance parameters for the *GaAs, No IPV*, *GaAs, IPV*, and *GaAs, IPV* - pin cells.

	η [%]	J_{SC} [mA/cm^2]	V_{OC} [V]	FF [%]
GaAs, No IPV	28.16	30.33	1.05	88.90
GaAs, IPV	29.17	31.44	1.06	87.90
GaAs, IPV - pin	33.90	38.52	1.05	83.43

Energy Band Diagram and Recombination Rates

The energy band diagram and the radiative and SRH recombination rates at $V = V_{\text{OC}}$ for the *GaAs, IPV - pin* cell are given in Figure 4.45a and Figure 4.45b, respectively. The SRH recombination rate is plotted as its absolute value as a negative value in SCAPS means that the generation via the impurity is larger than the recombination, and it is plotted on a logarithmic scale and can thus not be negative. This is also described in subsection 2.5.3.
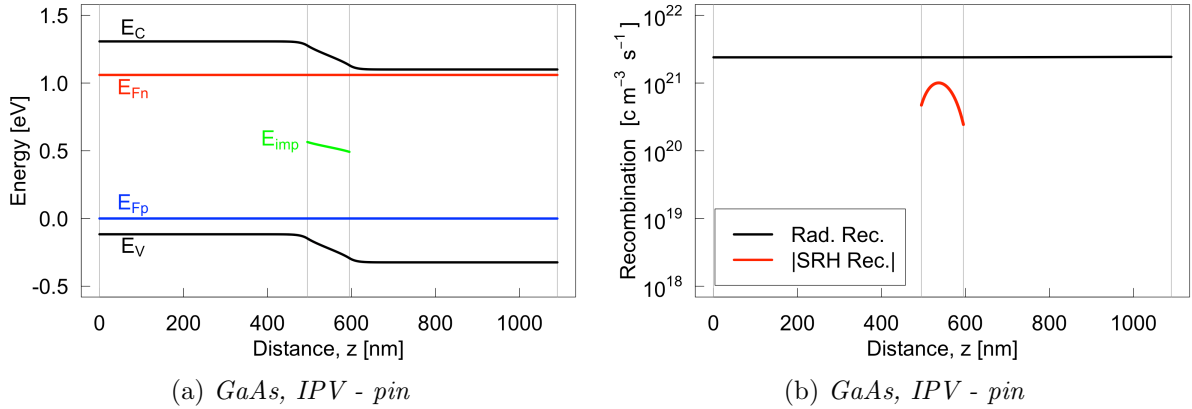

(a) *GaAs, IPV - pin*

(b) *GaAs, IPV - pin*

Figure 4.45: (a) The energy band diagram and (b) the recombination rates at $V = V_{\text{OC}}$ for the *GaAs, IPV - pin* cell. The SRH recombination rate is plotted as its absolute value. The vertical lines indicates the interfaces between the layers.

Discussion

As can be seen from the performance parameters in Table 4.20, the efficiency of the cell without the IPV effect (*GaAs, No IPV*) is very high. This is partly due to the fact that it only has impurities in the i-layer, and thus SRH recombination can only occur there. Comparing this cell with the cell where the IPV effect is enabled (*GaAs, IPV*), one can see that the cell benefited from the IPV effect. This is another way of saying that the generation rate via the impurities is greater than the recombination rate via the same impurities. This is not a general result, as the IPV effect can have a net negative effect. Whether the net result is positive or negative depends on several factors such as the magnitudes of the CCS and the impurity density. Regardless, the most important part of the cells in the context of inhomogeneous doping is *that* the total effect is positive.

As can be seen from Figure 4.43a and Figure 4.43b, did the optimization of the doping concentrations result in a slightly increased efficiency. This is due to, as explained in several previous

sections, an optimization of the quasi-Fermi level distance and the band-to-band recombination. The reason why the change in efficiency is low, especially for Figure 4.43b, is that the values are based on previous optimized values from previous simulated cells in this thesis, and the initial values were thus not far from the optimal value.s In Figure 4.43a, it can seem like one should simulate cells with lower doping concentrations to be sure that the best value was found. However, as the first point is lower than the second (which is the highest), and the curve only has one maximum, one can be sure that the highest point was found.

The efficiency when the i-layer thickness was varied had an optimum value, which for this cell was found to be 100 nm as shown in Figure 4.44. With a greater i-layer thickness, more carriers can be generated due to the IPV effect. In addition, the depletion region width of the cell increases. This is initially beneficial, as it increases the region with an electric field, which can result in more successful separation of generated electron-hole pairs. However, with a too large depletion region, does the lifetime of the carriers become a limiting factor, as the carriers recombine before they can contribute to the current. In the energy band diagram of the $GaAs$, IPV - pin cell in Figure 4.45b, the depletion region is seen as the part where the energy bands are non-constant with respect to position, and it can clearly be seen that this section is larger than e.g. for the $GaAs$, HJ - $Uni.$ cell as shown in Figure 4.39a.

Also shown in Figure 4.44, are the thicknesses of the p*- and n*-layers of kept constant at 495 nm each. As the optimal value of the i-layer was found to be 100 nm, the total cell thickness of the $GaAs$, IPV - pin cell is thus 1090 nm. In other words, the i-layer thickness was varied without varying the p*- and n*-layers. This is not a mistake in itself, but it leaves the resulting thickness to be different from all previous cells. It can therefore be argued that it would be better to vary the i-layer thickness while keeping the total cell thickness constant at 1000 nm. Unfortunately, as too many cells of the new thickness were simulated at the point when this aspect was considered and due to time limitations, this is not corrected. However, as the previous simulated cells without the IPV effect differs fundamentally from the cells in this section, it is not a major concern.. What is important is that all IPV cell are of the same thickness, which they are. If they were not the same thickness, the absorption of between the cells would differ and it would be more difficult to isolate the effect of the inhomogeneous doping.

The SRH recombination rate of the $GaAs$, IPV - pin cell has a optimum in the middle of the depletion region at $z \approx 545$ nm as show in Figure 4.45. This means that the difference between the generation and recombination rates via the impurities is largest here. As have been seen in previous cells simulated cells, is the SRH recombination rate is largest in the middle of the depletion region. This means that the generation rate also is largest in the middle, because the peak value is also found in the middle for the IPV cells. The aim of the inhomogeneous doping will be to reduce the SRH recombination in the middle i-layer.

4.5.2   p-i-n-n IPV Cells

In this subsection, the n*-layer in the $GaAs$, IPV - pin cell is split into two layers. Initially, the thickness of the rightmost layer is $t_n = 445$ nm while the layer in contact with the i-layer is $t_n^- = 50$ nm. First, using this configuration, the doping concentration of the thin n⁻-layer is optimized. Then, using the found optimum doping concentration, the thickness of the n⁻-layer is optimized while keeping the sum of the thicknesses of the two layer constant at 495 nm, i.e. $t_n^* = t_n^- + t_n = 495$ nm. The resulting cell is then labelled $GaAs$, IPV - $pinn$.

Results

Efficiency vs. n-layer Thickness and Doping Concentration

Figure 4.46a shows the result on the efficiency when the doping concentration in the n^--layer in contact with the i-layer is varied. All doping concentrations from and below $1 \cdot 10^{14}$ cm^{-3} resulted in the highest efficiency at 35.35%. This means that the highest efficiency can be obtained by completely removing the doping, i.e. creating an i-layer (without the IPV effect nor impurities) instead of a n-layer. Using this new i-layer (but still labelled the n^--layer), the thickness of this layer t_n^- is varied as shown in Figure 4.46b. The highest efficiency was found to be 35.45% at $t_n^- = 100$ nm, making the n-layer thickness $t_n = 495\text{nm} - 100\text{nm} = 395\text{nm}$. This cell is labelled *GaAs, IPV - pinn*.

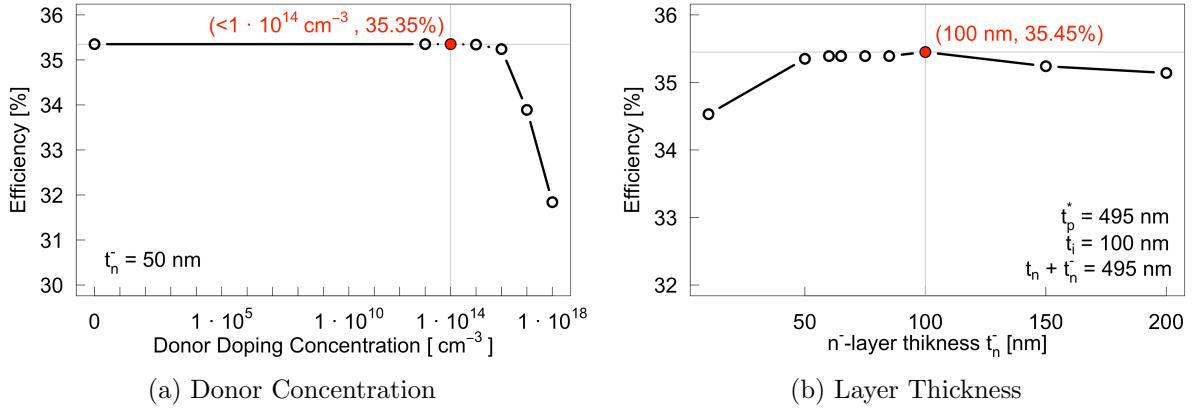(a) Donor Concentration (b) Layer Thickness

Figure 4.46: (a) The effect on the efficiency when the doping concentration is varied in the n^--layer in contact with the i-layer. (b) The effect on the efficiency when the thickness of the n^--layer, t_n^-, is varied. The doping concentration of this layer is 0 cm^{-3}, i.e. actually making it an i-layer, but without the IPV effect nor impurities.

Performance Parameters

The performance parameters of the *GaAs, IPV - pinn* cell are summarized in Table 4.21. Compared to the *GaAs, IPV - pin*, the efficiency of the *GaAs, IPV - pinn* is 3.95% higher.

Table 4.21: Performance parameters for the *GaAs, No IPV*, *GaAs, IPV*, *GaAs, IPV - pin*, and *GaAs, IPV - pinn* cells.

	η [%]	J_{SC} [mA/cm^2]	V_{OC} [V]	FF [%]
GaAs, No IPV	28.16	30.33	1.05	88.90
GaAs, IPV	29.17	31.44	1.06	87.90
GaAs, IPV - pin	33.90	38.52	1.05	83.43
GaAs, IPV - pinn	35.45	38.62	1.06	86.92

Energy Band Diagram and Recombination Rates

The energy band diagram and the radiative and SRH recombination rates at $V = V_{\mathrm{OC}}$ for the *GaAs, IPV - pinn* cell are given in Figure 4.47a and Figure 4.47b, respectively.

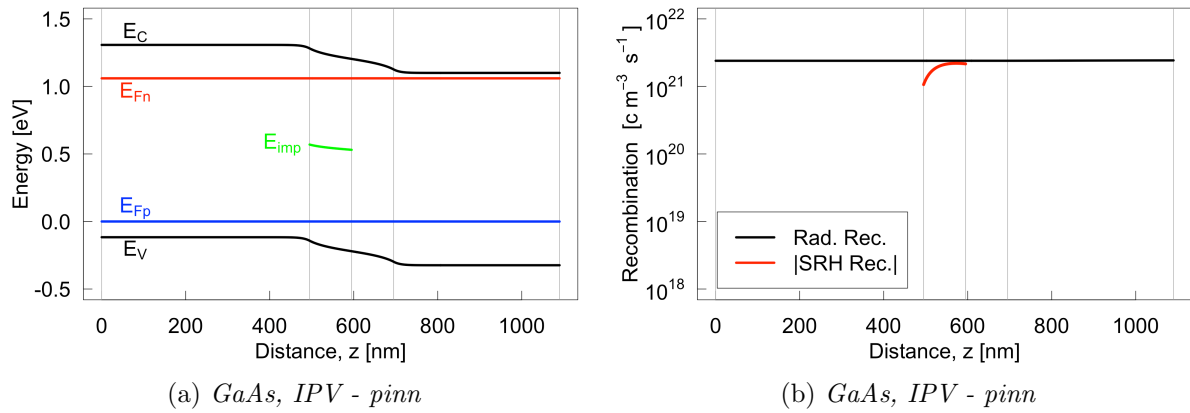

(a) *GaAs, IPV - pinn* (b) *GaAs, IPV - pinn*

Figure 4.47: (a) The energy band diagram and (b) the recombination rates at $V = V_{\mathrm{OC}}$ for the *GaAs, IPV - pinn* cell. The SRH recombination rate is plotted as its absolute value. The vertical lines indicates the interfaces between the layers.

Discussion

As can be seen from Figure 4.46a, all doping concentrations below $1 \cdot 10^{14}$ cm^{-3} resulted in the highest efficiency. In practice this is a beneficial result because it means that one does not need to dope the used material for the thin n$^-$-layer, and that it is tolerant to a certain amount of impurities. It is suggested here that the inclusion of the i-layer (still labelled n$^-$), similarly to the middle i-layer with the IPV effect, is beneficial to the cell because it increases the depletion region width. At a sufficiently thin additional i-layer will the depletion region cover cross this layer. It can be seen from the energy band diagram in Figure 4.47a that this is the case for the *GaAs, IPV - pinn* cell as E_C and E_V are non-constant with respect position in the n$^-$-layer. The reason for why the wider depletion region width is better is because it more effectively removes the generated electron-hole pairs before they recombine.

As can be seen from Figure 4.46b, a optimum of the efficiency was found when varying the n$^-$-layer. A too large thickness results in too little of the previous single n*-layer to be without doping. This negatively affects the electrical properties of the cell, resulting in a reduction in efficiency. However, a too thin i-layer does not fully utilize the benefit of the increase in depletion region width.

Looking at the SRH recombination rate in Figure 4.47b, one can see that the sum of the generation rate minus the recombination rate via the impurity has increased in the right side of the IPV layer. This is correlated with the descriptions above. By adding in the n$^-$-layer on the right side of the IPV layer does the depletion region increase to the right. Thus, the carriers are more effectively removed so that thy do not have as large probability of recombining, resulting in a larger absolute value of the SRH recombination.

Recalling the results from the homojunction p-n GaAs cells in section 4.4, one could theorize that a change in doping concentration in one of the doped layers in the p-i-n GaAs homojunction cell here should not result in a improvement in the efficiency. However, the effect of the changes in doping concentration here is not the same as in the paper by Santhanam and Fan [11]. Actually, it cannot be the same as here is the doping totally removed, while there it only was

reduced. In addition, this is a homojunction and it has been shown in the previous section that the design principle does not work for them. The positive result is instead likely due to, as described above, a increase in the depletion region width.

4.5.3   p-p-i-n-n IPV Cells

In this subsection, the same procedure as was done on the n*-layer in the previous subsection is repeated on the p*-layer in the *GaAs, IPV - pinn* cell. The only difference is that the starting thickness of the p$^-$-layer was 100 nm, i.e. the optimum thickness of the n$^-$-layer. The resulting cell is labelled *GaAs, IPV - ppinn*.

Results

Efficiency vs. p-layer Thickness and Doping Concentration

Figure 4.48a shows the result on the efficiency when the doping concentration in the thin p$^-$-layer is varied. The highest efficiency was found to be 35.75% at a doping concentration of $2 \cdot 10^{16}$ cm^{-3}. Using this doping concentration, the thickness of the p$^-$-layer layer is varied as shown in Figure 4.46b. While the changes were small, all thicknesses of the p^--layer between 75 nm and 300 nm resulted in the same highest efficiency of 35.75%. The lowest value at 75 nm was chosen for the p^- layer, i.e. making $t_\text{p} = 495\text{nm} - 75\text{nm} = 420\text{nm}$. This cell is denoted *GaAs, IPV - ppinn*.
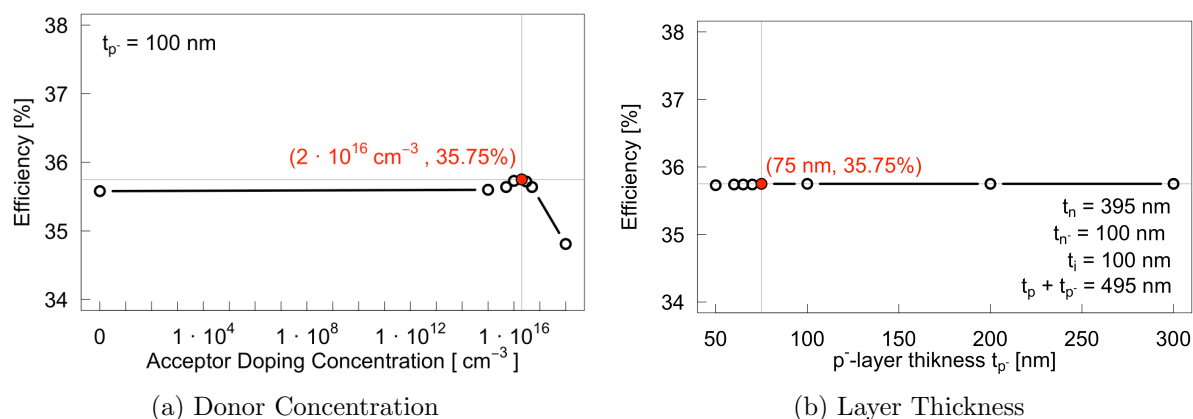

Figure 4.48: (a) The effect on the efficiency when the doping concentration is varied in the narrow p-layer. (b) The effect on the efficiency when the thickness of the narrow n-layer is varied. The doping concentration of the layer is $2 \cdot 10^{16}$ cm^{-3}.

Performance Parameters

The performance parameters of the *GaAs, IPV - ppinn* cell are summarized in Table 4.22. Compared to the *GaAs, IPV - pinn*, is the efficiency of the *GaAs, IPV - ppinn* is 0.85% higher.

101

Table 4.22: Performance parameters for the *GaAs, No IPV*, *GaAs, IPV*, *GaAs, IPV - pin*, *GaAs, IPV - pinn*, and *GaAs, IPV - ppinn* cells.

	η [%]	J_{SC} [mA/cm^2]	V_{OC} [V]	FF [%]
GaAs, No IPV	28.16	30.33	1.05	88.90
GaAs, IPV	29.17	31.44	1.06	87.90
GaAs, IPV - pin	33.90	38.52	1.05	83.43
GaAs, IPV - pinn	35.45	38.62	1.06	86.92
GaAs, IPV - ppinn	35.75	38.62	1.06	87.65

Energy Band Diagram and Recombination Rates

The energy band diagram and the radiative and SRH recombination rates at $V = V_{\text{OC}}$ for the *GaAs, IPV - ppinn* cell are given in Figure 4.49a and Figure 4.49b, respectively.

To compare the effect of the addition of the n$^-$-layer in the *GaAs, IPV - pinn* cell and the p$^-$-layer in the *GaAs, IPV - ppinn* cell, all SRH recombination rates at $V = V_{\text{OC}}$ between $z = 490$ nm and $z = 600$ nm for the *GaAs, IPV - pin*, *GaAs, IPV - pinn*, and *GaAs, IPV - ppinn* cells are shown in Figure 4.50.
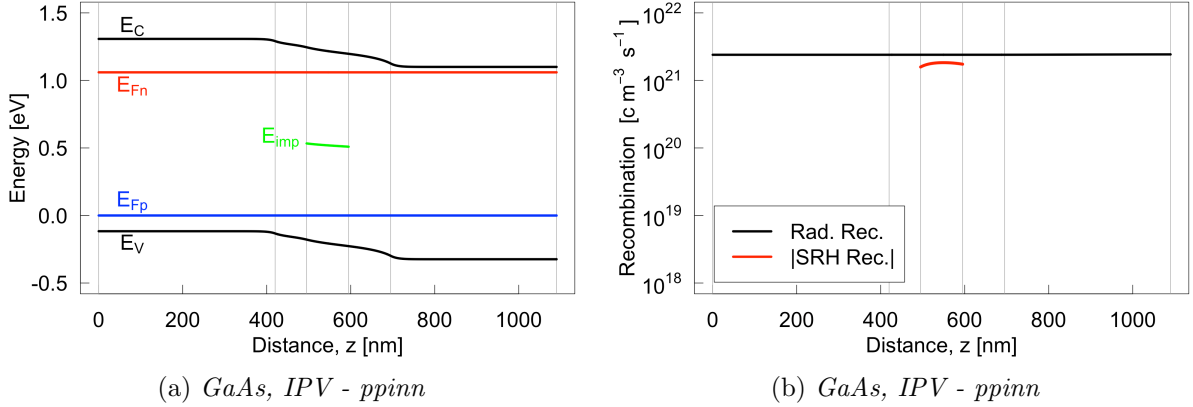

(a) *GaAs, IPV - ppinn*   (b) *GaAs, IPV - ppinn*

Figure 4.49: (a) The energy band diagram and (b) the recombination rates at $V = V_{\text{OC}}$ for the *GaAs, IPV - ppinn* cell. The SRH recombination rate is plotted as its absolute value. The vertical lines indicates the interfaces between the layers.
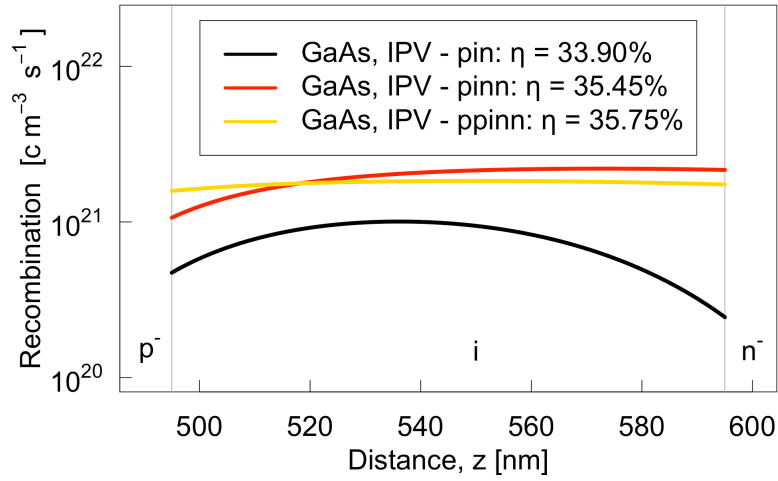
Figure 4.50: SRH recombination rates at $V = V_{OC}$ between $z = 490$ nm and $z = 600$ nm for the *GaAs, IPV - pin*, *GaAs, IPV - pinn*, and *GaAs, IPV - ppinn* cells. They are all plotted as their absolute value. The vertical lines indicates the interfaces between the layers, and the letters are the labelled names of the visible layers.

Discussion

Again, the result showed that a change in doping concentration in the layer in contact with the IPV i-layer improved the efficiency. However, as seen by the performance parameters in Table 4.19, the improvement was less when changing the p^--layer than the n^--layer. Contrarily to in the n^--layer and as can be seen in Figure 4.48a, the optimum doping concentration was found to be a single value above zero. Also, as shown in Figure 4.48b, it was found that for all thicknesses above a sufficient thickness resulted in the highest efficiency. This is somewhat surprising as the doping concentration of the p-layer already have been optimized in subsection 4.5.1. It suggests that the introduction of the second i-layer changed the optimum value of the acceptor doping. Possibly, one could use this new doping concentration in both p-layers (i.e. the p*-layer), and then do a new optimization of the p^--layer. However, due to time limitations, this is not done in this thesis.

The reason for why the cell experiences an increase in efficiency when the doping concentrating is changed is again explained by the increase in depletion region width and the more effective removal of the carriers. However, as seen by comparing all SRH recombination ration rates in Figure 4.50, it seems like the net generation rate (generation - recombnation) via the impurity is larger for the *GaAs, IPV - pinn* cell than for the *GaAs, IPV - ppinn* cell. This seems contradictory as the latter has the highest efficiency. However, by summing up the total SRH recombination at $V = V_{OC}$ for the cells, one can see that in fact the net generation is lower for the *GaAs, IPV - ppinn* cell. This is summarized in Table 4.23. Therefore, other factors than just the reduction of the SRH recombination must take place when the doping concentration of the p^--layer is changed since the efficiency is improved. No plausible suggestions to what these other factor are were found in this thesis, and more research is needed.

The results from this section showed that an inhomogeneous doping concentration around the i-layer in a p-i-n GaAs IPV homojunction resulted in an increase in efficiency. In fact the increase was found to be substantial at 5.46% or 1.85 percentage points, and it is enough to suggest that the changes shown here can be applied to real IPV cells. The effect is not the same as was found by Santhaman and Fan, and it could not be it either as it was applied to a homojunction. The important part is that one can obtain a higher efficiency of the cells, not necessarily which principle that is applied. However, it is possible that the principle can be applied to a heterojunction p-i-n IPV cell and that this would have an even greater effect.

Therefore, the next section aims to replicate the procedures conducted in this section in a p-GaAs/i-GaAs/n-AlGaAs IPV cell. However, as have been seen in previous simulations in this thesis, the CB offset between the GaAs and AlGaAs prevents the positive effect of the principle. Therefore, also here will the intrinsic property the electron affinity GaAs be modified to remove this offset.

Table 4.23: Absolute value of total SRH recombination at $V = V_{OC}$ for the *GaAs, IPV - pin*, *GaAs, IPV - pinn*, and *GaAs, IPV - ppinn* cells. A higher value indicates a higher net generation via the impurity.

Cell	GaAs, IPV - pin	GaAs, IPV - pinn	GaAs, IPV - ppinn
Total SRH rec. rate	$8.73 \cdot 10^{22}$ cm^{-3}s^{-1}	$2.20 \cdot 10^{23}$ cm^{-3}s^{-1}	$1.80 \cdot 10^{23}$ cm^{-3}s^{-1}

4.6 Modified GaAs/GaAs/AlGaAs IPV cells

This section aims to redo the simulation procedure conducted on the GaAs homojunction IPV cells in section 4.5, however this time using a p-GaAs*/i-GaAs*/n-AlGaAs IPV heterojunction. The asterix in GaAs again indicates that the electron affinity have been changed to remove the CB offset between the two materials GaAs and AlGaAs. The convention of the doping, layer numbers, and layer names of the cells from the previous section (see Figure 4.42) is repeated here.

The doping concentrations of the two p*- and n*-layers are set to be the same value as was found to be the optimum values in subsection 4.5.1, i.e. $N_D = N_A = 1 \cdot 10^{17}$ cm^{-3}. Similarly, the found optimal thickness of the middle i-layer in the same section of 100 nm is used in the middle i-layer of the cells in this section as well. By doing this, the only difference between the cells in the previous section and this section before including in the inhomogeneously doped layers is the replacing of the n-GaAs layer with a n-AlGaAs layer. Thus, the difference of inhomogeneously doping concentrations in homojunction IPV cells and heterojunction IPV cells can be observed.

This section consist of two main parts. First, in subsection 4.6.1, the CB offset between GaAs and AlGaAs is removed. This results in two cells labelled *GaAs, IPV - CB* (i.e. with a CB offset) and *GaAs*, IPV - pin* (i.e. without a CB offset). Then, in subsection 4.6.2, the inhomogeneous doping concentration is applied to the CB offset-free cell. In contrast to the previous section, this is done for both the p*- and n*-layers in one subsection. This resulted in two cells labelled *GaAs*, IPV - pinn* and *GaAs*, IPV - ppinn*,

Again, the reader is reminded that only the middle i-layer has impurities and it is thus the only layer with the IPV effect.

4.6.1 Conduction Band Offset

As the result from section 4.2 showed that the CB band barrier in GaAs/AlGaAs heterojuntions prevents the positive effect of the design principle by Santhanam and Fan [11], this section aims to remove this barrier by changing the electron affinity of GaAs so that the design principle can be investigated fruther. The reader is again reminded that this is not possible to do in real GaAs.

Results

Energy Band Diagrams

Initially, an p-GaAs/i-GaAs/n-AlGaAs IPV cell labelled the *GaAs, IPV - CB* cell was simulated. The energy band diagram at $V = V_{OC}$ for this cell is shown in Figure 4.51a. The result showed that a CB barrier of $\Delta E_C = 0.33$ eV was formed between the i-GaAs and n-AlGaAs. Using Anderson's rule and Eq.(2.6), a modified value of the electron affinity for the GaAs, $\chi_{GaAs, \, new}$ (both i-GaAs and p-GaAs), that removes the barrier was calculated to be

$$\chi_{GaAs, \, new} = \chi_{GaAs, \, old} - \Delta E_C = 4.07 \text{ eV} - 0.33 \text{ eV} = 3.74 \text{ eV} \tag{4.7}$$

Using this modified value for the electron affinity in the GaAs layers, a new cell denoted the *GaAs*, IPV - pin* cell was simulated, where the asterix in GaAs indicates the modification. Its energy band diagram at $V = V_{OC}$ is given in Figure 4.51b, and one can there see that the CB offset was removed.
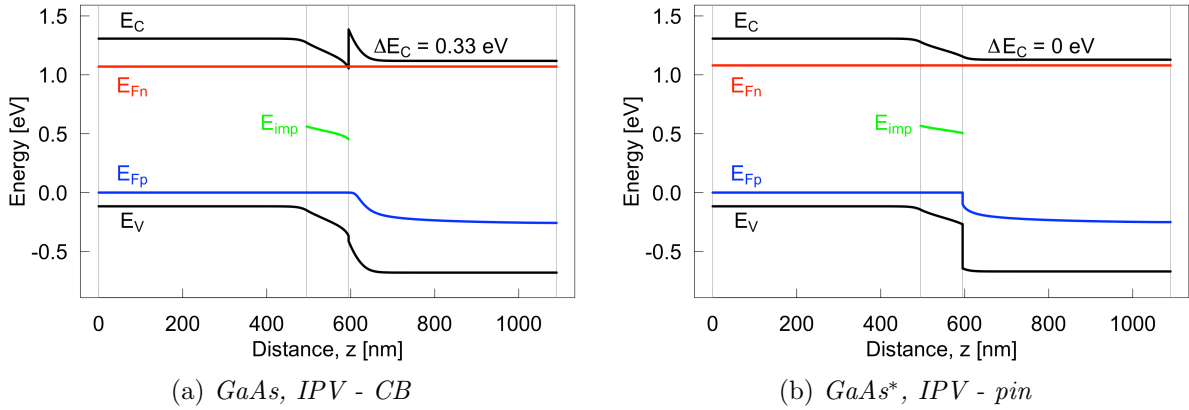

(a) *GaAs, IPV - CB* (b) *GaAs*, IPV - pin*

Figure 4.51: The energy band diagram at $V = V_{OC}$ for (a) the *GaAs, IPV - CB* cell and (b) the *GaAs*, IPV - pin*. The vertical lines indicates the interfaces between the layers.

Performance Parameters

The performance parameters of the *GaAs, IPV - CB* and *GaAs*, IPV - pin* cells are summarized in Table 4.24. In addition, the performance parameters of a new cell denoted *GaAs*, No IPV* is included in the same table. This cell is identical to the *GaAs*, IPV - pin*, except optical capture of the carriers via the impurities is disabled (i.e. no IPV effect). Comparing the efficiency of the *GaAs*, IPV - pin* cell and the *GaAs*, No IPV* cell, one can see that these cells benefits from the IPV effect. Additionally, by comparing the *GaAs, IPV - CB* cell and the *GaAs*, IPV - pin* cell, one can also see that the removal of the CB barrier has a slightly positive effect on the cell efficiency.

Table 4.24: Performance parameters for the *GaAs, IPV - CB*, *GaAs*, IPV*, and *GaAs*, No IPV* cells.

	η [%]	J_{SC} [mA/cm^2]	V_{OC} [V]	FF [%]
GaAs, IPV - CB	33.06	38.03	1.07	81.29
GaAs*, IPV - pin	34.71	38.73	1.07	83.75
GaAs*, No IPV	30.95	32.92	1.07	88.12

Recombination Rates

The radiative and SRH recombination rates at $V = V_{\mathrm{OC}}$ for the *GaAs, IPV - CB* and *GaAs**, *IPV - pin* cells are shown in Figure 4.52a and Figure 4.52b, respectively. The plots for the recombination rates for the *GaAs, IPV - CB* cell is omitted as this is not the cell which will undergo the upcoming changes in doping concentrations.
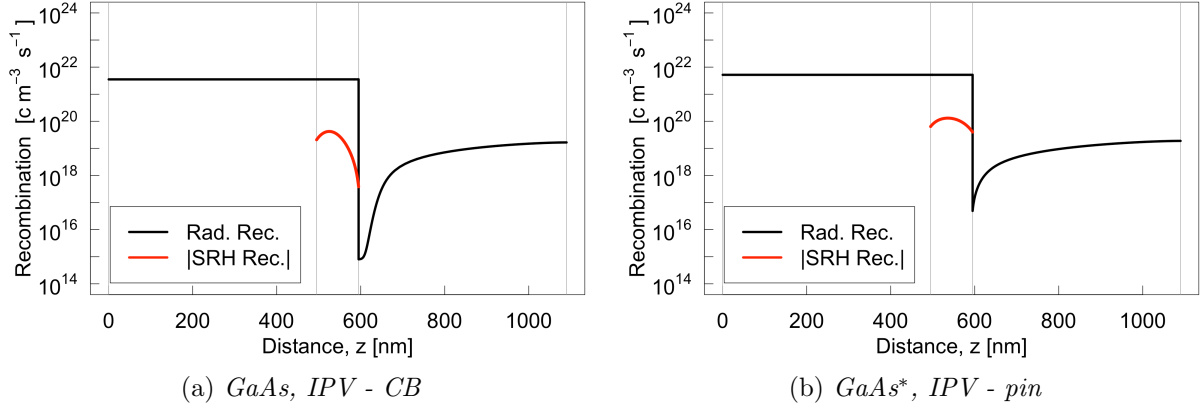

(a) *GaAs, IPV - CB*

(b) *GaAs*, IPV - pin*

Figure 4.52: The recombination rates at $V = V_{\mathrm{OC}}$ for (a) the *GaAs, IPV - CB* cell and (b) the *GaAs*, IPV - pin*. The SRH recombination rate is plotted as its absolute value. The vertical lines indicates the interfaces between the layers.

Discussion

The main takeaway from this subsection is that the CB offset successfully was removed by changing the electron affinity of the GaAs while recalling that this is an intrinsic material property. This means that it is not possible to change this value in a real materials. Thus, the subsequent results when the inhomogeneous doping concentration around the i-layer is applied will be relevant for a general IPV heterojunction without band offsets, not specifically for GaAs and AlGaAs. In addition, the results here showed that the cells benefited from the IPV effect, i.e. the generation is larger than the recombination via the impurities.

4.6.2   p-p-i-n-n IPV Cells

In this section, the n-AlGaAs layer is split into two layers, n$^-$ and n, where the former is in contact with the i-layer. Initially, the thickness of the n$^-$-layer is 50 nm. At this thickness, the doping concentration of this layer was optimized. Using the found optimal value, the thickness of the n$^-$-layer was optimized. This is done while keeping the total combined thickness of the n$^-$- and n-layers constant at 495 nm. The resulting cell of these simulations is labelled *GaAs**, *IPV - pinn*.

Next, the same procedure was done for the p-GaAs* layer, i.e. splitting it to form a p and a p$^-$ layer, and optimizing the doping and thickness of the p$^-$-layer. The combined n$^-$- and n-layers thickness was 495 nm. The resulting cell of these simulations is labelled *GaAs*, IPV - ppinn*.

Results

Efficiency vs. n-layer Thickness and Doping Concentration

Using a thickness of 50 nm in the n$^-$-layer, the doping concentration was varied as shown in Figure 4.53a. All doping concentrations from and below $1 \cdot 10^{14}$ cm^{-3} resulted in the highest efficiency at 36.03%. This means that the highest efficiency can be obtained by removing the

doping all together in this layer, i.e. creating an i-layer. The thickness of this new i-layer without the IPV effect or impurities was then varied as shown in Figure 4.53b. The highest efficiency was found to be 36.08% at a thickness of 77 nm. The cell with the additional 77 nm i-layer is denoted *GaAs*, IPV - pinn*.
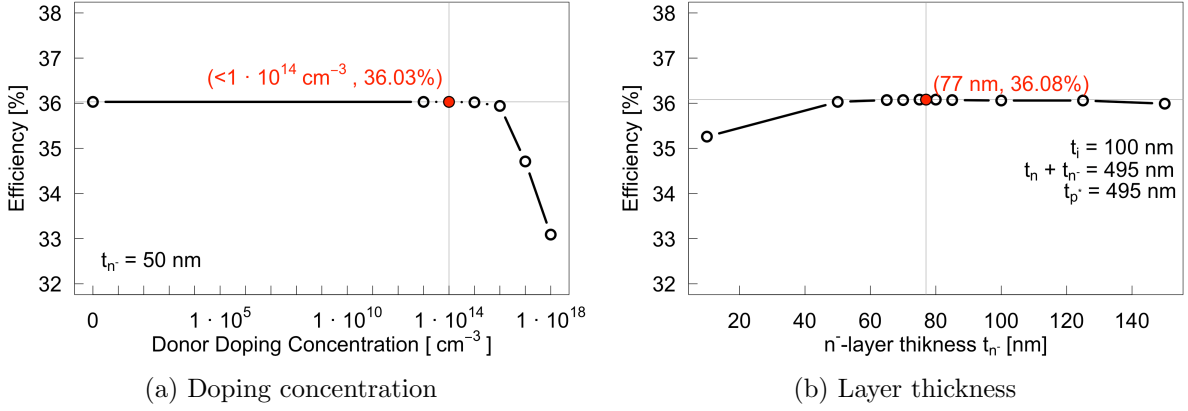

(a) Doping concentration

(b) Layer thickness

Figure 4.53: (a) The effect on the efficiency when the doping concentration is varied in the narrow n-layer. (b) The effect on the efficiency when the thickness of the narrow n-layer is varied. The doping concentration of the n^--layer is 0 cm^{-3}, i.e. actually making it an i-layer.

Performance Parameters

The performance parameters of the *GaAs*, IPV - pinn* cell are summarized in Table 4.25. The previous modified GaAs IPV cells are included for comparison. The result showed that *GaAs*, IPV - pinn* cell has a 3.94% higher efficiency than the homogeneously doped *GaAs*, IPV - pin* cell.

Table 4.25: Performance parameters for the *GaAs*, IPV - pinn* cell.

	η [%]	J_{SC} [mA/cm^2]	V_{OC} [V]	FF [%]
GaAs, IPV - CB	33.06	38.03	1.07	81.29
GaAs, IPV - pin*	34.71	38.73	1.07	83.75
GaAs, No IPV*	30.95	32.92	1.07	88.12
GaAs, IPV - pinn*	36.08	38.74	1.07	86.93

Energy Band Diagram and Recombination Rates

The energy band diagram and the radiative and SRH recombination rates at $V = V_{OC}$ for the *GaAs, IPV - pinn* cell are given in Figure 4.54a and Figure 4.54b, respectively.
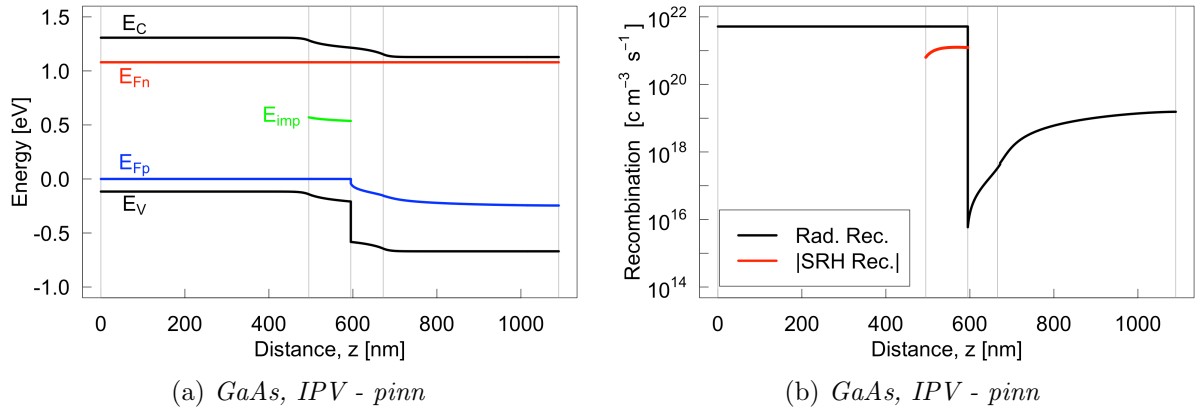
(a) *GaAs, IPV - pinn*

(b) *GaAs, IPV - pinn*

Figure 4.54: (a) The energy band diagram and (b) the recombination rates at $V = V_{\mathrm{OC}}$ for the $GaAs^*$, IPV - $pinn$ cell. The SRH recombination rate is plotted as its absolute value. The vertical lines indicates the interfaces between the layers.

Efficiency vs. p-layer Thickness and Doping Concentration

Figure 4.55a shows the result on the efficiency when the doping concentration in the p^--layer is varied at a thickness of 50 nm. The highest efficiency was found to be 36.32% at a doping concentration of $8 \cdot 10^{15}$ cm^{-3}. Using this doping concentration, the thickness of the same layer is varied as shown in Figure 4.55b. Only at a thickness between 40 and 50 nm was the efficiency of 36.32% obtained The middle value at 45 nm is chosen for the p^- layer, i.e. making $t_{\mathrm{p}} = 495\mathrm{nm} - 45\mathrm{nm} = 450\mathrm{nm}$. This cell is labelled $GaAs^*$, IPV - $ppinn$.

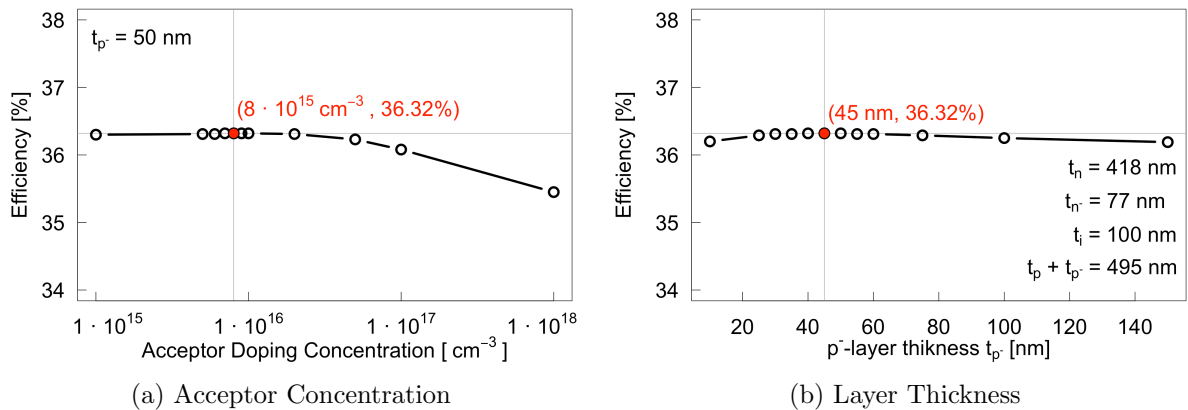(a) Acceptor Concentration

(b) Layer Thickness

Figure 4.55: (a) The effect on the efficiency when the doping concentration is varied in the narrow p^--layer. (b) The effect on the efficiency when the thickness of the n^--layer is varied. The doping concentration of the layer is $8 \cdot 10^{15}$ cm^{-3}.

Performance Parameters

The performance parameters of the $GaAs^*$, IPV - $ppinn$ cell are summarized in Table 4.26. Compared to the $GaAs$, IPV - $pinn$, the efficiency of the $GaAs$, IPV - $ppinn$ is 0.85% higher.

Table 4.26: Performance parameters for the $GaAs^*$, IPV - $ppinn$ cell.

	η [%]	J_{SC} [mA/cm^2]	V_{OC} [V]	FF [%]
$GaAs$, IPV - CB	33.06	38.03	1.07	81.29
$GaAs^*$, IPV - pin	34.71	38.73	1.07	83.75
$GaAs^*$, $No\ IPV$	30.95	32.92	1.07	88.12
$GaAs^*$, IPV - $pinn$	36.08	38.74	1.07	86.93
$GaAs^*$, IPV - $ppinn$	36.32	38.74	1.07	87.53

Energy Band Diagram and Recombination Rates

The energy band diagram and the radiative and SRH recombination rates at $V = V_{OC}$ for the $GaAs^*$, IPV - $ppinn$ cell are given in Figure 4.56a and Figure 4.56b, respectively. To compare the effect of the addition of the n$^-$-layer in the $GaAs^*$, IPV - $pinn$ cell and the p$^-$-layer in the $GaAs^*$, IPV - $ppinn$ cell, all SRH recombination rates at $V = V_{OC}$ between $z = 490$ and $z = 600$ nm for the $GaAs^*$, IPV - pin, $GaAs^*$, IPV - $pinn$, and $GaAs^*$, IPV - $ppinn$ cells are shown in Figure 4.57.

(a) $GaAs^*$, IPV - $ppinn$
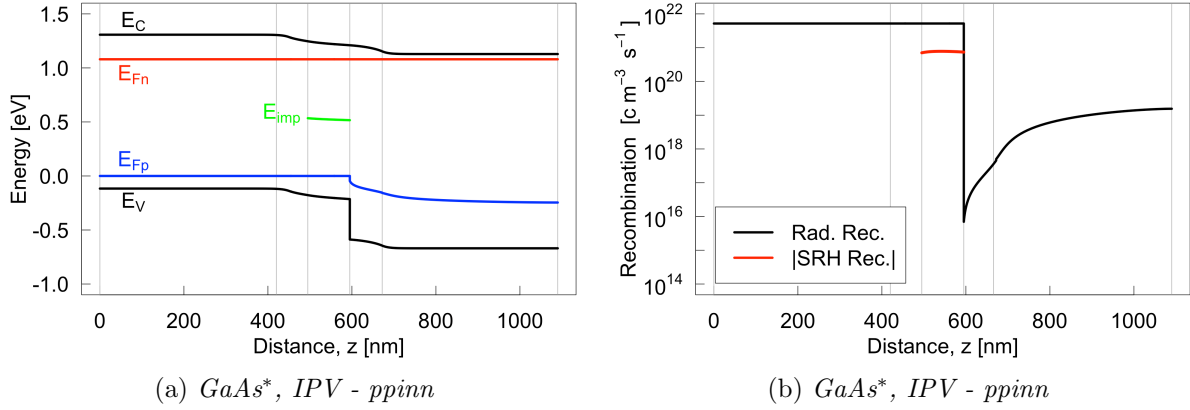(b) $GaAs^*$, IPV - $ppinn$

Figure 4.56: (a) The energy band diagram and (b) the recombination rates at $V = V_{OC}$ for the $GaAs^*$, IPV - $ppinn$ cell. The SRH recombination rate is plotted as its absolute value. The vertical lines indicates the interfaces between the layers.
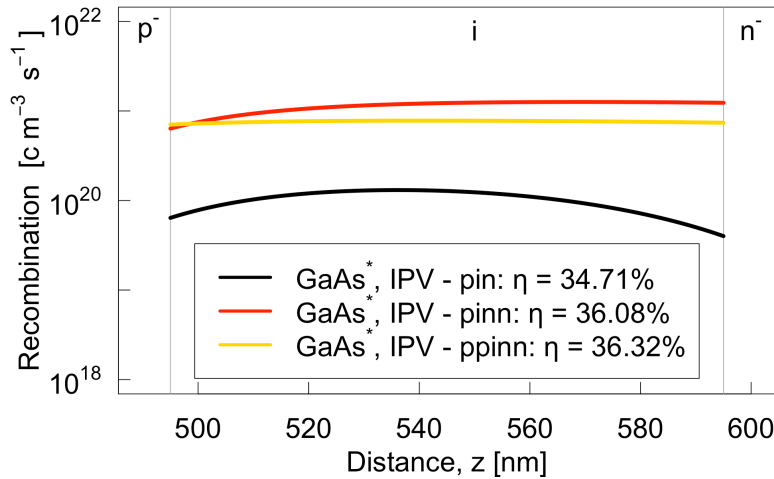

Figure 4.57: SRH recombination rates at $V = V_{OC}$ between $z = 490$ and $z = 600$ nm for the $GaAs^*$, IPV - pin, $GaAs^*$, IPV - $pinn$, and $GaAs^*$, IPV - $ppinn$ cells. They are all plotted as their absolute value. The vertical lines indicates the interfaces between the layers, and the letters are the labelled names of the visible layers.

Discussion

In general, the results here are very similar to the ones for the GaAs homojunction IPV cell in subsection 4.5.2. There, it was already known that the same effect from Santhanam and Fan in Ref. [11] could not be achieved as the cells there were homojunctions. The cells in this section were heterojunction, and the aim was to replicate the effect by Santhanam and Fan. However, the result shows that the same effect occurs when inhomogeneous doping concentration is applied to both IPV homojunctions and heterojunctions. This strongly indicates that the design principle does not have the same effect in IPV cells. It is again suggested that the reason for the improvement is partly due to a increased depletion region width.

The improvement between the homogeneous doped cell ($GaAs^*$, IPV - pin) and the final inhomogeous doped cell ($GaAs^*$, IPV - ppinn) was substantial at 4.63% or 1.61 percentage points. This means that even though the desired effect was not achieved, is the performans increase of such a magnitude that it could be beneficial to apply the changes done here to real IPV cells. As stated previously, the fact that the efficiency increases is more important than why it increases.

A difference between the homojunction cells in the previous section and the heterojunction cells in this section is that an optimal value for the p$^-$-layer was found here, as can be seen by Figure 4.55b. In the previous section in Figure 4.48b, all values over a certain thickness gave the same efficiency. Such a difference was not expected, and the initial thought was then that an error was made during the simulations. However, no such error was found. This suggest that both the introduction of the second i-layer and the fact that this is a heterojunction changes what the optimum value of the p$^-$-thickness is. However, the relationship between these factor is not concluded on in this thesis.

The absolute efficiencies are in general larger for the cells in this section compared to the cells in the previous section. This could suggest that it is better to use heterojunction IPV cells when inhomogeneous doping concentrations is applied. However, as described in subsection 3.3.3, is the value for the absorption coefficient for AlGaAs used in these simulations too large due to an error. This error was not fixed as it was discovered too late. The larger value of absorption coefficient is likely the reason why the heterojunction here performs better.

Table 4.27 summarizes the total SRH recombination rates for the $GaAs^*$, IPV - pin, $GaAs^*$, IPV - pinn, and $GaAs^*$, IPV - ppinn cells. There it can be seen that this value is largest (which means most net generatoin via the impurities) for the $GaAs^*$, IPV - pinn. This can also be seen in Figure 4.57. However, as seen by the performance parameters in Table 4.26, this cell does not have the highest efficiency. This means that other factors than the increase in depletion region width so that the carriers do not recombine as easily is involved when the doping concentrations are changed. It could not be concluded in this thesis what these factors are. However, the improvement of the changes done here is substantial, so more research should be conducted in order to understand and possibly improve the effect observed here.

Table 4.27: Absolute value of total SRH recombination at $V = V_{OC}$ for the $GaAs^*$, IPV - pin, $GaAs^*$, IPV - pinn, and $GaAs^*$, IPV - ppinn cells. A higher value indicates a higher net generation via the impurity.

Cell	$GaAs^*$, IPV - pin	$GaAs^*$, IPV - pinn	$GaAs^*$, IPV - ppinn
Total SRH rec. rate	$1.13 \cdot 10^{22}$ cm^{-3}s^{-1}	$1.24 \cdot 10^{23}$ cm^{-3}s^{-1}	$7.43 \cdot 10^{22}$ cm^{-3}s^{-1}

The results here showed fairly similar behaviour as the homojunction IPV cells. However, one final attempt is done on applying the design principle by Santhanam and Fan on a heterojunction IPV cell. This time, the cells will consist of p-AlGaAs/i-GaAs/n-AlGaAs, i.e. changing the

p-GaAs* with p-AlGaAs. As the band edges forms offsets in such cells, will this first be removed by changing the electron affinty of both p- and n-AlGaAs

4.7 Modified AlGaAs/GaAs/AlGaAs IPV cells

This section repeats the simulation procedure from the previous section, only changing the p-GaAs* to be p-AlGaAs*. In addition, the i-GaAs here uses the real value of the electron affinity, while the electron affinity of p- and n-AlGaAs* have been modified. The asterix in AlGaAs* indicates this modification.

4.7.1 Band Offsets

The aim of this section is to remove the band offsets created in p-AlGaAs/i-GaAs/n-AlGaAs. This is done because section 4.2 showed that a barrier in the CB prevented the positive effect of the design principle by Santhanam and Fan [11].

Results

Energy Band Diagrams

Initially, a p-GaAs/i-GaAs/n-AlGaAs cell labelled the *AlGaAs, No IPV - Barrier* cell was simulated. The energy band diagram at $V = V_{\mathrm{OC}}$ for this cell is shown in Figure 4.58a. The result showed that a CB barrier of $\Delta E_{\mathrm{C}} = 0.33$ eV was formed between the i-GaAs and n-AlGaAs, and that a VB barrier of $\Delta E_{\mathrm{V}} = 0.05$ eV was formed between the p-AlGaAs and i-GaAs. Using Anderson's rule and Eq.(2.6), a modified value of the electron affinity for the n-AlGaAs $\chi_{\mathrm{n\text{-}AlGaAs, new}}$ that removes the CB barrier was calculated to be

$$\chi_{\mathrm{n\text{-}AlGaAs, new}} = \chi_{\mathrm{AlGaAs, old}} + \Delta E_{\mathrm{C}} = 3.740\ \mathrm{eV} + 0.33\ \mathrm{eV} = 4.07\ \mathrm{eV} \tag{4.8}$$

Similarly, for the a modified value of the electron affinity for the p-AlGaAs $\chi_{\mathrm{p\text{-}AlGaAs, new}}$ that removes the VB barrier was calculated to be

$$\chi_{\mathrm{p\text{-}AlGaAs, new}} = \chi_{\mathrm{AlGaAs, old}} - \Delta E_{\mathrm{V}} = 3.740\ \mathrm{eV} - 0.05\ \mathrm{eV} = 3.69\ \mathrm{eV} \tag{4.9}$$

Using these modified values for the electron affinity in the AlGaAs layers, a new cell labelled the *AlGaAs*, *No IPV* cell was simulated. Its energy band diagram at $V = V_{\mathrm{OC}}$ is given in Figure 4.58b, and one can there see that the band offsets were removed.
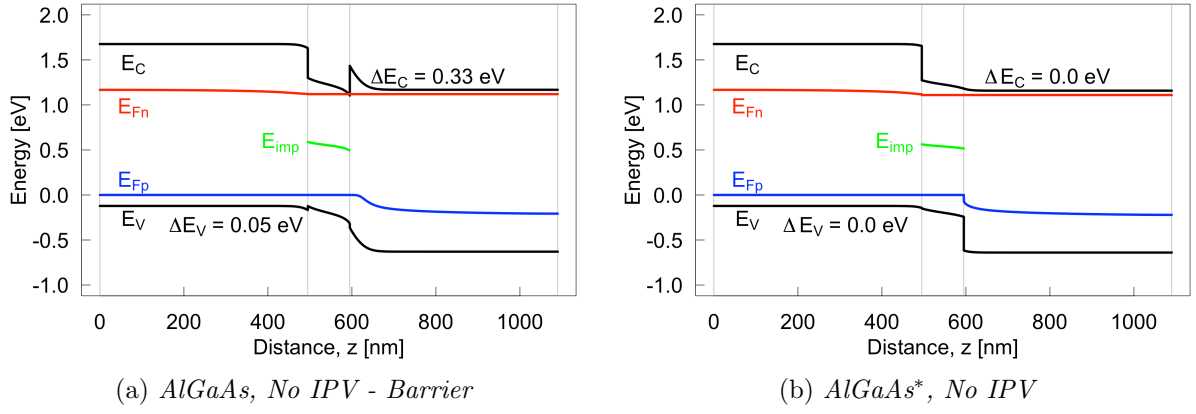
(a) *AlGaAs, No IPV - Barrier*

(b) *AlGaAs*, No IPV*

Figure 4.58: The energy band diagram at $V = V_{\mathrm{OC}}$ for (a) the *AlGaAs, No IPV - Barrier* cell and (b) the *AlGaAs*, No IPV* cell. The vertical lines indicates the interfaces between the layers.

Performance Parameters

The performance parameters of the *AlGaAs, No IPV - Barrier* and *AlGaAs*, No IPV* cells are summarized in Table 4.28. In addition, the performance parameters of a new cell labelled *AlGaAs*, IPV - pin* is included in the same table. This cell is identical to the *AlGaAs*, No IPV*, except optical capture of the carriers via the impurities is activated (i.e. the IPV effect). Comparing the efficiency of the *AlGaAs*, IPV - pin* cell and the *AlGaAs*, No IPV* cell, one can see that these cells benefits from the IPV effect. Additionally, by comparing the *AlGaAs, No IPV - Barrier* cell and the *AlGaAs*, No IPV* cell, one can also see that the removal of the barriers have a negative effect in the cell efficiency.

Table 4.28: Performance parameters for the *AlGaAs, No IPV - Barrier*, *AlGaAs*, No IPV*, and *GaAs*, IPV* cells.

	η [%]	J_{SC} [mA/cm^2]	V_{OC} [V]	FF [%]
AlGaAs, No IPV - Barrier	32.18	32.92	1.11	87.98
AlGaAs*, No IPV	31.95	32.92	1.11	87.53
AlGaAs*, IPV - pin	35.57	38.73	1.11	82.56

Energy Band Diagram and Recombination Rates

The energy band diagram and the radiative and SRH recombination rates at $V = V_{\mathrm{OC}}$ for the *AlGaAs*, IPV - pin* cell are given in Figure 4.59a and Figure 4.59b, respectively.
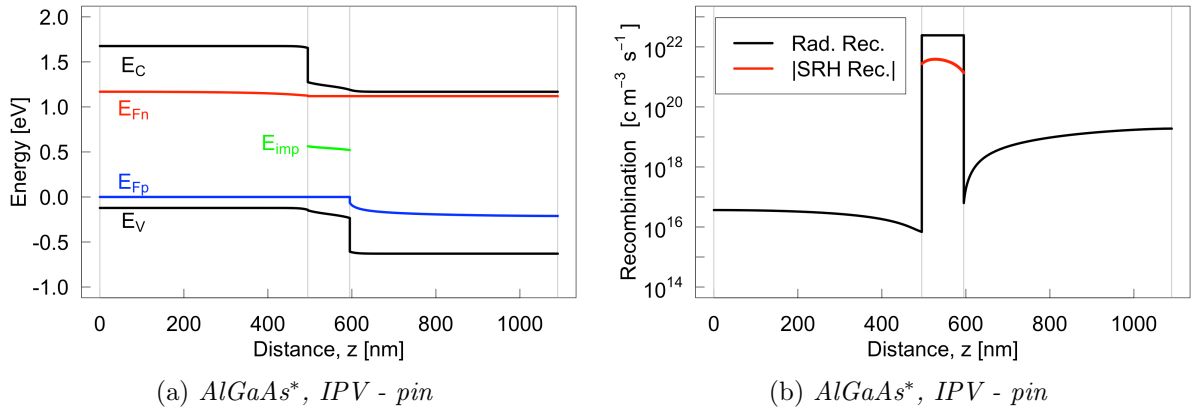
(a) *AlGaAs*, IPV - pin*

(b) *AlGaAs*, IPV - pin*

Figure 4.59: (a) The energy band diagram and (b) the recombination rates at $V = V_{OC}$ for the *AlGaAs*, IPV - pin* cell. The SRH recombination rate is plotted as its absolute value. The vertical lines indicates the interfaces between the layers.

Discussion

Again, the main takeaway from a section where band offsets have been removed it that this were done successfully, while recalling that this is done by changing an intrinsic property of the materials. Comparing Eq.(4.8) and Eq.(4.9), one can see that the sign changes from + to − between them. This is simply a sign convention. Both ΔE_V and ΔE_V are here given as energy distances, i.e. they are are always positive. Since the n-AlGaAs layer needs to be "moved" down in the energy band diagram is it necessary to add the offset value. Similarly, as the p-AlGaAs layer needs to be "moved" up, the value needs to be subtracted here.

4.7.2 p-p-i-n-n IPV Cells

In this section, the simulation procedure from the two preceding sections is repeated. This means that the p*- and n*-layers of the cell is split into two, and the doping concentrations and thicknesses of the layers in contact with the i-layer are optimized.

Results

Efficiency vs. n-layer Thickness and Doping Concentration

Using a thickness of 50 nm in the narrow n⁻-layer, the doping concentration was varied as shown in Figure 4.60a. All doping concentrations from and below $1 \cdot 10^{14}$ cm^{-3} resulted in the highest efficiency at 37.20%. This means that the highest efficiency can be obtained by removing the doping all together in this layer, i.e. creating an i-layer. The thickness of this new i-layer without the IPV effect or impurities was then varied as shown in Figure 4.60b. The highest efficiency was found to be 37.40% at a thickness of 125 nm. The cell with the additional 125 nm i-layer is labelled *AlGaAs*, IPV - pinn*.

Performance Parameters

The performance parameters of the *AlGaAs*, IPV - pinn* cell are summarized in Table 4.29. The previous cells from this section are included for comparison. The result showed that *AlGaAs*, IPV - pinn* cell has a 5.14% higher efficiency than the homogeneously doped *AlGaAs*, IPV - pin* cell.

113

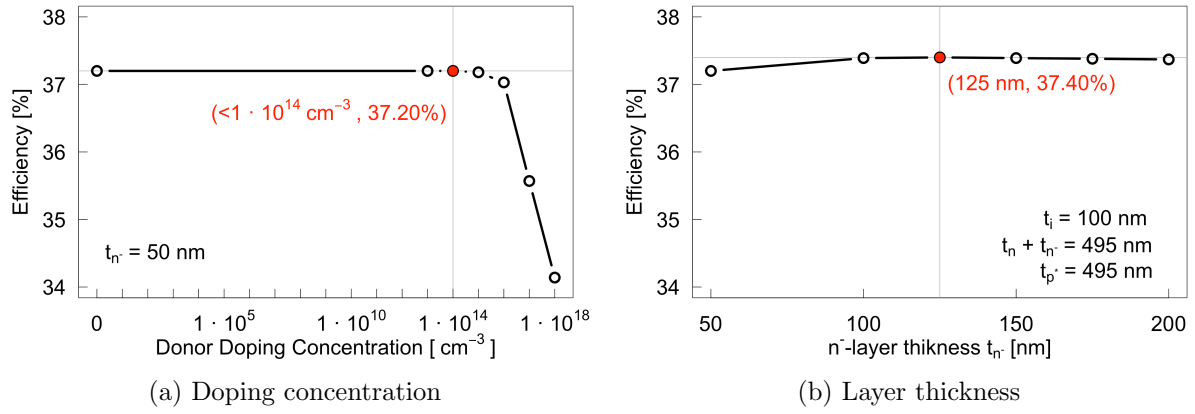(a) Doping concentration

(b) Layer thickness

Figure 4.60: (a) The effect on the efficiency when the doping concentration is varied in the narrow n-layer. (b) The effect on the efficiency when the thickness of the narrow n-layer is varied. The doping concentration of the layer is 0 cm^{-3}, i.e. actually making it an i-layer.

Table 4.29: Performance parameters for the *AlGaAs*, IPV - pinn* cell.

	η [%]	J_{SC} [mA/cm^2]	V_{OC} [V]	FF [%]
AlGaAs, No IPV - Barrier	32.18	32.92	1.11	87.98
AlGaAs*, No IPV	31.95	32.92	1.11	87.53
AlGaAs*, IPV - pin	35.57	38.73	1.11	82.56
AlGaAs*, IPV - pinn	37.40	38.74	1.11	86.70

Energy Band Diagram and Recombination Rates

The energy band diagram and the radiative and SRH recombination rates at $V = V_{OC}$ for the *AlGaAs*, IPV - pinn* cell are given in Figure 4.61a and Figure 4.61b, respectively.
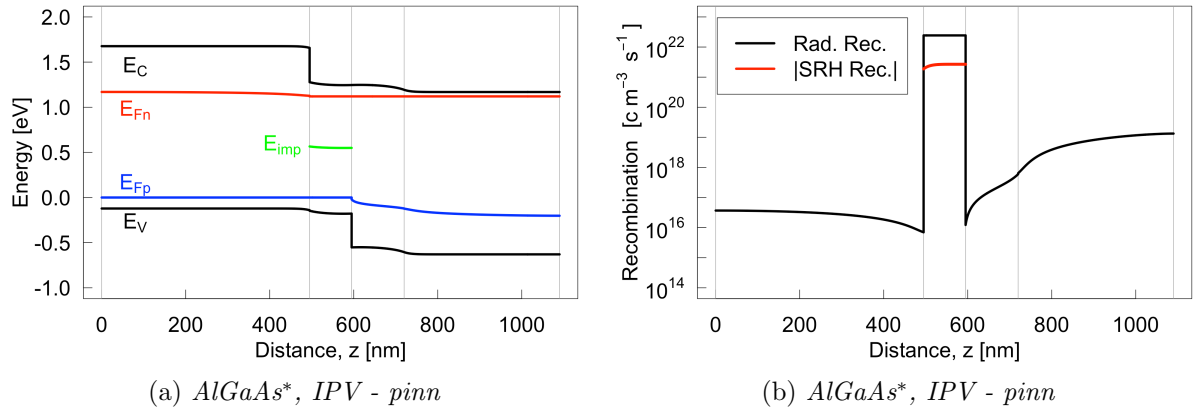

(a) *AlGaAs*, IPV - pinn*

(b) *AlGaAs*, IPV - pinn*

Figure 4.61: (a) The energy band diagram and (b) the recombination rates at $V = V_{OC}$ for the *AlGaAs*, IPV - pinn* cell. The SRH recombination rate is plotted as its absolute value. The vertical lines indicates the interfaces between the layers.

Efficiency vs. p-layer Thickness and Doping Concentration

Figure 4.62a shows the result on the efficiency when the doping concentration in the narrow p$^-$-layer is varied. The highest efficiency was found to be 37.60% at a doping concentration of $1 \cdot 10^{16}$ cm^{-3}. Using this doping concentration, the thickness of the the same layer is varied as shown in Figure 4.62b. At a thickness of 40 nm was the maximum efficiency of 37.61% obtained This cell with this found doping concentration and thickness is labelled *AlGaAs*, IPV - ppinn*.

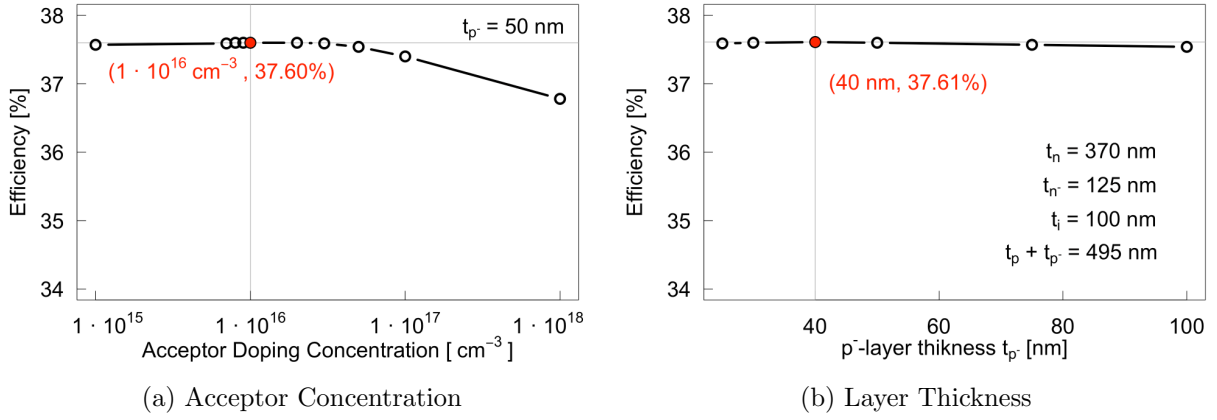(a) Acceptor Concentration

(b) Layer Thickness

Figure 4.62: (a) The effect on the efficiency when the doping concentration is varied in the narrow p$^-$-layer. (b) The effect on the efficiency when the thickness of the narrow p$^-$-layer is varied. The doping concentration of the layer is $1 \cdot 10^{16}$ cm^{-3}.

Performance Parameters

The performance parameters of the *GaAs*, IPV - ppinn* cell are summarized in Table 4.26. Compared to the *GaAs, IPV - pinn*, the efficiency of the *GaAs, IPV - ppinn* is 0.85% higher.

Table 4.30: Performance parameters for the *AlGaAs*, IPV - ppinn* cell.

	η [%]	J_{SC} [mA/cm^2]	V_{OC} [V]	FF [%]
AlGaAs, No IPV - Barrier	32.18	32.92	1.11	87.98
AlGaAs*, No IPV	31.95	32.92	1.11	87.53
AlGaAs*, IPV - pin	35.57	38.73	1.11	82.56
AlGaAs*, IPV - pinn	37.40	38.74	1.11	86.70
AlGaAs*, IPV - ppinn	37.61	38.75	1.11	87.21

Energy Band Diagram and Recombination Rates

The energy band diagram and the radiative and SRH recombination rates at $V = V_{OC}$ for the *AlGaAs*, IPV - ppinn* cell are given in Figure 4.63a and Figure 4.63b, respectively.

(a) *AlGaAs*, IPV - ppinn*

(b) *AlGaAs*, IPV - ppinn*
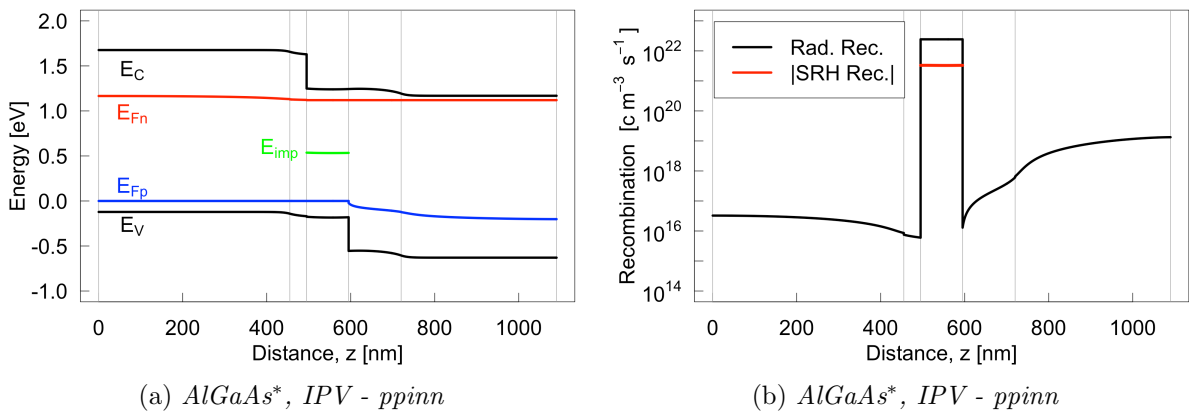
Figure 4.63: (a) The energy band diagram and (b) the recombination rates at $V = V_{OC}$ for the *AlGaAs*, IPV - ppinn* cell. The SRH recombination rate is plotted as its absolute value. The vertical lines indicates the interfaces between the layers.

To compare the effect of the addition of the i-layer in the *AlGaAs*, IPV - pinn* cell and the p-layer in the *AlGaAs*, IPV - ppinn* cell, all SRH recombination rates at $V = V_{OC}$ between z = 490 nm and z = 600 nm for the *AlGaAs*, IPV - pin, AlGaAs*, IPV - pinn*, and *AlGaAs*, IPV - ppinn* cells are shown in Figure 4.64.
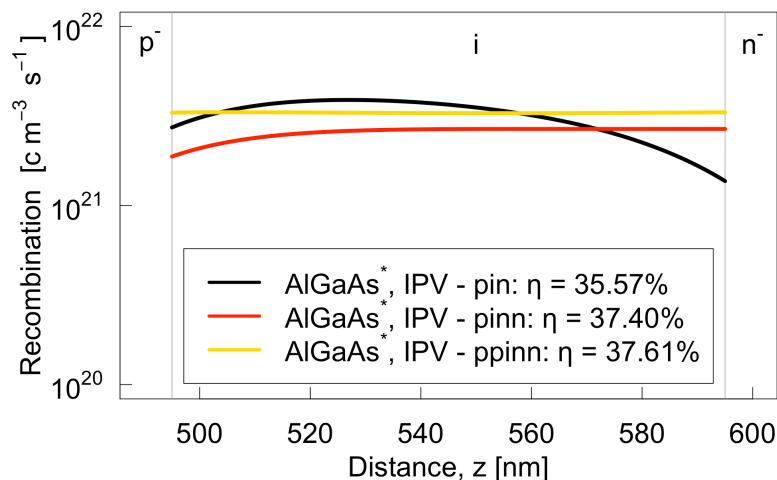

Figure 4.64: SRH recombination rates between z = 490 nm and z = 600 nm at $V = V_{OC}$ for the *AlGaAs*, IPV - pin, AlGaAs*, IPV - pinn*, and *AlGaAs*, IPV - ppinn* cells. They are all plotted as their absolute value. The vertical lines indicates the interfaces between the layers, and the letters are the labelled names of the visible layers.

Discussion

Unfortunately, no new information was obtained from these cells. The discussion of these cells would be almost identical to the ones for the *GaAs*, IPV - ppinn* cell from subsection 4.6.2, and is thus not repeated here. The cells in this section does also her improve substantially when the inhomogeneous doping is utilized (by 5.74%). This is not the same as in the paper by Santhanam and Fan, but partly due to a wider depletion region and partly due to some other factors that are not concluded on here. Regardless, the improvement is of such a magnitude that it could be beneficial to apply to real IPV cells.

Chapter 5

Conclusion and Future Work

5.1 Conclusion

In this thesis, the solar cell simulation program SCAPS has been used to investigate a doping design principle that utilizes inhomogeneous doping around the depletion region to suppress the SRH recombination mechanism in heterojunctions. IPV solar cells have deep-level states in the bandgap that allows for a two-step generation path. However, the same states can act as recombination centers, reducing the cell efficiencies. The aim of the thesis was thus to utilize the doping design principle in IPV solar cells, with the goal of achieving higher efficiency cells by improving the generation-to-recombination rate via the deep-level states in the bandgap.

The doping design introduced by Santhanam and Fan [11] was successfully replicated, and SCAPS was deemed suitable for simulating the design principle of inhomogeneous doping. However, the results showed some inconsistencies when the layers in the cells were divided in two, especially when this was done close to the initial layer interfaces. This problem is caused my the mesh algorithm in SCAPS, as it increases the number of calculation points in proximity to interfaces. While this problem is solvable by adjusting SCAPS's mesh generation settings, this solution was considered both too time consuming and to get consistent results for this thesis. Instead, the conclusion is that the improvements obtained from the design principle is slightly lower than what the numeric values indicates.

The design principle was first applied to p-GaAs/n-AlGaAs cells. Unfortunately, this resulted in a substantial efficiency *decrease*. This was due to the CB offset between the GaAs and AlGaAs. The inhomogeneous doping raised the barrier height, and this reduced the number of electrons contributing to the current. A general conclusion is thus that the design principle only is applicable to interfaces without band offsets, and that GaAs/AlGaAs cells thus are not suitable. In this thesis, in odder to continue the work, this problem was bypassed by modifying the electron affinities of the materials to remove the band offsets. This is not possible to achieve in real GaAs/AlGaAs, and the subsequent result were then based on a hypothetical band offset-free heterojunction.

Using modified CB offset-free p-GaAs/n-AlGaAs, the design principle successfully resulted in higher efficiency cells. It was anticipated, as it is know that the effect of the principle is greater for lower voltage cells, that the improvement in the redesigned cell could be greater during lower incident light power. However, by comparing to a similar homogeneously doped cell, the efficiency improvement with and without the doping design principle was approximately constant. The conclusion is thus that the performance increase of the redesigned cells were approximately the same all incident light powers, and that the initial hypothesis was incorrect.

By increasing the CCS and the impurity density, low efficiency modified CB offset-free p-GaAs/n-AlGaAs cells were simulated. Using a these cells, the thicknesses of the inhomogeneously doped layers were varied. This process was found to be very valuable, as the efficiency at the optimal layer thicknesses was found to be over 20% greater than that of the initial cell. However, the optimal thicknesses of the layers are only relevant for the exact materials simulated here, and there is no way to argue that these values will be optimal for other cells. Instead, the conclusion is that a similar thickness optimization of the layers should be conducted on all cells before applying the design principle so that the maximum improvement is obtained.

Lastly, three IPV cells with inhomogeneous doping concentration around the middle i-layer, one GaAs homojunction, one p-GaAs/i-GaAs/n-AlGaAs heterojunction, and one p-AlGaAs/i-GaAs/n-AlGaAs heterojunction, were investigated. By optimally including the inhomogeneously doped layers the efficiency of the three cell improved by 5.46%, 4.64%, and 5.74%, respectively. This is a substantial improvement, and the conclusion is thus that this method could be applicable for IPV cells.

However, the positive effect in the IPV cells does not have the same origin as what is observed for the conventional cells without the IPV effect. This is supported by the fact that the positive effect of the design changes in the IPV cells did not require that the structures were heterojunctions, which is a requirement in Santhanam and Fan's design. Instead, it is suggested that part of the reason why the IPV cell efficiencies improves is due to a widening of the depletion region. This leads to a more effective transport of the generated carriers which result in lower SRH recombination. However, not all simulated IPV cell in this thesis follows a trend of higher efficiency with higher net generation via the deep-level states. Therefor the widening of the depletion region cannot be the only explanation. This thesis did not manage to give a definite conclusion on why the design changes in the IPV cells resulted in better performing IPV cells, and more research it thus needed.

5.2 Future Work

The majority of the simulations in this thesis have been conducted on cells where the electron affinity of at least one layer have been changed. This cannot be done in real materials, but was done to remove the band offsets. Therefore, if similar cells as have been simulated here is to be made experimentally, other materials must be used. Thus, it is suggested for future work to try to find a suitable pair of materials that form a band offset-free heterojunciton.

In all but one cell in this theses the total thickness of the cells were kept constant wile the relative layer thicknesses were varied. It is possible that an even greater effect of the design principle could be achieved if the absolute thicknesses of the layers also were varied.
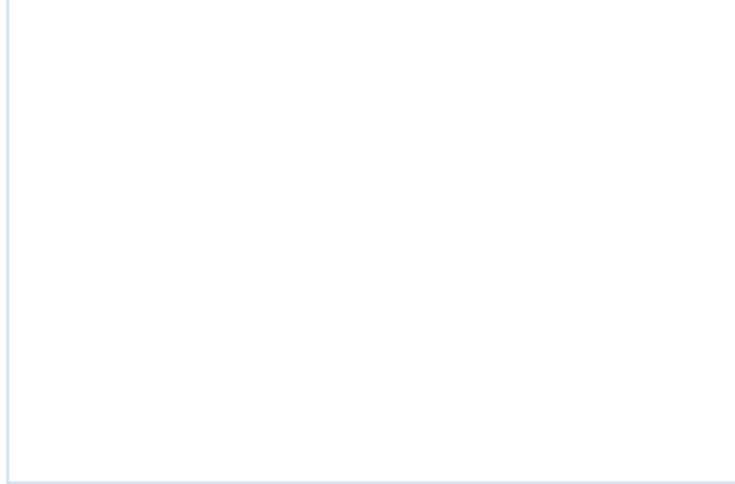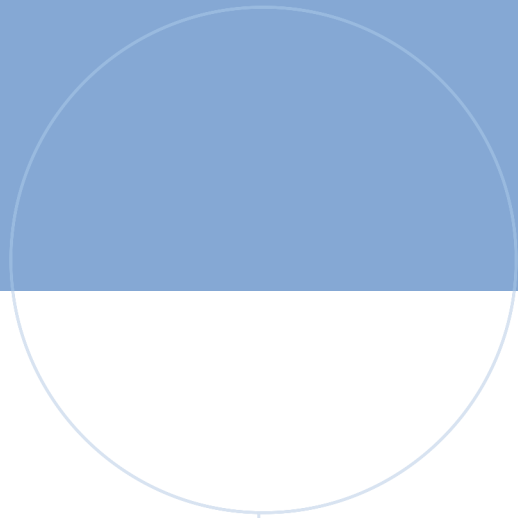
The result in this thesis showed that inhomogeneously doping concentration around the i-layer in IPV cells substantially can improve their efficiency. However, this thesis was not able give a definite conclusion on why this is observed. Therefore, in future work could this effect be investigated more.

References

[1] BP. bp statistical review of world energy. Technical report, BP, 2022 [Online].

[2] United Nations. Transforming our world: The 2030 agenda for sustainable development. Technical report, UN, 2015 [Online].

[3] Würfel U. Würfel P. *Physics of Solar Cells: From basic Principles to Advanced Concepts*. Wiley-VCH, Weinheim Germany, 3 edition, 2016.

[4] REN21. Renewables 2022 global status report. Technical report, REN21, 2022 [Online].

[5] William Shockley and Hans J. Queisser. Detailed balance limit of efficiency of p-n junction solar cells. *Journal of Applied Physics*, 32(3):510–519, 1961.

[6] Martin A. Green, Ewan D. Dunlop, Jochen Hohl-Ebinger, Masahiro Yoshita, Nikos Kopidakis, Karsten Bothe, David Hinken, Michael Rauer, and Xiaojing Hao. Solar cell efficiency tables (version 60). *Progress in Photovoltaics: Research and Applications*, 30(7):687–701, 2022.

[7] Antonio Luque and Antonio Marti. Increasing the efficiency of ideal solar cells by photon induced transitions at intermediate levels. *Physical Review Letters - PHYS REV LETT*, 78:5014–5017, 06 1997.

[8] Stephen P. Bremner, Michael Y. Levy, and Christiana B. Honsberg. Limiting efficiency of an intermediate band solar cell under a terrestrial spectrum. *Applied Physics Letters*, 92(17):171110, 2008.

[9] K. Sablon, Y. Li, N. Vagidov, V. Mitin, J. W. Little, H. Hier, and A. Sergeev. Gaas quantum dot solar cell under concentrated radiation. *Applied Physics Letters*, 107(7):073901, 2015.

[10] M. Wolf. Limitations and possibilities for improvement of photovoltaic solar energy converters: Part i: Considerations for earth's surface operation. *Proceedings of the IRE*, 48(7):1246–1263, 1960.

[11] Parthiban Santhanam and Shanhui Fan. Suppressing non-radiative generation and recombination in LEDs, PVs, and photodiode detectors via inhomogeneous doping around the depletion region co-located with a heterojunction. In Denis V. Seletskiy, Mansoor Sheik-Bahae, and Masaru K. Kuno, editors, *Photonic Heat Engines: Science and Applications III*, volume 11702, page 117020P. International Society for Optics and Photonics, SPIE, 2021.

[12] Marc Burgelman. Koen Decock. Alex Niemegeers. Johan Verschraegen. Stefaan Degrave. *SCAPS manual*. Department of Electronics and Information Systems (ELIS) of the University of Gent, Belgium., 2021.

[13] Heggren T. N. G. Tio2-based solar cells. devices and simulations. Specialization project, Norwegian University of Science and Technology, Department of Physics, 2022.

[14] Nelson J. *The Physics of Solar Cells*. Imperial College Press, London, UK, 2003.

[15] S.M. Sze. *Semiconductor Devices: Physics and Technology*. John Wiley & Sons Singapore Pte. Limited, 2012.

[16] Hansen S. E. Simulation of the impurity photovoltaic effect in tio$_2$ solar cells using scaps. Master's thesis, Norwegian University of Science and Technology, Department of Physics, 2022.

[17] Sun-Tae Hwang, Soohyun Kim, Hyeunseok Cheun, Hyun Lee, Byungho Lee, Taehyun Hwang, Sangheon Lee, Wonki Yoon, Heon-Min Lee, and Byungwoo Park. Bandgap grading and al0.3ga0.7as heterojunction emitter for highly efficient gaas-based solar cells. *Solar Energy Materials and Solar Cells*, 155:264–272, 2016.

[18] Bysting T. S. Simulation of the impurityphotovoltaic effect in gaas solarcells. Master's thesis, Norwegian University of Science and Technology, Department of Physics, 2021.

[19] John H. Davies. *The Physics of Low-dimensional Semiconductors: An Introduction*. Cambridge University Press, 1997.

[20] E. Antolín, A. Martí, and A. Luque. 1.29 - intermediate band solar cells. In Ali Sayigh, editor, *Comprehensive Renewable Energy*, pages 619–639. Elsevier, Oxford, 2012.

[21] S. Kalogirou. *McEvoy's Handbook of Photovoltaics: Fundamentals and Applications*. Elsevier Science, 2017.

[22] Antonio Luque, Antonio Martí, Elisa Antolín, and César Tablero. Intermediate bands versus levels in non-radiative recombination. *Physica B: Condensed Matter*, 382(1):320–327, 2006.

[23] M. J. Keevers and M. A. Green. Efficiency improvements of silicon solar cells by the impurity photovoltaic effect. *Journal of Applied Physics*, 75(8):4022–4031, 1994.

[24] Bysting T. S. Numerical simulations of single junction gaas solar cell performance using scaps. Specialization project, Norwegian University of Science and Technology, Department of Physics, 2020.

[25] P Sawicka-Chudy, Z Starowicz, G Wisz, R Yavorskyi, Z Zapukhlyak, M Bester, Ł Głowa, M Sibiński, and M Cholewa. Simulation of tio2/cuo solar cells with scaps-1d software. *Materials Research Express*, 6(8):085918, jun 2019.

[26] Ioffe institute, 2021. Accessed: 2023-03-17.

[27] D. W. Winston. Simwindows – version 1.5.0., 23 January 1999.

[28] J.J. Liou and Frank Schwierz. Evolution and recent advances in rf/microwave transistors. *IEEE Hong Kong Electron Devices Meeting*, 06 2023.

[29] Devendra Kc, Raju Wagle, and Raid Gaib. Modelling and simulation of algaas/gaas solar cell. *American Journal of Engineering Research (AJER)*, 9:218–223, 04 2020.

[30] Martin A. Green, Ewan D. Dunlop, Jochen Hohl-Ebinger, Masahiro Yoshita, Nikos Kopidakis, and Xiaojing Hao. Solar cell efficiency tables (version 58). *Progress in Photovoltaics: Research and Applications*, 29(7):657–667, 2021.